Investigations on Polystyrene Sulfonates and Polyacrylates in the Presence of Specifically Interacting Cations

Von der Fakultät für Naturwissenschaften

der Universität Paderborn

genehmigte

Dissertation

Zur Erlangung des akademischen Grades

Doktor der Naturwissenschaften

Dr. rer. nat.

von

Markus Hansch, M.Sc.

aus Lemgo

Paderborn 2017

Die vorliegende Dissertation entstand im Zeitraum von Januar 2013 bis März 2017 im Arbeitskreis von Prof. Dr. Klaus Huber im Fachbereich für Physikalische Chemie an der Fakultät für Naturwissenschaften der Universität Paderborn.

1. Gutachter: Prof. Dr. Klaus Huber
2. Gutachter: Prof. Dr. Wolfgang Bremser

Die Arbeit wurde eingereicht am: 24.03.2017
Tag der mündlichen Prüfung: 27.04.2017

Danksagungen

Zunächst möchte ich meinem Doktorvater Herrn Prof. Dr. Klaus Huber für die interessante Themenstellung, die sehr gute Zusammenarbeit und die Betreuung danken. Zudem möchte ich mich dafür bedanken, dass ich während meiner Doktorarbeitszeit die Freiheit hatte einen längeren Aufenthalt am ILL und mehrere Aufenthalte bei der BASF verwirklichen zu dürfen.

Weiterhin danke ich Herrn Prof. Dr. Wolfgang Bremser für die Übernahme des Zweitgutachtens meiner Dissertation.

Der Deutschen Forschungsgemeinschaft danke ich für die finanzielle Förderung meiner Arbeit (HU 807/15-1).

Ein großer Dank geht auch an Dr. Ralf Schweins, Dr. Sylvain Prévost, Dr. Rajeev Dattani, Dr. Vitaliy Pipich und Dr. Sebastian Lages, für die Unterstützung/Durchführung von Experimenten am ILL, ESRF, MLZ und MAX-lab. Der BASF, Hans-Peter Kaub und Sascha Deck danke ich für die Bereitstellung des Microkalorimeters und die Beratung bei den Experimenten.

Allen ehemaligen und aktuellen Mitgliedern der Arbeitsgruppe und der gesamten physikalischen Chemie danke ich für die ausgezeichnete Arbeitsatmosphäre und den tollen kollegialen Zusammenhalt.

Zusätzlich danke ich meinen ehemaligen Bacheloranten und SHKs Yanjing Zhang, Linda Kothe und Benjamin Hämisch für die Unterstützung bei meiner Arbeit, wobei ein besonderer Dank an Benni geht.

An dieser Stelle bedanke ich mich auch bei Dr. Jochen Ortmeyer und Dr. Dagny Konieczna für die Freundschaft und die schöne Zeit, die wir an der Uni zusammen verbracht haben.

Ein großer Dank geht auch an meine gesamte Familie für die Unterstützung während des Schreibprozesses. Ein besonderer Dank geht dabei an meine beiden Töchter, die es immer wieder verstehen mich auf ihre unnachahmliche Art und Weise von der Arbeit und von den kleinen Problemen des Alltags abzulenken.

Ein großer Dank geht auch an Dich Nina. Danke für deine Unterstützung und deine Liebe. Danke für jede Stunde, die du dich alleine um die Kinder gekümmert hast und mir damit den Freiraum geschaffen hast, damit ich meine Arbeit zu Ende stellen konnte. Danke für deine Nachsicht und dass du dich selbst und deine Wünsche hintenan gestellt hast, wenn es mal wieder länger im Labor wurde, wenn mal wieder eine Dienstreise anstand oder wenn ich auch nach der Arbeit noch den ganzen Abend vor dem Laptop verbracht habe. Unter anderem deshalb liebe ich Dich.

Zusammenfassung

In der vorliegenden Arbeit werden die Wechselwirkungen zwischen Polyelektrolyten und spezifisch wechselwirkenden Kationen in verdünnten wässrigen Lösungen untersucht, wobei der Fokus auf den Kombinationen Aluminium-Polystyrolsulfonat (AlPSS) und Barium-Polystyrolsulfonat (BaPSS) liegt.

Für beide Kombinationen wurde zunächst das Phasendiagramm bestimmt. Das Phasendiagramm von Polystyrolsulfonat mit Aluminium konnte in Abhängigkeit der Aluminiumkonzentration in drei Bereiche aufgeteilt werden. In einem Bereich mit niedriger Al^{3+}-Konzentration waren die Lösungen klar. Bei höheren Konzentrationen wurden die Lösungen trüb und das Polymer fiel aus. Die beiden Bereiche wurden durch eine Phasengrenzlinie voneinander getrennt, die einen linearen Anstieg der kritischen Al^{3+}-Konzentration mit ansteigender PSS Konzentration aufweist. Bei einer weiteren Erhöhung der Al^{3+}-Konzentrationen wurde eine Re-entrantphasengrenze überschritten. Eine Re-entrantphasengrenze zeichnet sich dadurch aus, dass durch die vermehrte Anbindung der Kationen an den negativ geladenen Polyelektrolyten eine Ladungsumkehr des Polyelektrolytknäuels verursacht wird, die zu einer Löslichkeit des gesamten Komplexes führt. Die Lösungen wurden wieder klar und es war keine Fällung des Polymers mehr zu beobachten. Das Phasendiagramm von Polystyrolsulfonat mit Barium wies nur zwei Bereiche auf, einen stabilen bei niedrigen Ba^{2+}-Konzentrationen und einen instabilen Bereich bei hohen Ba^{2+}-Konzentrationen. Im Gegensatz zu Polystyrolsulfonaten in Gegenwart von Al^{3+} und anderen bekannten Kombinationen von spezifisch wirkenden Kationen in Gegenwart von Polyacrylaten, wies die Phasengrenze von BaPSS einen horizontalen Verlauf auf.

Von beiden Kombinationen wurden Streuexperimente an selektiven Punkten im stabilen Bereich des jeweiligen Phasendiagrams durchgeführt, wobei mit beiden Kombinationen eine Schrumpfung der Polystyrolsulfonatketten mit ansteigender Al^{3+}- bzw. Ba^{2+}-Konzentration zu beobachten war. Die Kettenstruktur von AlPSS blieb bis kurz vor der Phasengrenze knäuelartig, während Polystyrolsulfonate in Gegenwart von Barium kompakter wurden ohne aber bis zur Kugel zu kollabieren. Eine Vergleichsstudie mit Polyacrylaten in Gegenwart von Ba^{2+} zeigte, dass in diesem Fall eine Kollabierung dieser Polyacrylatketten bis zur kompakten Kugel auftrat.

Temperaturabhängige Streuexperimente an AlPSS und BaPSS ergaben im Fall von AlPSS eine Schrumpfung der Ketten mit einer Temperaturerhöhung, während im Fall von BaPSS eine Temperaturerniedrigung zur Schrumpfung führte. Messungen mit der isothermalen Titrationskalorimetrie an verschiedenen Kationen-Polyelektrolyt-Kombinationen zeigten, dass bis auf Polystyrolsulfonat in Gegenwart von Ba^{2+}, in allen anderen untersuchten Kombinationen die Anbindung der spezifisch wirkenden Kationen an das Polymer entropiegetrieben war. Im Fall von Polystyrolsulfonat in Gegenwart von Ba^{2+} wurde dagegen eine exotherme Anbindung beobachtet.

Abstract

Interactions between polyelectrolytes and specifically interacting cations (SIC) in dilute aqueous solutions were investigated in the present work. The focus lies on the combination of aluminum-polystyrene sulfonate (AlPSS) and on barium-polystyrene sulfonate (BaPSS).

First of all phase diagrams for both combinations were determined. The AlPSS phase diagram could be separated into three regimes depending on the Al^{3+} concentration. In a regime of low Al^{3+} concentrations sample solutions remained clear. By increasing the Al^{3+}-concentration the solutions became turbid and the polymer precipitated. The two regimes are separated from each other by a threshold, which shows a linear correlation between the amount of SIC necessary to precipitate the polyelectrolyte and the molar concentration of the negative residues of the polyelectrolyte. By a further increase of the Al^{3+}-concentration a re-entrant phase boundary was crossed, the sample solutions became clear. The reason for this re-dissolution of the polymer chains is the charge reversal due to the binding of a large enough number of multivalent cations to the residual groups of the polyelectrolyte. The phase diagram of BaPSS exhibits just two regimes, one at low Ba^{2+}-concentrations where the solutions were clear and one at higher Ba^{2+}-concentrations, where a precipitation of the BaPSS was observable. In contrast to polystyrene sulfonates in the presence of Al^{3+} and combinations of polyacrylates in the presence of SICs, the phase boundary of BaPSS exhibits a horizontal trend at low polymer concentrations.

Various scattering experiments were carried out for both combinations at selected points in the respective phase diagram. In both cases a shrinking of the polystyrene sulfonate chains could be observed with an increasing concentration of Al^{3+} or Ba^{2+}. The structure of polystyrene sulfonate in the presence of Al^{3+} stays coil-like even at points close to the phase boundary, while the PSS chains in the presence of Ba^{2+} become more compact without collapsing to a compact sphere. A comparative SAXS study on polyacrylate in the presence of Ba^{2+} revealed that the shrinking of the polyacrylate chains proceeded to compact spheres.

Temperature dependent SLS/DLS measurements on AlPSS and BaPSS showed that in case of AlPSS an increasing sample temperature led to a decreasing size of the polymer chain, while in case of BaPSS the same effect occurred with a decreasing sample temperature. Isothermal titration calorimetry measurements on different SIC-polyeletrolyte combinations underlined that except for BaPSS, the binding of the SICs to the polyelectrolytes is an entropically driven process. In case of polystyrene sulfonates in the presence of Ba^{2+} it could be demonstrated that the binding process is exothermic.

Content

1. Introduction

1.1 State of the Art

1.1.1 Polyelectrolytes in the Presence of Counterions

Polyelectrolytes are water soluble polymers, which carry inonizable groups along their backbones. In aqueous solutions the polyelectrolyte (PE) dissociates into the polyion and the respective counter ions. Polyelectrolytes can be separated into three different groups, the negatively charged polyanions (e.g. polyacrylates (PA) and polystyrenesulfonates (PSS)), the positively charged polycations (e.g. quaternized poly(2-vinyl-pyridine)) and polyampholytes (e.g. DNA and proteins), which carry anionic and cationic charges. Polyelectrolytes are very sensitive towards variations of the pH, temperature and the salt content of the solvent. Polyelectrolytes play an important role in industrial applications and nearly all biological processes.

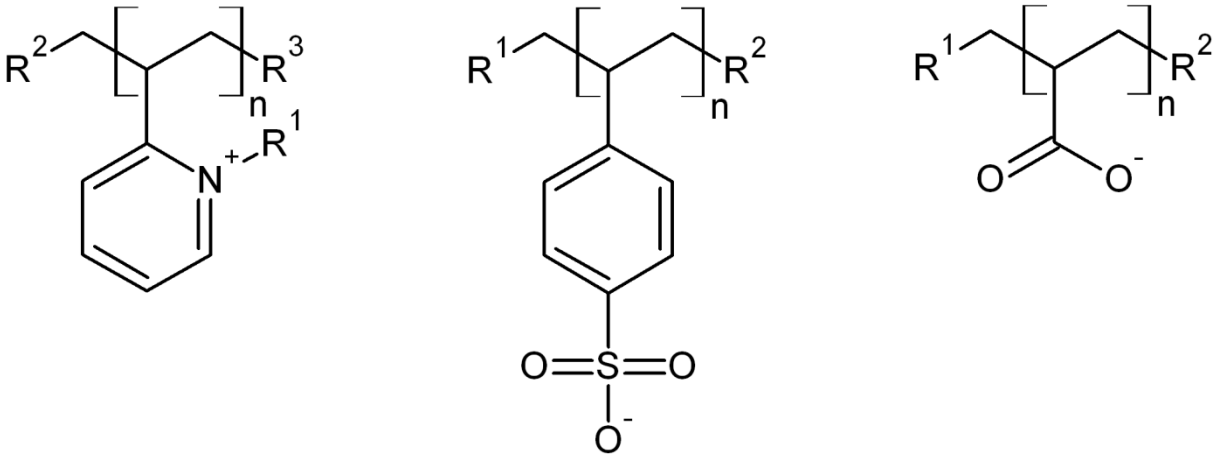

Figure 1: Examples for polyelectrolytes, quaternized poly(2-vinyl-pyridine) (left hand), polystyrene sulfonate (middle) and polyacrylate (right hand).

It is highly relevant to study the response of the polyelectrolyte system towards changes in the solvent conditions. Especially the addition of salts to aqueous polyanion solutions has been studied for decades.[1] To get an idea of the influence of salt on the PE in solutions, we first consider the nature of the charged groups on the polymer itself. Due to electrostatic repulsion these charged residues try to be in solution as far apart from each other as possible. That leads to a coil swelling, whereby the polyelectrolyte coils become bigger than a neutral polymer chain with the same chain length. By the addition of an inert salt the reversed process can be initiated.[2] Takahashi et al. reported an experiment which nicely shows this effect. They performed viscosity measurements on polyacrylate samples with different molecular weights. Each sample was dissolved in pure water with different contents of NaBr. The authors showed that the intrinsic viscosity of each sample was decreasing with increasing NaBr concentration.[3] A decreasing intrinsic viscosity can be explained by a decrease in the hydrodynamic size. Due to the added sodium ions, which are

incorporated in the polyacrylate domain, the intra molecular electrostatic repulsion between the different acrylate groups is shielded. This leads to a shrinking of the coil dimensions, which becomes stronger with increasing inert salt content. The shrinking of the polyacrylate chains with increasing inert salt content was later on proofed by different authors with the help of static and dynamic light scattering (SLS/DLS).[4–6] At a certain inert salt level which depends on the polyelectrolyte and the added salt, theta conditions of the PE chains are reached and the PE chains behave like an ideal polymer chain. For PSS[7,8] the theta conditions are reached at 4.17 M NaCl at 16.4°C or 3.1 M KCl at 25°C and for PA[6,9] theta conditions are reached at 1.5 M NaBr at 15°C or 1.5 M NaCl at 25°C. A further increase of the salt level leads to precipitation of the chains and is denoted in the literature as salting out effect.

In 1951 Wall et al. published experimental results, which gave a hint that a second type of cations exist, which interact more specifically with the residual groups of the polyelectrolytes.[10] The precipitation point of polyacrylic acid in the presence of calcium, strontium and barium hydroxides was investigated. It could be shown that the amount of cations necessary to precipitate the polyacrylic acid chains decreases in the series of the alkaline earth cations from Ca over Sr towards Ba with increasing ionic radius. Since all cations are bivalent, the differences in the critical cation concentration could not be explained by electrostatic effects. Therefore an assumption was made that besides electrostatic interactions another key factor plays a role for the different affinities of the cations toward the acrylate group.[10] In the following that type of cations is called specifically interacting cation (SIC). In contrast to inert salt cations, SICs lead to an increased shrinking of the PE chain, which cannot be explained with a stronger shielding of the intramolecular electrostatics. Other than inert salt cations, SICs interact chemically via complexation with the residual groups of the polyelectrolytes. These cations are in most cases multivalent and can interact therefore at the same time with more than one residual group. The binding of SIC to polyelectrolytes leads to charge compensation and decreased hydrophilic properties of the entire coil, which results in an increased shrinking of the coils and at a certain critical SIC concentration to a precipitation of the chains.[11–16]

In line with those findings Ikegami et al.[17] revealed two different types of thresholds. In one case, denoted as H-type threshold, the phase boundary appears at high salt concentrations and is independent from the polymer concentration. In that case the precipitation is caused by a perturbation of the hydration shell of the polyelectrolyte chains, which is induced by the high concentration of cations in the solution. The H-type threshold corresponds to the salting out effect, which is induced by non-specific interactions between inert salts and polyelectrolytes.

At the L-type threshold the critical SIC concentration is low and depends on the total concentration of the residual groups, which results in a linear increase of a comparable low critical salt concentration with an increasing polyelectrolyte concentration. In systems, which exhibit a L-type threshold, the interaction between cations and residual groups is dominated by specific interactions.[17]

Different authors could show that the L-type threshold can be shifted towards higher critical SIC concentrations with an additionally introduced inert salt. An increasing inert salt content leads to an increased exchange pressure of the inert salt cations on the SIC located at the residual groups of the polyelectrolyte. As a consequence a higher critical SIC concentration is needed to precipitate the SIC-polyelectrolyte system.[12,18] Therefore a re-solution of precipitated SIC-polyelectrolyte complexes can also be achieved by addition of an inert salt.[18] Additionally, Michaeli[18] could reveal from investigating polymethacrylic acid (PMA) at different charge fractions and different NaCl contents in the presence of Ca^{2+}, Mg^{2+} and Ba^{2+}, a quantitative formula, which describes the influence of the inert salt content and the charge fraction α on the slope m and the intercept i of the L-type threshold in the phase diagram,

$$[M^{z+}]_{th} = i + m[COO^-]_{th} \tag{1}$$

with,

$$i = \left(\frac{0.0034}{\alpha^2}\right) + 0.13[NaCl] \tag{2}$$

$$m = \alpha(0.8 - 0.7[NaCl]) \tag{3}$$

where $[M^{z+}]_{th}$ is the critical SIC concentration, $[COO^-]_{th}$ represents the concentration of negatively charged residual groups and [NaCl] denotes the inert salt concentration. He concluded that the total amount of bivalent, specifically interacting cations is composed of two different species.

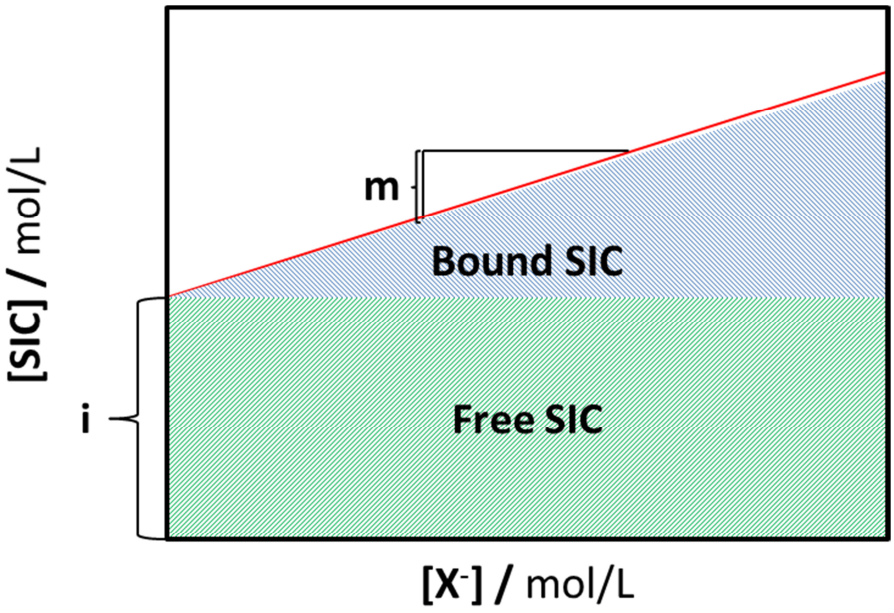

Figure 2: Conclusion of Michaeli[18] for phase diagrams of alkaline earth cation-PMA systems with inert salt content, translated to a more general case thereby [SIC] replaces $[M^{z+}]$ and $[X^-]$ replaces $[COO^-]$. The amount of free SIC is denoted by i and the greenish shaded area. The blueish shaded area represents the amount of SIC which is bound to the polyelectrolyte chain. The stoichiometry between [SIC] and monomeric groups $[X^-]$ can be determined from the slope of the phase boundary (red line). In case of alkaline earth cation-PMA systems, i and m are defined by eq 2 and eq 3.

The part denoted by i is the content of free bivalent cations, while $m[COO^-]_{th}$ describes the minimum amount of bivalent cations which is needed to precipitate the PMA chains. The fraction/slope m is thereby independent from the total PMA monomer concentration and gives valuable information about the stoichiometry of the complex at the threshold (Fig. 2).[18] Interestingly enough Michaeli[18] could not find a trend reported by Wall et al.[10], who could show that the amount of SIC needed for precipitation of PA chains lowers in the row of the alkaline earth cations from calcium towards barium.

Typical SIC-PE systems, which exhibit an L-type threshold are PMAs in the presence of Ca^{2+}, Mg^{2+} and Ba^{2+}, PAs in the presence of alkaline earth cations, Cu^{2+}, Pb^{2+} and Zn^{2+} and PSS in the presence of Al^{3+}, Fe^{3+}, La^{3+} and Th^{4+}.[11–16,18–23]

1.1.2 Polyacrylates in the presence of SICs

The working horse for investigations on SIC-polyelectrolyte systems in our group was the sodium polyacrylate.

In 1993 Huber reported experiments on polyacrylate in the presence of Ca^{2+}-cations, established by static light scattering and viscosimetry.[11] For these experiments two polyacylate samples were dissolved in 0.1 M NaCl at a pH of 9. Under these conditions the PA chain is highly charged and the chains are electrostatically shielded from each other, which is necessary if the single coil behavior shall be investigated by light scattering. For two PA samples four different calcium contents by replacement of sodium ions were established under the condition that each calcium ion replaces two sodium ions at a constant level of cationic charges [I] with excess Na^+ ions ($[I]=\text{constant}=0.1=2[Ca^{2+}]+[Na^+]$). For the different calcium contents the squared radius of gyration and the viscosity was measured as a function of the polyacrylate concentration. It could be shown that the squared radius of gyration R_g^2 and the reduced viscosity decreased with decreasing polyacrylate concentration. Thereby R_g^2 was much smaller than the value which was obtained for the same samples at theta conditions, which underlines the SIC character of the Ca^{2+}-cation. Additionally, by keeping the overall concentration of charges in the experiment constant at [I]=0.1, the coil collapse induced by the Ca^{2+}-cations could not be misinterpreted as an increased shielding provoked by the Ca^{2+}-cations. For each $(R_g^2)^2$ versus $[COO^-]$ curve an extrapolation towards $(R_g^2)^2=0$ was done, thereby obtaining for each sample series a collapse concentration. The collapse concentration increased linearly with increasing PA content, which correlated nicely with an L-type threshold reported by Ikegami et al.[17].

In the following Schweins investigated the influence of Ca^{2+}, Sr^{2+} and Ba^{2+} on polyacrylates in saline, diluted solutions.[24] He followed the procedure which was applied by Huber[11]. The pH of the solutions was adjusted to 8 – 9 and the alkaline earth cations were introduced via replacement of sodium ions ($[I]=2[M^{2+}]+[Na^+]=\text{const.}$). It could be shown that the phase boundaries for CaPA, SrPA and BaPA each follow an L-type trend, whereby the slope of the thresholds lowers in the row of the alkaline earth cations from Ca^{2+} towards Ba^{2+}.[13] As already mentioned the slope of the threshold gives information about the stoichiometry

between SICs and residual groups at the threshold. Therefore it can be assumed that less Ba^{2+} is needed to precipitate the polyacrylate chains than in case of Ca^{2+} and Sr^{2+}, which is in line with the findings of Wall et al.[10]. Combined static- and dynamic light scattering (SLS/DLS) experiments on selected points below the threshold revealed a shrinking of the polyacrylate chains with increasing SIC concentration, whereby for all three systems a collapse from coils towards compact spheres at states located close to the phase boundary could be observed.[12,13] Additional small angle neutron scattering (SANS) experiments revealed for CaPA pearl necklace-like structures at intermediate states in the phase diagram.[25] The scattering curves were fitted satisfactorily with a pearl necklace form factor.[26] Also for SrPA a combined small angle x-ray scattering/anomalous small angle x-ray scattering (SAXS/ASAXS) experiment revealed a pearl necklace-like structure at intermediate states.[27]

Lages worked on PbPA and CuPA.[28] Additionally he investigated the influence of temperature on the solution behavior of polyacrylate chains in the presence of Sr^{2+}- and Ca^{2+}-cations and the aggregation of CaPA and CuPA at states located slightly above the threshold. He also followed the sample preparation procedure which was reported by Huber[11]. For PbPA and CuPA it could be shown that the thresholds exhibit an L-type trend, but are less sensitive to ion exchange at variable [I] compared to alkaline earth cation-PAs, which gives a hint that the interaction between Cu^{2+} and Pb^{2+} and the PA is stronger than in case of alkaline earth cation-PAs. The total shrinking of the PA chains in the presence of Cu^{2+} and Pb^{2+} is not as strong as in case of the alkaline earth cations and the chains remain coil like even at states close to the threshold.[14,15] However, in case of PbPA pearl necklace-like structures could be revealed at intermediate states in the phase diagram by combined SAXS/ASAXS measurements, which could be fitted by a pearl necklace form factor.[15] Time resolved light scattering experiments on the aggregation of CaPA and CuPA revealed compact aggregates in the case of CaPA and more fluffy aggregates with CuPA.[14] That fitted nicely to the results of light scattering experiments on none aggregated samples, where it could be shown that CaPA collapses from coils to compact spheres, whereby CuPA remains coil-like even at states close to the phase boundary.[14]

Temperature dependent combined light scattering experiments on CaPA and SrPA showed a decrease in the size of the polyacrylate coils with increasing sample temperature. In combination with results from ITC experiments on CaPA performed by Antonietti et al.[29], who obtained a positive binding enthalpy, the experimental results lead to the assumption that the binding process between the Ca^{2+}-cations and the Sr^{2+}-cations and the residual groups in the polyelectrolyte is an entropically driven process. Additionally, states at different sample temperatures were investigated for CaPA by means of SANS and AFM.[30,31] Thereby a partial densification of the chains with increasing sample temperature could be shown. The SANS scattering curves at high temperatures could be fitted with a pearl necklace form factor. The experiment showed that independent of the method (increasing the Ca^{2+}-content or increasing the sample temperature), which was used to approach the phase boundary the same transition of the polyacylate chains could be observed.

In the following Ezhova worked on polyacrylates in the presence of silver cations.[32] It could be shown that the phase diagram of AgPA is much more complex, compared to the phase diagrams, which were established before.[16] From bottom to top, the AgPA phase diagram can be subdivided into four regimes: single coils, dense unstable aggregates, stable aggregates and precipitates. The regime, where single coil behavior can be observed is very narrow, the threshold exhibits a very small slope of m=0.001 and a considerable coil shrinking could not be observed by combined light scattering while approaching that phase boundary. Above that phase boundary in a region of $0.001 < Ag^+/COO^- < 0.3$ the polyacrylate chains form coil-like aggregates. These aggregates become denser and unstable aggregates are formed with increasing content of Ag^+ ($0.05 < Ag^+/COO^- < 0.3$). In a region between $0.3 < Ag^+/COO^- < 3$ stable aggregates appear. A further increase of the silver concentration to Ag^+/COO^- ratios larger than 3 leads to precipitation of the AgPA aggregates.

Additionally spherical nano brushes consisting of a polystyrene core and a polyacylate shell were synthesized.[33] The nano brushes were analyzed by combined SLS/DLS in the presence of Ag^+, Mg^{2+} and Ca^{2+} at constant [I]=0.01. Thereby comparable to the experiments with linear chains a shrinking of the PA shell with increasing SIC concentration could be observed. The extent of shrinking of the shell was largest with Ca^{2+} and smallest with Mg^{2+}. The maximum shrinking of the PA shell induced by Ag^+-cations was in the middle but the concentration at which the maximum decrease was reached, was smaller with Ag^+ than with the other two SICs, which is in line with the high sensitivity of polyacrylates chains towards the presence of silver ions.

1.1.3 Polystyrenesulfonates in the presence of SICs

A quick overview shall now be presented on results from different authors for SIC-polystyrene sulfonates a second working horse in the field of polyelectrolyte science. A main focus will lie thereby on PSS in the presence of Al^{3+} and Ba^{2+}.

Keller et al. reported precipitation experiments with PSS in the presence of Na^+, Ba^{2+}, Ca^{2+}, Mg^{2+}, Sr^{2+} and Al^{3+}.[21] The experiments were done with polystyrene sulfonate at a pH of 3 – 3.7. The PSS sample had a M_w of $1.2*10^6$ g/mol. An inert salt was not included and the precipitation point was determined by visual inspections of test tube experiments. It was figured out that precipitation of the PS chains occurred only with the addition of Al^{3+} and Ba^{2+}. From these findings a phase diagram for AlPSS and BaPSS could be constructed. The phase diagram for AlPSS exhibits an L-type threshold, while the phase boundary for BaPSS shows a strong increase of the critical Ba^{2+}-concentration with decreasing polymer concentration. Such a trend is typical for a reaction which underlies the law of mass action. In the following the authors did precipitation experiments with chlorosulfonic acid and para-toluene sulfonate in the presence of the same cations which were investigated for the precipitation of the PSS. Only Ba^{2+} (and Mg^{2+} in case of para-toluene sulfonate) led to precipitation, for all the other cations, including Al^{3+}, no precipitation was observed. Therefore it was assumed that two different mechanisms are responsible for the precipitation. In case of BaPSS the precipitation is caused by an association of Ba^{2+} and SO_3^-,

which pulls the complete polymer out of the solution. For AlPSS Keller et al. argued that due to the bridging character of the trivalent salt a coil contraction takes place which goes a long with an increase of the hydrophobic nature of the chain and which eventually leads to the precipitation of the chains. That led to the assumption that in case of BaPSS precipitation is an ionic property, while in case of AlPSS precipitation is a polymeric chain property.

Comparable to AlPSS, L-type thresholds were also found for PSS in the presence of Fe^{3+}, La^{3+} and Th^{4+}.[19,20,23] Interestingly enough PSS in the presence of La^{3+} and Th^{4+} exhibits a re-entrant phase boundary, which is located at higher SIC concentrations above the precipitation threshold. Beyond a re-entrant phase boundary the PE coils dissolve again, because of a charge inversion of the PE chain, which reaches a maximum when every negatively charged group in the polyelectrolyte is bound by a single multivalent cation. That turns the negatively charged polyelectrolyte into a positively charged polyelectrolyte. The intra and intermolecular repulsive electrostatic forces lead to states comparable to those observed below the precipitation threshold. The re-entrant phase boundaries observed in the case of LaPSS and ThPSS exhibit a horizontal threshold, which is independent from PE concentration. The L-type threshold and the re-entrant phase boundary for LaPSS and ThPSS could also be calculated via theoretical considerations in good agreement with the experimental results.[20,34]

BaPSS was also investigated in more details by other authors applying different methods. Especially the nature of the phase boundary is not yet clear cut. As mentioned before in this chapter, Keller et al. found a phase boundary, determined by visual inspections, which obeys the law of mass action.[21] Before Keller et al., Dubin et al. [35] investigated the precipitation of PSS in the presence of Ba^{2+}. Thereby different polymer samples with different molecular weights from 4.2 kD to 1400 kD were used. The PSS samples were dissolved in 0.1 M NaCl and the phase boundaries were established via turbidity titrations with 1 M $BaCl_2$. For a better visibility of the turbidity the samples were illuminated with an intense collimated beam of light. Dubin et al. also showed that the phase boundary of BaPSS had a negative slope. With increasing M_w of the PSS sample the slope became less negative and the thresholds became more horizontal and were shifted to lower critical Ba^{2+}-concentrations. Interestingly he could also show that precipitation of the BaPSS chains could be achieved via cooling a heated BaPSS solution, which seems to be in contrast to the findings for CaPA and SrPA.

In the last two decades Muthukumar et al. published results on PSS in the presence of Ba^{2+}-cations.[36,37] The phase diagrams for different PSS samples with different degrees of polymerization from 82 to 962 were established via visual observations. An inert salt content was not included. Comparable to the results presented by Dubin, a shift towards lower critical Ba^{2+}-concentrations with an increasing degree of polymerization could be observed. But in contrast to the results presented by Keller et al.[21] and Dubin[35], Muthukumar et al.[36,37] found a horizontal phase boundary at low PSS concentrations, which turns into an L-type threshold at 0.01 to 0.02 M of PSS monomers. SANS measurements in the semi-dilute

regime show a decreasing radius of gyration with an increasing Ba^{2+}-content, whereby values for the R_g were in between the calculated values for the rod-like limit and the unperturbed theta conditions. At a certain concentration a strong increase of the total scattering intensity appeared which is in line with the aggregation of the chains, starting beyond the phase boundary. A coil-globule transition could not be observed. Like Dubin et al.[35], Muthukumar et al.[36,37] could show that aggregation and precipitation can be induced via cooling a heated BaPSS solution. This effect was used in time dependent aggregation experiments which were induced via quenching a BaPSS solution to lower temperatures.[38] The aggregation process was followed via SLS, DLS and small angle light scattering (SALS). Combined SLS/DLS measurements on BaPSS samples without inert salt in the stable regime reveals two modes, single chains (fractal dimension 5/3) and aggregates (fractal dimension > 3.5). When the samples are quenched in the unstable regime, an induction period gets visible, where additional aggregates are formed by consumption of single chains. Successively further aggregation of the preformed aggregates starts.

1.2 Motivation and Goals of the Present Work

As it was outlined in the Introduction, a lot of work was done on polyacylates in the presence of alkaline earth cations and transition metal cations. A major concern of the present thesis is, if the results which were obtained from experiments with polyacrylates in the presence of different SICs can be transferred to polystyrene sulfonates in the presence of SICs. The aim of experiments to be done on polystyrene sulfonates in saline solutions in the presence of SICs is to broaden the knowledge on SIC-polyelectrolyte combinations. The most interesting question is if the results which were obtained from SIC-polyarylates in saline solutions concerning type of the threshold, influence of the inert salt content and temperature, SIC dependent chain shrinking and SIC induced shape transition of the PA-chains can be transferred to SIC-polystyrene sulfonates.

Therefore differences and similarities between SIC-polyacrylates and SIC-polysytrene sulfonates will be unraveled. The focus will thereby lie on AlPSS and BaPSS, due to the known differences in the phase behavior. AlPSS exhibits an L-type threshold which can be also observed with polyacrylates in the presence of SIC. For BaPSS phase boundaries were established which follow either a law of mass action trend or which show a horizontal threshold in the dilute regime of PSS. For the following experiments the PSS samples will be dissolved in NaCl solutions. First of all the phase boundaries of AlPSS and BaPSS will be established. The Al^{3+} and Ba^{2+}-cations will be introduced by replacement of the corresponding amounts of Na^+ at constant [I] according to $[I]=z[M^{z+}]+[Na^+]$. The phase diagrams will be established for different polymers with different M_w and for different inert salt contents. On selected states in those phase diagrams investigations by combined SLS/DLS will be done, to investigate the SIC induced shrinking of the PSS coils. SLS/DLS will be supplemented by small angle scattering experiments on selected points in the phase diagram of AlPSS and BaPSS. Thereby it shall be investigated if the shape of the PSS coils in the presence of Al^{3+} and Ba^{2+} changes via an approach to the respective phase boundary.

Additionally a combined SLS/DLS/small angle scattering study on BaPA will be done as a comparison to AlPSS and BaPSS. To this end the BaPA phase diagram which was established by Schweins et al.[13,24] will be used for those experiments. Comparable to the procedure which was outlined for AlPSS and BaPSS, combined SLS/DLS experiments on points in the phase diagram will be performed. Some of these points will then be selected and additionally analyzed by small angle x-ray scattering (SAXS).

Temperature dependent combined SLS/DLS experiments will be performed on AlPSS and BaPSS. It is our major concern to learn which temperature trend the AlPSS follows and if the BaPSS follows actually a trend opposite to that observed with CaPA and SrPA. Successively isothermal titration calorimetry (ITC) experiments will be performed on CaPA, BaPA, AlPSS, BaPSS and CaPSS. Here it shall be scrutinized if the temperature dependent trends from the light scattering experiments can be confirmed by Isothermal Titration Calorimetry.

Also some selected aggregation experiments with BaPSS will be discussed. Thereby the influence of the induction method (temperature quenching or component mixing) will be analyzed in more detail. It is of interest if morphological features which were obtained from the shrinking experiments in the stable part of the phase diagram can be also found in the type of the aggregates or in the aggregation trend.

2. Methods and Instruments

2.1 Static and Dynamic Light Scattering (SLS/DLS)

The general principles of static and dynamic light scattering experiments will be presented in the following two chapters. However, if the reader is interested in further details about the methods, the text books of the following authors are recommended: Lindner and Zemb[39], Berne and Pecora[40], Chu[41], Schärtl[42], Teraoka[43], Colby and Rubinstein[44], Brown[45], Huglin[46] and Kratochvil[47].

2.1.1 Basics of the Static Light Scattering (SLS)

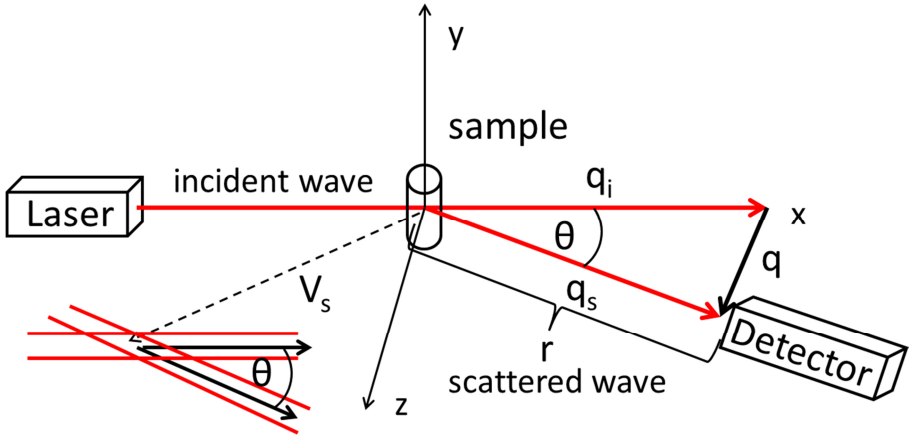

Figure 3: Chart of a basic scattering set-up including some important parameters and variables.

In a light scattering experiment a vertical polarized laser beam illuminates a sample (Fig. 3). The incident wave interacts with the electronic shell of the molecules and induces an oscillating dipole. The oscillating dipole emits part of that light which exhibits the same wave length as the incident beam. A detector which moves at the distance r in the x-y plane around the sample measures the intensity $I_{s(\theta)}$ of the scattered light which hits the detector in dependence of the scattering angle θ. For scattering experiments the scattering angle θ is translated into the scattering vector $\vec{q}$, which has the following value,

$$q_i - q_s = q = \frac{4\pi \times n}{\lambda_0} \sin\left(\frac{\theta}{2}\right) \tag{4}$$

whereby q_i is the value of the incident wave, q_s is the value of the scattered wave, n is the refractive index of the solvent and λ_0 is the vacuum wavelength of the incident beam.

In order to get a scattering intensity, which is independent of the apparatus constants, the intensity of the scattered light $I_{s(\theta)}$ at the scattering angle θ is translated into the Rayleigh ratio ΔR_θ[48] by including the sample-detector distance r, the intensity of the incident wave I_0 and the angular dependent scattering volume $V_{s(\theta)}$.

$$\Delta R_\theta = \frac{d\Sigma}{d\Omega} = \frac{I_{s(\theta)} \times r^2}{I_0 \times V_{s(\theta)}} \tag{5}$$

For particles and molecules which are smaller than $\lambda_0/20$ the scattering is isotropic, which results in a scattering signal that is independent from the scattering angle. This is a typical situation when solvents without any high molecular supplements are measured by light scattering. The interference of scattered light waves from different scattering centers leads for particles which are bigger than $\lambda_0/20$ to a scattering signal, which decreases with an increasing scattering angle. The ratio of the scattered intensity at q divided by the respective intensity extrapolated to q=0 defines the form factor

$$P(q) = \frac{(\frac{d\Sigma}{d\Omega})_q}{(\frac{d\Sigma}{d\Omega})_{q=0}} \tag{6a}$$

The form factor depends on the shape of the scattering particles. Physically the form factor for any molecule consisting out of n identical point-like subunits with the distance r_{jk} is defined by,

$$P(q) = \frac{1}{n^2}\sum_{j=1}^{n}\sum_{k=1}^{n}\frac{\sin(qr_{jk})}{qr_{jk}} \tag{6b}$$

If $qr_{jk}<1$ the form factor can be approximated with a Taylor series. Stopped after the second term this results into,

$$P(q) \approx 1 - \frac{1}{3}q^2\langle s^2\rangle \tag{7}$$

whereby $\langle s^2\rangle$ is the mean squared radius of gyration defined by

$$\langle s^2\rangle = \frac{1}{2n^2}\sum_{j=1}^{n}\sum_{k=1}^{n} r_{jk}^2 = \frac{1}{n}\sum_{j=1}^{n}\langle r_{j,cm}^2\rangle \tag{8}$$

where $\langle r^2_{j,cm}\rangle$ defines the averaged squared distance from the center of mass to the j'th subunit of the molecule.

Expressed in Rayleigh ratios the basic formula for light scattering experiments can be written in the following way,

$$\Delta R_\theta = \frac{d\Sigma}{d\Omega} = K \times c \times M \times P(q) \times S(q) \tag{9}$$

where c is the sample concentration in g/L, M is the molecular weight of the sample in g/mol and S(q) is the structure factor, which can be neglected when the experiments are performed in the dilute regime. K denotes the contrast factor,

$$K = \frac{4\pi^2}{N_A \times \lambda_0^4} \times \left(n_t \times \frac{\partial n}{\partial c}\right)^2 \tag{10}$$

It includes the Avogadro number N_A, the wavelength of the incident beam λ_0, the refractive index of the toluene bath n_t and the refractive index increment dn/dc value of the polymer in the respective solvent.

Practically the angular dependent Rayleigh Ratio of the sample is obtained in the following way,

$$\Delta R_\theta = RR_{toluene} \times \frac{I_{solution(\theta)} - I_{solvent\ (\theta)}}{I_{standard\ (\theta)}} \tag{11}$$

where $RR_{toluene}$ is a tabulated toluene standard, $I_{solution\ (\theta)}$ is the scattering intensity of the sample solution at the scattering angle θ, $I_{solvent\ (\theta)}$ is the scattering intensity of the solvent at the scattering angle θ and $I_{standard\ (\theta)}$ is the scattering intensity of the standard at the scattering angle θ, which is in case of the following work always a toluene measurement.

Including sample-solvent interactions (A_2-parameter) and eq 7 under the assumption that 1/(1-x)≈1+x and rearrangement of eq 9 leads to the Zimm equation[49] for monodisperse systems,

$$\frac{Kc}{\Delta R_\theta} = \frac{Kc}{\frac{d\Sigma}{d\Omega}} = \frac{1}{M} + 2 \times A_2 \times c + \frac{\langle s^2 \rangle}{3\,M} \times q^2 \tag{12}$$

The Zimm equation[49] can be extended to polydispers systems in the following way,

$$\frac{Kc}{\Delta R_{\theta,t}} = \frac{1}{M_w} + 2 \times A_2 \times c_t + \frac{R_g^2}{3\,M_w} \times q^2 \tag{13}$$

where M_w is the weight averaged molecular weight,

$$M_w = \frac{\sum_{i=1}^{n} c_i M_i}{\sum_{i=1}^{n} c_i} \tag{14}$$

R_g^2 is the z-average squared radius of gyration,

$$R_g^2 = \frac{\sum_{i=1}^{n} c_i M_i \langle s^2 \rangle_i}{\sum_{i=1}^{n} c_i M_i} \tag{15}$$

and c_t is the total concentration of the polydispers sample,

$$c_t = \sum_{i=1}^{n} c_i \tag{16}$$

Providing that the dn/dc for the sample in the respective solvent is known and that a dilution series was established, the true non-apparent values for M_w and R_g and the A_2-parameter can be determined by means of the Zimm equation[49]. Details are outlined in the chapter 3.4.1 where characterizations of the different polyelectrolyte samples are presented.

Because of the reason that the size of the polyelectrolyte coils depends in a complex and very sensitive way on the ratio between monomeric groups and SICs, a dilution series cannot be established in those cases. Therefore in the following the values for M_w and R_g obtained

from light scattering experiments of polyelectrolytes in the presence of SICs are apparent values.

An alternative way to evaluate light scattering data is the Guinier approximation[50],

$$\Delta R_\theta = \frac{d\Sigma}{d\Omega} = K \times c \times M_W \times e^{-\frac{R_g^2}{3} \times q^2} \tag{17}$$

A linearization of the scattering curve is achieved by using the natural logarithm whereby validity of the Guinier approximation is ensured by $q * Rg \leq 1$.

2.1.2 Basics of the Dynamic Light Scattering (DLS)

In chapter 2.1.1 it was outlined that the wave length/frequent of the incident beam and the scattered light is the same. But with a closer look on the frequent spectra it can be observed that the line in the spectra of the scattered light is not sharp but slightly broaden. The reasons for this observation are the polymer particles which act as sources of radiation in the light scattering experiment and which underlay in solution a Brownian movement[51–53]. The polymer particles move thereby relative to the primary light source and the detector, the result is basically comparable to the Doppler effect[54] on sound waves.

The degree of line broadening depends on the rate and thereby on the size of the particles. The line broadening itself can be detected by a fluctuation in the scattering intensity. For the SLS experiment only the average value of the fluctuating intensity is used for the analysis. In a DLS experiment the q dependent fluctuation itself is analyzed.

For the further analysis the fluctuating signal is described by the correlation function $g_2(\tau)$. Therefore the scattering intensities at different time slots are correlated with each other. Technically the total measurement time T is subdivided in equal time intervals Δt,

$$T = N \times \Delta t \tag{18}$$

in which it is important that Δt is smaller than a dynamic process of the particle motion. In the following the intensities of different time intervals which are separated from each other by the lag time,

$$\tau = n \times \Delta t \tag{19}$$

are correlated with each other, thereby n is a natural number. If for example n is equal to 5, two intervals are correlated with each other which are separated by 5 time intervals from each other. The correlation is done for all time intervals with $\tau = 5 * \Delta t$ along the time axis T. It follows the summation of the different products and the division by the number of summands N. Afterwards the process is repeated with many different τ's. By a division of the average squared scattering intensity one obtained the intensity-time-correlation function,

$$g_2(\tau) = \frac{\langle I(t) \times I(t+\tau) \rangle}{\langle I(t) \rangle^2} \tag{20}$$

The decrease of the intensity-time-correlation function on a constant value includes all information about the dynamic of the investigated particles. For a further analysis of the data the measurable intensity-time-correlation function has to be translated with the help of the Siegert-relation[55] into the non-measurable field-time-correlation function $g_1(\tau)$,

$$g_2(\tau) = 1 + [g_1(\tau)]^2 \tag{21}$$

For monodisperse systems the field-time-correlation function is defined as follows,

$$g_1(\tau) = e^{-\Gamma \times \tau} \tag{22}$$

where Γ is a decay rate or mean inverse relaxation time, which particles need to cover a mean squared displacement of $1/q^2$. By means of this value the diffusion coefficient of the particles can be determined,

$$\Gamma = D \times q^2 \tag{23}$$

In case of polydispers samples the field-time-correlation function consist out of the sum of the single diffusive modes, weighted by μ_i,

$$g_1(\tau) = \sum_{i=1}^{n} \mu_i e^{-\Gamma_i \times \tau} \tag{24}$$

In the following work the data of the DLS experiments were evaluated by the cumulant analysis established by Koppel.[56] Because of the polydispersity of the sample the exponential function of $g_1(\tau)$ deviates from the exponential function in the monodisperse case. Therefore the decay function is fitted by a series expansion of τ,

$$\ln(g_1(q,\tau) = const. - K_1 \times \tau + \frac{K_2}{2!} \times \tau^2 - \frac{K_3}{3!} \times \tau^3 \ldots \tag{25}$$

For data analysis only the quadratic function was used. The cubic term and terms with higher orders were neglected. With the help of the first cumulant, the z-averaged diffusion coefficient can be calculated.

$$K_1 = \Gamma = \langle D_Z \times q^2 \rangle \tag{26}$$

Practically the data of the dynamic light scattering (DLS) measurements are recorded in the same q-regime as the SLS data. An apparent diffusion coefficient D is obtained at each q-value (angle) from second order cumulant analysis of the respective correlation functions. In case of the sample characterization a true z-averaged diffusion coefficient D_z is determined via extrapolation of the resulting D towards $q^2=0$ and c=0, according to

$$D = D_Z \, (1 + C {R_g}^2 q^2 + k_D c) \tag{27}$$

where C and k_D are constants accounting for the angular dependence and concentration dependence of D respectively. As mentioned in the chapter before in case of the experiments with polyelectrolytes in the presence of SICs a dilution series could not be established because of experimental reasons Therefore the D_Z is in those cases affected by

the concentration dependent part in eq 27. The diffusion coefficient D_Z is used to calculate the effective hydrodynamic radius R_h via the Stokes-Einstein equation[52],

$$R_h = \frac{k_B T}{6\pi\eta D_z} \tag{28}$$

where k_B is the Boltzmann constant, T is the absolute temperature and η is the viscosity of the solvent.

2.1.3 Combined SLS/DLS

Due to the limited q-regime, SLS measurements do not give access to the form factor of the scattering particles, if the size of the particles becomes smaller than 100 nm. In those cases only the Guinier plateau in the beginning can be obtained from SLS experiments, which gives information about the size and the molecular weight of the scattering objects, but conclusion about the shape of the investigated particles are not possible anymore. With the help of combined SLS/DLS experiments, rough estimations about the shape of the particles can be received. Therefore the ratio of the radius of gyration and the hydrodynamic radius is calculated, which is denoted as the structure sensitive parameter ρ,

$$\rho = \frac{R_g}{R_h} \tag{29}$$

With this information a first hint is available if the structure of the scattering objects is sphere-like ρ≈0.78[57], coil-like ρ≈1.3-1.8[58] or rod-like ρ≈2[59,60].

For a more detailed analysis, either SANS or SAXS experiments has to be performed, which give access to a larger q-regime than SLS. Depending on the experimental parameters and combined with SLS a completer form factor of the scattering objects is with these methods available.

2.1.4 List of Light Scattering Instruments

The following four light scattering instruments were used for this work. Three of them are located in the laboratories in Paderborn and one of them is operated by the Large Scale Structures Group at the ILL in Grenoble. In the subsequent table, one picture and the basic data of each instrument are listed.

Table 1: List of the utilized light scattering instruments

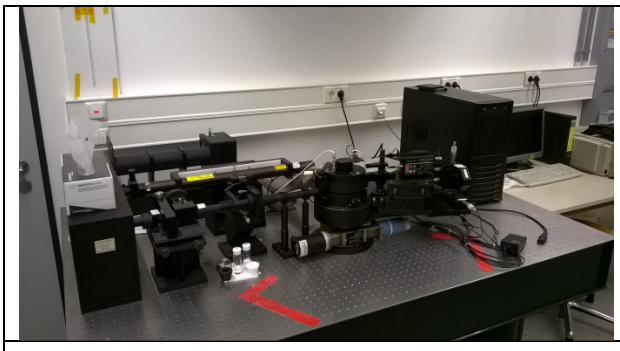	**ALV 5000E CGS** Light source: HeNe laser λ_0: 633 nm Angular range: 12° < θ < 155° Temperature range: 10°C < T < 40°C Detector: 1 movable detector Mode: SLS and DLS Location: AK Huber, Uni Paderborn
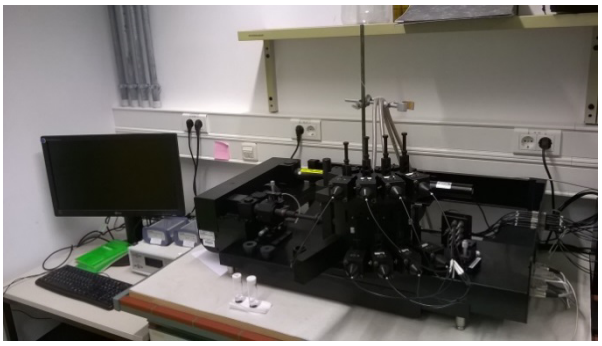	**ALV CGS-3/MD8** Light source: HeNe laser λ_0: 633 nm Angular range: 20° < θ < 136° Temperature range: 10°C < T < 40°C Detector: 8 movable detectors separated from each other by an angle of 8° Mode: SLS and DLS – static and time resolved Location: AK Huber, Uni Paderborn
 [61]	**ALV CGS-3**[61] Light source: HeNe laser λ_0: 633 nm Angular range: 17° < θ < 152° Temperature range: 5°C < T < 50°C Detector: 1 movable detector Mode: SLS and DLS Location: Large Scale Structures Group, ILL
	**Fica 50 modificated by SLS Systemtechnik** Light source: HeNe laser λ_0: 633 nm Angular range: 20° < θ < 145° Temperature range: 10°C < T < 40°C Detector: 1 movable detector Mode: SLS Location: AK Huber, Uni Paderborn

2.2 Small Angle Scattering

As it was mentioned in chapter 2.1.3, small angle scattering experiments are the choice, if a form factor is not available by static light scattering experiments. Due to the wave length of the neutrons or x-rays, which is in these experiments much smaller than the wave length of the lasers used for light scattering experiments, and large/changeable sample-detector distance, a larger q-regime can be investigated by small angle scattering experiments. By adjusting the instrumental parameters, sample detector distance and wave length of the incoming beam, an overlap with the SLS curve can be achieved.. With the help of the form factors, information about the shape of the particles can be gained.

2.2.1 Small Angle Neutron Scattering (SANS)

In small angle neutron scattering experiments neutrons interact with particles. In contrast to light scattering experiments, where the induced light waves interact with the electronic shell of particles, neutrons interact directly with the core of the atoms.[39] Because of that reason the interaction between different isotopes of a single element is different and can be used for the design of the experiment. The differences in interaction can be seen in the value for the scattering length which is the analog to the dn/dc value used in light scattering and describes the interaction between neutrons and elements. One of the most important differences in the scattering length exists in between hydrogen ($-0.374*10^{-12}$cm) and deuterium ($0.667*10^{-12}$cm).[62] The difference in scattering length is used to create a contrast in between the solvent and the dissolved particles/polymers to obtain the net-scattering intensity of the particles. In case of the following work two situations were investigated, deuterated PSS dissolved in H_2O and hydrogenated PSS dissolved in D_2O.

The experiments were carried out at the MLZ in Munich and the ILL in Grenoble. Both neutron facilities use a nuclear reactor running with enriched uranium for the production of neutrons. The neutrons are produced in a chain reaction and moderated at special places in the reactor. Subsequently the moderated neutrons are extracted by evacuated neutron guides from the reactor pool and send to the different instruments. Neutrons which arrive then at the instrument exhibit differences in speed and thereby also in energy and wave length. For the scattering experiment it is necessary that all neutrons, which take part in the scattering process, have nearly the same wave length. Because of that reason a rotating turbine-like speed selector is placed in the neutron guide, which lets just neutrons pass, which have a specific speed/wave length. By adjusting the speed of rotation the wave length of the extinguishing neutron beam can be tuned. Afterwards the neutrons are guided by collimators to the sample, scatter at the sample and impact on the detector.

The two SANS instruments which were used for this work are different in construction and also the data treatment differs slightly. Hence each instrument is introduced in the following by an own chapter.

2.2.1.1 D11

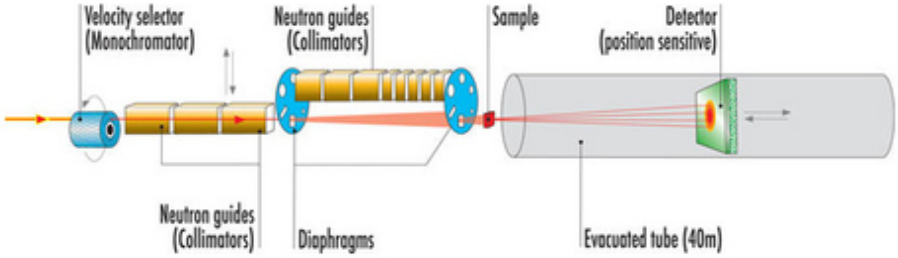

Figure 4: Installation of the D11 located at the ILL in Grenoble.[63]

The D11 instrument located at the ILL in Grenoble is a classical pinhole instrument.[63] The neutrons are guided by evacuated collimators to the sample position, which is located in between the collimators and the detector tank at normal atmospheric pressure and enter after the scattering process through a window into the evacuated detector tank, which has a length of 40 m. The neutrons hit afterwards on a 96*96 cm^2 CERCA ^3He gas detector which is mounted on a movable trolley. The sample detector distance can be varied in between 1.2 and 39 m and the incident neutron beam can be tuned by the selector in between 4.5 Å and 40 Å.

The differential scattering cross section per unit volume in units of cm^{-1} of the solvent and solutions measured with the D11 are calculated according to the following equation,[39]

$$\left(\frac{d\Sigma}{d\Omega}\right)_S = \frac{[I_S(q) - I_{CD}(q)] - A_2[I_{EC}(q) - I_{CD}(q)]}{[I_{H_2O}(q) - I_{CD}(q)] - A_1[I_{EC}(q) - I_{CD}(q)]} \times \frac{A_3}{A_4} \tag{30}$$

Variations in the detector sensitivity are quantified with the H_2O-measurement and considered appropriately in the data evaluation. The factors A_1-A_4 are defined as follows,

$$A_1 = (T_{H_2O}/T_{EC})(1 - n_{H_2O}\tau)/(1 - n_{EC}\tau) \tag{31}$$

$$A_2 = (T_S/T_{EC})(1 - n_S\tau)/(1 - n_{EC}\tau) \tag{32}$$

$$A_3 = T_{H_2O} d_{H_2O}(1 - n_{H_2O}\tau)\left(\frac{d\Sigma}{d\Omega}\right)_{H_2O,eff} \tag{33}$$

$$A_4 = T_S d_S(1 - n_S\tau) \tag{34}$$

The term $(1-n_x\tau)$ corrects for dead time losses, with the integral count rate n_x and the dead time τ. The scattering data are put on an absolute scale by multiplying the scattering data with the tabulated, wavelength dependent, effective differential scattering cross section per unit volume for water $(d\Sigma/d\Omega)_{H2O,eff}$=0.983 cm^{-1} at λ=6 Å. T_S is the transmission of S where S is solution (sl) or solvent (sv) or water (H_2O). The transmission is defined as,

$$T_S = \frac{I_{S(q)}(q = 0)}{I_{EC(q)}(q = 0)} \tag{35}$$

The transmission of the empty cell T_{EC} is defined as the intensity of the beam attenuated by the empty cell divided by the intensity of the empty beam. The scattering cross section of the polymer (pol) is obtained by subtracting the scattering cross section of the solvent (sv) and the incoherent background (inc) of the solution from the solution measurement (sl).

$$\left(\frac{d\Sigma}{d\Omega}\right)_{Pol} = \left(\frac{d\Sigma}{d\Omega}\right)_{sl} - \left(\frac{d\Sigma}{d\Omega}\right)_{sv} - \left(\frac{d\Sigma}{d\Omega}\right)_{inc} \tag{36}$$

2.2.1.2 KWS-3

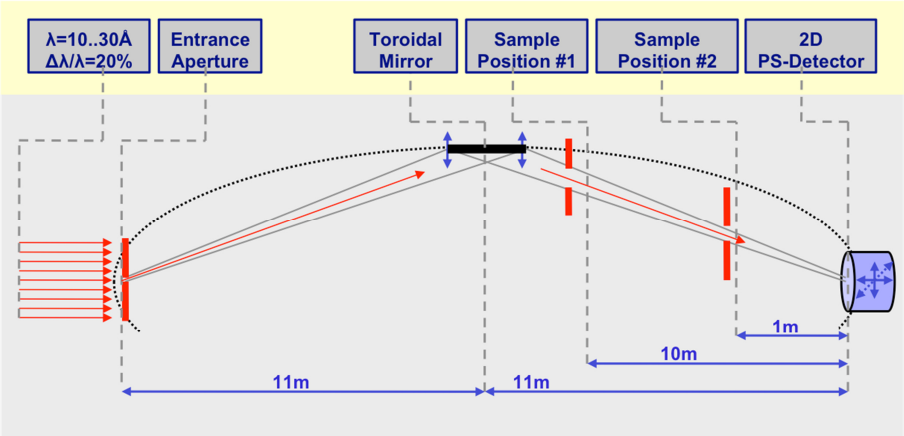

Figure 5: Installation of the KWS-3 located at the FRMII in Garching.[64]

The KWS-3 located at the MLZ in Garching by Munich and operated by the JCNS is also a SANS beam line, but the layout and the principle of operation doesn't follow the principle of pinhole camera but the focusing mirror principle.[64] The centerpiece of the instrument is a double-focusing toroidal mirror, which exhibits two focal points, one located at the entrance of the instrument and one located right on the detector. The neutrons which leave the velocity selector impact on an entrance aperture, which is equal to the first focal point. Subsequently the neutrons hit on the toroidal mirror, where they are reflected in the direction of the detector. On the way to the detector the neutrons transit two sample chambers which can be evacuated. In contrast to a classical pin hole instrument like the D11 the sample-detector positions are fixed due to the sample chambers at 10 m and 1 m. The standard neutron wavelength used for the instrument is 12.8 Å with this configuration a q-range from $1*10^{-4}$ $Å^{-1}$ to $3*10^{-2}$ $Å^{-1}$ is accessible which allows to measure very big particles, e.g. a full form factor of a particle can be recorded which has a radius of 380 nm.

The absolute differential scattering cross section per unit volume in units of cm^{-1} measured at KWS-3 was calculated according to,[65]

$$\left(\frac{d\Sigma}{d\Omega}\right)_S = \frac{L^2}{p^2 T_S h_S I_0}\left([I_S(q) - I_{CD}(q)] - T_S[I_{EC}(q) - I_{CD}(q)]\right) \tag{37}$$

In eq 37, $I_x(q)$ is the recorded scattering signal. The indices S, CD, and EC stand for sample, cadmium and empty cell where sample is either d-NaPSS solution or solvent. Measurement of cadmium provides the electronic background. By measuring an empty cell, the sample background is established. The calibration refers to the intensity of the direct neutron beam I_0.[66,67] The flux I_0 is measured by a direct beam attenuated by an empty cuvette, including a correction for the electronic background. The instrumental parameters p, h_s and L denote the detector pixel size, sample thickness and sample-detector distance. The transmission T_S of S is defined as,

$$T_S = \frac{I_{S(q)}(q=0)}{I_{EC(q)}(q=0)} \tag{38}$$

The scattering cross section of the polymer (pol) is obtained by subtracting the scattering cross section of the solvent (sv) and the incoherent background (inc) of the solution from the solution measurement (sl).

$$\left(\frac{d\Sigma}{d\Omega}\right)_{Pol} = \left(\frac{d\Sigma}{d\Omega}\right)_{sl} - \left(\frac{d\Sigma}{d\Omega}\right)_{sv} - \left(\frac{d\Sigma}{d\Omega}\right)_{inc} \tag{39}$$

2.2.2 Small Angle X-Ray Scattering (SAXS)

X-rays interact in contrast to neutrons with the electron shell of the sample atoms.[39,68] The degree of interaction is thereby proportional to the electron density of the atom, which increases with increasing atomic number and is expressed in the respective scattering length. In a SAXS experiment the contrast between sample and solvent is given by the natural difference in electron density. Therefore an artificial contrast variation, which has to be done for SANS can be omitted for SAXS experiments.

Because of the reason that the interaction between x-rays and sample atoms increase with increasing atomic number and that most of the SIC exhibit higher atomic numbers, SAXS and ASAXS experiments can give access to the distribution of the SIC cations around the polyelectrolyte chain. The method can be a powerful tool, if the structure of condensed domains of SIC-polyelectrolyte complexes, which are enriched by SICs, shall be investigated.

X-rays can be created either by a X-ray tube, which allows the construction of comparable small laboratory based SAXS instruments or by a synchrotron. In a synchrotron electron batches rotate with more than 99% of the speed of light on orbits in an evacuated pipe, whereby magnets force them to stay on the circular path. Hence, the electrons emit tangential to the ring a broad spectrum of hard X-rays, which can be used for various experiments. The broad spectrum of the X-ray beam is an advantage compared to the laboratory based instruments, which work with just one wave length. By means of a monochromator a certain wavelength can be extracted and used in a SAXS instrument which is also located tangential to the synchrotron ring. The adjustment of the wave length enables to tune the q-regime, which shall be covered for the experiment and it allows running ASAXS experiments. Synchrotron radiation facilities are for example the ESRF in Grenoble (France),

Petra III run by the DESY in Hamburg or BESSY II run by the HZB in Berlin or the new MAX IV in Lund. For this work experiments were performed at the ID02 located at the ESRF and I911 SAXS beamline located at the old MAX-Lab in Lund, which was meanwhile shut down.

2.2.2.1 ID02

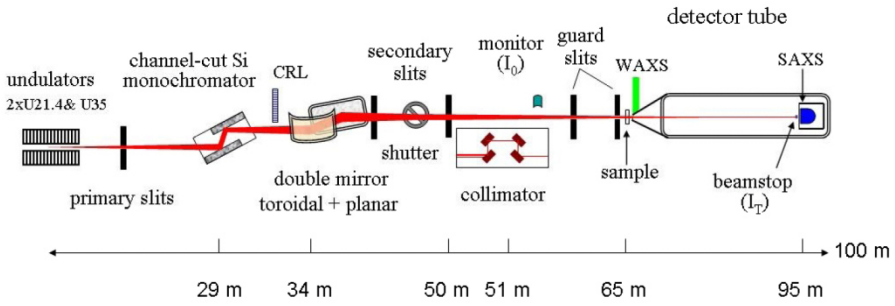

Figure 6: Installation of the ID02 located at the ESRF in Grenoble.[69]

The ID02 is a classical pinhole SAXS instrument.[69] From the undulated X-ray beam which comes from the synchrotron a wave-length is selected with the help of the monochromator and focused by mirrors on the detector. The unique feature is a detector tank with a length of more than 30m, located after the sample position, which contains different movable detectors optimized for different applications. The sample detector distance can be varied from 0.8 m towards 31 m. Connected with the WAXS detector a q-range from 0.001 nm^{-1} to 50 nm^{-1} at 0.1 nm wave length is accessible with the instrument. The instrument is an excellent choice for time-resolved combined SAXS/WAXS experiments and for high resolution ultra-small angle X-ray scattering.

For the Rayonix MX-170HS detector the differential scattering cross section per unit volume of the solvent and solutions measured with the ID02 were calculated according to the following equation,

$$\left(\frac{d\Sigma}{d\Omega}\right)_S (x,y)(cm^{-1}) = \frac{(N_{(x,y)} - \langle N_{dark(x,y)}\rangle)}{\Delta\Omega_{(x,y)} \times E_{flatfield(x,y)} \times I_1} \times F_{norm} \quad (40)$$

where $N_{(x,y)}$ is the count rate for the sample at the detector pixel with the coordinates (x,y), $\langle N_{dark(x,y)}\rangle$ is the dark count with the same exposure time at the same detector pixel averaged over multiple runs, $\Delta\Omega_{(x,y)}$ is the solid angle of the respective detector pixel, $E_{flat\ field(x,y)}$ is an experimentally normalized flat field measured with a strongly fluorescent and absorbing sample (12% HBr in water) to account for differences in pixel efficiencies and I_1 is the integrated intensity of the outcoming flux measured on the beamstop. F_{norm} is the calibration factor which is defined as the energy dependent normalization factor $F_{norm\ H2O}$=1.63E-3 mm^{-1} at λ=0.1 nm divided by a measurement of water in the same capillary which is used for the samples. During the measurement the outcoming and incoming flux are permanently monitored by a PIN diode, one on the beamstop, coated with a metal foil, receiving the full direct beam, and one well before the sample, measuring photons scattered

by a Kapton foil. Successively an azimuthal integration on the normalized 2D data is performed. The differential scattering cross section per unit volume of the solutions is obtained by subtracting the solvent measurement and a sample background which corresponded to the scattering plateau at q > 4 nm^{-1} and which stems predominantly from free SICs in the sample.

2.2.2.2 I911 SAXS beamline

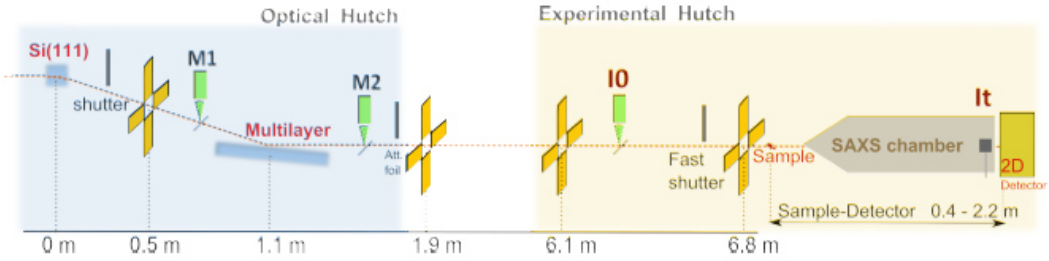

Figure 7: Installation of the I911-SAXS beamline which was located at the MAX-Lab in Lund.[70]

The I911 SAXS beamline, which was installed at MAX-Lab is also a pinhole instrument.[70] Other than the ID02, the instrument works with a fixed wave length of 0.091 nm selected from the white X-ray beam by a Si monochromator. Subsequently the x-ray beam is focused by a Mo-Si multilayer mirror. The intensity of the incoming beam I_0 and the intensity of the transmitted beam I_t is monitored during the complete measurement. The scattering intensity is measured by a Pilatus 1M detector. The sample-distance can be varied in between 0.4 m and 2.2 m. A typical setup covers a q-range from 0.01 $Å^{-1}$ to 0.3 $Å^{-1}$. Lower (0.006 $Å^{-1}$) and higher (2 $Å^{-1}$) q-values are reachable by setup modifications.

The data reduction was done as follows. First of all the scattering of the empty cuvette was subtracted from the water measurement. The values of the resulting scattering curve were averaged in a q-regime from 0.1 $Å^{-1}$ to 0.3 $Å^{-1}$ and the respective variance was calculated. Subsequently the solvent measurement was subtracted from the solution measurement. To get absolute scattering values the resulting scattering curve was divided by the averaged water measurement and multiplied with 0.0162 cm^{-1}, which is the differential scattering cross section of water.

2.2.3 Modell Form Factors

The form factor of scattering particles, which is accessible by small angle scattering experiments, give beside the information of the size and M_w, which can be extracted from the Guinier plateau in the beginning, more information about the shape of the particles.

Beside the basic form factors like a sphere, coil or rod, a large number of more complex model form factors were calculated meanwhile theoretically. Modern SAS fitting software's like "SASVIEW" or "Igor" include these calculated model form factors and give the possibility to adapt these model form factors on the SAS curves by a fitting routine.

In the following the approach for the fitting process is presented. First of all the slope of the SAS curve was analyzed which appears after the Guinier plateau in the Porod regime[68,71,72]. A

slope of -1 is a hint, that the particle is more rod/cylinder like, -2 correlates with a coil-like structure and -4 could be connected to a more sphere-like structure. Those information were taken to select an appropriate model for the fitting process. For each model different fitting parameters are available. For the first approach the standard values were kept and the fitting routine was started. Afterwards the goodness of the fit was checked visually by comparing the fitted curve to the original scattering curve and statistically by the χ^2-value. Subsequently the fitting procedure was repeated by changing single parameters in doing so that the parameters of the fitted model make sense and that the size of the fitted model was approximately in line with the size of the scattering particles measured by light scattering. The fitting procedure was stopped when no improvement was anymore possible.

In the following the model form factors are presented which were used for the analysis of the SAS experiments.

For polymer chains under good solvent conditions an approximate formula is derived by Hammouda et al. for the form factor as[73,74],

$$\frac{d\Sigma}{d\Omega}(q) = \frac{scale}{\nu X^{\frac{1}{2\nu}}}\gamma\left(\frac{1}{2\nu}, X\right) - \frac{1}{\nu X^{\frac{1}{\nu}}}\gamma\left(\frac{1}{\nu}, X\right) + bkg \tag{41}$$

where *s* is a dimensionless scaling factor adjusting P(q) to absolute scattering cross section per unit volume, 1/ν is the Porod exponent, which is the reciprocal fractal dimension of the excluded volume chains, b is the value for any background scattering and γ(s,X) is the incomplete gamma function.

$$\gamma(z, X) = \int_0^X dt\, e^{-t} t^{z-1} \tag{42}$$

X is defined as,

$$X = \frac{q^2 a^2 n^{2\nu}}{6} = \frac{q^2 R_g^2 (2\nu+1)(2\nu+2)}{6} \tag{43}$$

where a is the statistical segment length of the polymer chain and n is the degree of polymerization. The square of the radius of gyration is defined as

$$R_g^2 = \frac{a^2 n^{2\nu}}{(2\nu+1)(2\nu+2)} \tag{44}$$

Polymer chains in their unperturbed state (θ-condition) obey Gaussian chain statistics for long enough chains. This form factor derives from eq 41 in the limit of 1/ν=2 and agrees with the form factor derived by Debye for such Gaussian chains.[68,75] For polydisperse chains obeying a Schulz-Zimm type molecular weight distribution the z-averaged Debye formula reads,

$$\frac{d\Sigma}{d\Omega} = scale\frac{2\left[\left(1+\frac{UR_g^2q^2}{1+2U}\right)^{-\frac{1}{U}}+\left(\frac{R_g^2q^2}{1+2U}\right)-1\right]}{(1+U)\left(\frac{R_g^2q^2}{1+2U}\right)^2}+bkb \quad (45)$$

where U expresses the polydispersity of the chains as

$$U = \frac{M_w}{M_n} - 1 \quad (46)$$

The form factor for collapsed polymer coils, which are expected to exhibit a pearl necklace structure was based on a simple model[26]. This model is composed of the following two elements: N homogeneous spheres of a radius R are freely jointed by M rods of length l, with N=M+1. The length of a rod l is related to the center to center distance A between two neighbouring spheres via l=A-2R. The form factor of the model is calculated according to,

$$\frac{d\Sigma}{d\Omega}(q) = \frac{scale}{V}\times\frac{(S_{ss}(q)+S_{rr}(q)+S_{rs}(q))}{(M\times m_r+N\times m_s)^2}+bkg \quad (47)$$

where V is the volume of the pearl necklace chain. The parameters m_r and m_s are defined as follows,

$$m_r = (SLD_r - SLD_{sv})\times V_r \quad (48)$$

$$m_s = (SLD_s - SLD_{sv})\times V_s \quad (49)$$

SLD_x is the scattering length density of the spheres (s), rods (r) and solvent (sv). V_x is the respective total volume of the rods (r) and spheres (s). In order to reach at V_r a cross section had to be selected for the rods. In the present case a value in between 0.05 and 5 nm was applied. The parameters S_{ss}, S_{rr} and S_{rs} are as follows

$$S_{ss}(q) = 2m_s^2\Psi^2(q)\left[\frac{N}{1-\sin(qA)/qA}-\frac{N}{2}-\frac{1-\left(\frac{\sin(qA)}{qA}\right)^N}{\left(1-\frac{\sin(qA)}{qA}\right)^2}\times\frac{\sin(qA)}{qA}\right] \quad (50)$$

$$S_{rr}(q) = m_r^2\left[M\left\{2\Lambda(q)-\left(\frac{\sin\left(\frac{ql}{2}\right)}{\frac{ql}{2}}\right)\right\}+\frac{2M\beta^2(q)}{1-\sin(qA)/qA}-2\beta^2(q)\frac{1-\left(\frac{\sin(qA)}{qA}\right)^M}{\left(1-\frac{\sin(qA)}{qA}\right)^2}\right] \quad (51)$$

$$S_{rs}(q) = m_r\beta(q)m_s\Psi(q)4\left[\frac{N-1}{1-\sin(qA)/qA} - \frac{1-\left(\frac{\sin(qA)}{qA}\right)^{N-1}}{\left(1-\frac{\sin(qA)}{qA}\right)^2} \times \frac{\sin(qA)}{qA}\right] \quad (52)$$

$$\Psi(q) = 3\frac{\sin(qR) - (qR)\cos(qR)}{(qR)^3} \quad (53)$$

$$\Lambda(q) = \frac{\int_0^{ql}\frac{\sin(t)}{t}dt}{ql} \quad (54)$$

$$\beta(q) = \frac{\int_{qR}^{q(A-R)}\frac{\sin(t)}{t}dt}{ql} \quad (55)$$

If the pearl-like domains of a pearl necklace chain approach each other, the structure gets increasingly cylinder-like and the corresponding form factor may also be described by rigid cylinders.[50] In this case the scattering intensity is given by

$$\frac{d\Sigma}{d\Omega}(q) = \frac{scale}{V}\int_0^{\pi/2} f^2(q,\alpha)\sin\alpha\, d\alpha + bkg \quad (56)$$

with

$$f(q) = 2(\Delta\rho)V\sin(qL\cos\alpha/2)/(qL\cos\alpha/2)\frac{J_1(qr\sin\alpha)}{(qr\sin\alpha)} \quad (57)$$

where V is the volume of the cylinder with the length L and the radius r, α is the angle between the axis of the cylinder and the q-vektor, J_1 is the first order Bessel function and Δρ is difference in scattering length density between the cylinder and the surrounding solvent.

Alternatively a more ellipsoidal shape could also fit to the collapsing particles. A model form factor for ellipsoids was established by Feigin[76],

$$P(q) = \frac{scale}{V}f^2(q) + bkg \quad (58)$$

where f(q) is represented by the following equation,

$$f(q) = \frac{3(\Delta\rho)V(\sin[qr(R_a,R_b,\alpha)] - qr\,cos[qr(R_a,R_b,\alpha)])}{[qr(R_a,R_b,\alpha)]^3} \quad (59)$$

with

$$r(R_a,R_b,\alpha) = [R_b^2 sin^2\alpha + R_a^2 cos^2\alpha]^{1/2} \quad (60)$$

According to the cylinder model, V represents the volume of the ellipsoid, Δρ is the difference in scattering length density in between the particles and the solvent and α is the

angle between the axis of the cylinder and the q-vektor. R_a is the radius along the rotational axis of the ellipsoid and R_b is the radius perpendicular to the rotational axis of the ellipsoid.

As it was already discussed in some cases polyelectrolyte chains in the presence of SICs collapse at states located close to the phase boundary to compact spheres. According to Guinier[50] the form factor of a sphere is defined as follows,

$$\frac{d\Sigma}{d\Omega}(q) = \frac{scale}{V}\left[\frac{3V(\Delta\rho)(\sin(qr) - qr\cos(qr))}{(qr)^3}\right]^2 + bkg \tag{61}$$

where r is the radius of the sphere, V is the volume of the sphere and Δρ is the difference in scattering length density in between the particles and the solvent.

The goodness of the fits were checked visually and mathematically by the χ^2/Npts value, which is defined as follows,

$$\frac{\chi^2}{Npts} = \frac{\sum \frac{\left[\left|x_{i,obs} - x_{i,cal}\right|\right]^2}{x_{i,cal}}}{Npts} \tag{62}$$

where $x_{i,obs}$ is the observed value, $x_{i,cal}$ is the calculated value from the fit and Npts is the number of the data points.

2.3 Isothermal Titration Calorimetry (ITC)

ITC is a common technique in biology or biochemistry for the investigation of protein-protein, protein-ligand interactions or enzyme kinetics.[77–79] ITC instruments are sensitive towards small temperature fluctuations, which are induced by the enthalpy of binding processes or dilution processes. In the present experiments a TAM III instrument from TA instruments was used which is located at the BASF in Ludwigshafen.

The main part of the TAM III instrument is the water tank which is connected to a very accurate thermostat. The sample containers, which include in the following experiments the sample/polyelectrolyte solution is connected over a peltier element with the water tank. By means of a computer controlled syringe pump a solution including the SIC can be added stepwise via a cannula to the sample container. The amount of the injected volume, the volumetric flow and the time between two injections can be programmed before experiment. The sample solution in the container is stirred during the whole experiment at a constant speed.

In the following a short introduction is given how the signal of an ITC experiment arises and in which way the data of the ITC experiment were analyzed. After complete thermal equilibration of the filled sample container an ITC experiment can be started. Subsequently a small volume V_i of the SIC solution is added to the polyelectrolyte solution. The temperature of the solution in the sample container slightly increases in an exothermic reaction or decreases in an endothermic reaction. As a result, the two sides of the peltier element probed different temperatures, which induce a current in the peltier element. The current is

proportional to the heat flow and was recorded over time. The heat flow increases to a maximum level with ongoing reaction and drops back to the baseline once the temperature of the solution recovers the temperature in the water tank. Depending on whether the peak is below or above the baseline, the reaction is identified as exothermic or endothermic. After a certain delay time, the next increment of the SIC solution is titrated to the polymer solution. A typical titration program obeyed the following protocol: in a first step 2µl of SIC solution is added, followed by 80 steps à 10µl added in intervals of 30 min.

Baseline subtraction and integration of the peak provided the heat which was consumed or created by the titration step. The heat per titration step was normalized by division with the molar amount of SICs added by this step,

$$\Delta H_{Mi} = \frac{\Delta \mathrm{H}_{Ri} - \Delta \mathrm{H}_{BGi}}{n_{M^{z+}}} \tag{63}$$

where ΔH_{Ri} is the recorded heat of titration step i, n_{Mz+} is the added molar amount of SIC, and ΔH_{Mi} is the consumed/created heat by the particular reaction step i in kJ per mol of added M^{z+}. From the value of each titration step a background ΔH_{BGi} had to be subtracted, which stemmed from the dilution process of the SICs, while the SIC solution was added to the polyelectrolyte solution. The background subtraction can be done in different ways.

1) By running a solvent measurement performed with the same protocol as has been used for the polyelectrolyte solution but with pure solvent instead of the polyelectrolyte solution.
2) By using the fitted background. The tail of the ITC experiment is used for this fit. It is assumed that in this part of the ITC experiment every binding site in the polyelectrolyte is already bound to the specifically interacting cations. The signal stems then only from the dilution of the SICs. If the signal of titration steps adopts a plateau value, a mean value from data of the plateau is calculated and subtracted from the value of every titration step. If the signal shows a gradient with the number of titration steps instead of a plateau, this gradient is fitted with a linear or quadratic function depending on the shape of the final gradient of the ITC curve. The function resulting from the fit is then used as a pseudo solvent measurement.

As it is outlined in Figure 8, the procedure of the background subtraction slightly influences the final ITC curve. The largest influence is observed at the beginning of an experiment. In case of the subtraction of a fitted background, the results from a quadratic fit function is very close to the original solvent measurement. In the CaPA and BaPA experiments an average value was subtracted from every titration step. In case of the experiments with AlPSS under different solvent conditions a linear function was used. For BaPSS in pure water a quadratic function was utilized while for the BaPSS in inert salt an average value was used for background subtraction. The background subtraction for the CaPSS experiments was done by a solvent titration.

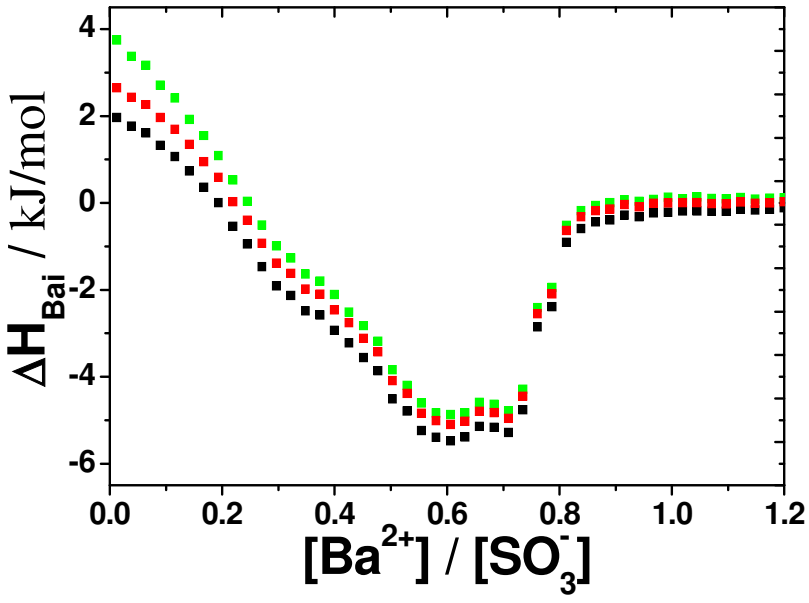

Figure 8: Results from a titration of NaPSS with Ba^{2+} in pure water (experiment BaPSS-1) corrected by subtracting an average value (■), a quadratic fit to the tail of the ITC experiment (■) and a solvent titration done with the same protocol used for the actual ITC experiment (■).

Two ways have been applied to interpret calorimetric data. In one way, ΔH_{Mi} from eq 63 is plotted versus the molar ratio n_{Mz+}/n_{X-} of the SIC M^{z+} and of the monomer X^- of the polyelectrolyte. In the optimum case the ITC curve exhibits a sigmoidal shape which approaches a baseline close to zero and a maximum of ΔH_{Mi} can be extracted from the first titration steps of the ITC experiment. This maximum value is considered to correspond to the molar binding enthalpy.

An additional way to interpret the data is to stepwise add the heat increments after having subtracted the respective background and plot the accumulated heat versus the number of titration steps. This gives a steadily increasing signal, which approaches a plateau when the baseline of the ITC experiment is reached. The maximum value obtained from this curve is divided by the molar amount of monomer groups n_{X-} provided by the starting volume $V(X^-)$ of the polyelectrolyte solution, giving a mean value of the heat which was consumed or created per mole monomer groups of the polyelectrolyte,

$$\Delta H_{X^-} = \frac{\sum_i (\Delta H_{Ri} - \Delta H_{BGi})}{n_{X^-}} \tag{64}$$

3. Experimental Procedures

3.1 Materials

The chemicals applied for this work were purchased from different suppliers. The following table gives an overview of the used chemicals and the respective suppliers.

Table 2: List of the chemicals, which were used for this work and the respective suppliers.

chemicals	supplier
NaCl	Fluka
$BaCl_2$*2 H_2O	
$SrCl_2$	
$BaCl_2$ anhydrous	Sigma Aldrich
$CaCl_2$*6 H_2O	
$AlCl_3$* 6 H_2O	
$AlCl_3$ anhydrous	
h-HPSS-1	
h-NaPSS-3	
D_2O used for SANS in Grenoble	
h-NaPSS-1	PSS – Polymer Standards Service
h-NaPSS-2	
h-NaPSS-4	
NaPA-1	
NaPA-2	
NaPA-3	
D_2O used for SANS in Munich	Deutero
ultrapure water	Millipore device from the technical chemistry department of the university of Paderborn

3.1.1 Drying of the Polyelectrolyte Samples

Polyelectrolytes are a hygroscopic and therefore they always bind a certain amount of water. Hence the polyelectrolyte samples were dried before use in a vacuum oven for at least one hour at 55°C and 30 mbar. In case of the characterization of h-NaPSS-2 and of h-NaPSS-1, in the case of the coil shrinking experiments done with h-NaPSS-2 and in the case of the solutions used for the determination of the phase diagrams established with sample h-NaPSS-2 a fixed value of 11% was subtracted from the initial weights. This value was determined by several dryings of small portions of the polymers in the vacuum oven.

3.2 Evaluation of the Phase Diagrams

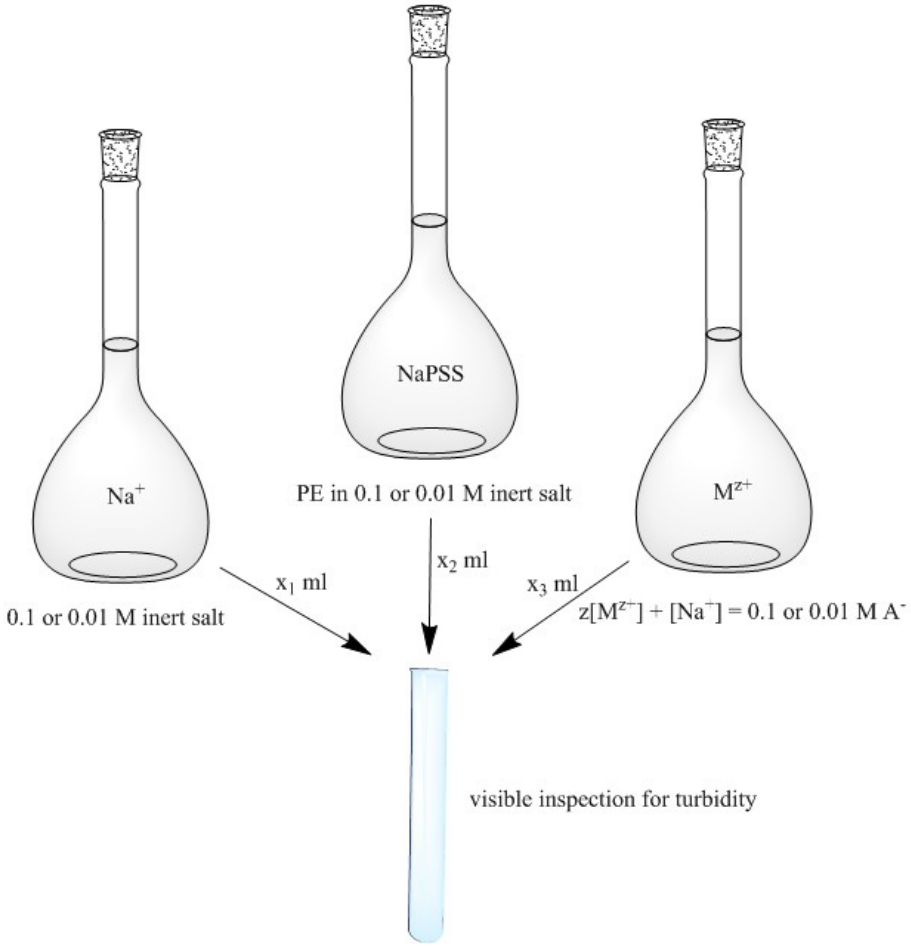

Figure 9: Procedure for the determination of the phase diagram by visible inspection.

At least one phase diagram is established for each SIC-polyelectrolyte combination. For each phase diagram three different stock solutions were prepared first. One stock solution contained [I]=0.1 or 0.01 M inert salt. A second consisted of ~1 g/L polyelectrolyte dissolved in the respective inert salt solution. The polyelectrolyte was gently dissolved by slowly rotating the solution for at least two days. The third solution contained the SIC with $[I]=z[M^{z+}] + [Na^+] = 0.1$ or 0.01. Ultrapure water or D_2O was used as solvent for the stock solutions. Composition of the three stock solutions assured constancy of $[I]=z[M^{z+}] + [Na^+] = [A^-]$. In a few exceptional cases some phase diagrams were established without an inert salt content. In these cases the polyelectrolyte and the SIC were dissolved only in pure water.

To establish the phase diagram of a SIC polyelectrolyte system three different methods were used:

1) Mixtures of the respective polyelectrolyte stock solution and the inert salt stock solution at variable ratios were prepared as starting solutions. These starting solutions were diluted step by step with the SIC stock solution in test tubes and visually inspected for turbidity.
2) The sample preparation proceeded analogously to the case of method 1. The dilution process was carried out in a light scattering cell instead of test tubes. After each addition of an amount of SIC solution the cell was shaken, placed in the goniometer, which was adjusted to a temperature of 25°C and measured 3 times for 10 s at an angle of 40°. The scattering intensity over time was averaged and plotted versus the concentration of the SIC. The phase boundary was calculated by an intersection of two tangents, one which was adjusted to the values recorded at the beginning of the experiment, where just a small increase of the scattering intensity with an increasing SIC-concentration could be observed and one which was adjusted to the values recorded at the end where a strong increase of the scattering intensity with an increasing SIC-concentration could be observed.

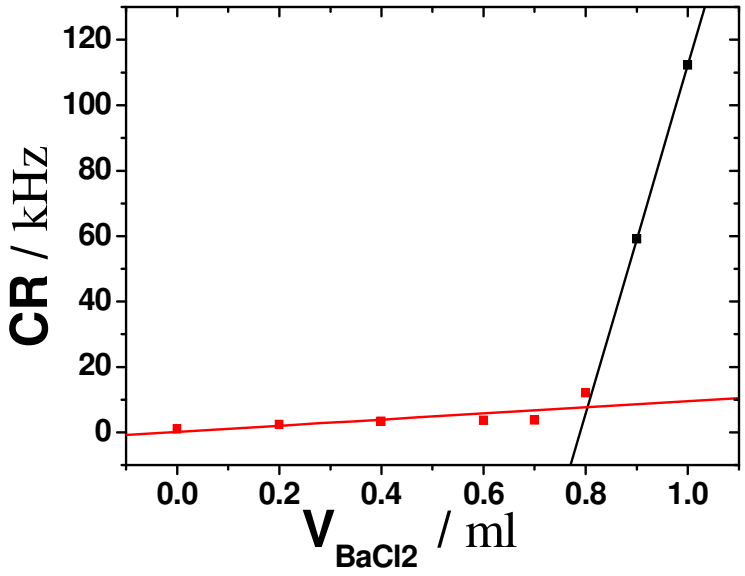

Figure 10: Example for identification of a threshold point by static light scattering at a scattering angle of 40°. The intersection between the black and the red line correspond to the threshold establishing the phase diagram. The example is part of the phase behavior of h-HPSS at pH 3 ([SO_3^-]=5.11 mM) shown in Fig. 34.

Independent from the method every single sample fulfilled the rule that the SIC is introduced into the respective NaPSS solution by replacement of the corresponding amounts of inert salt at constant concentration of the anion (A^-) [I]=0.01 or 0.1 M according to [I]=z*[M^{z+}]+[Na^+]=0.1 or 0.01 M A^-. Only the phase diagrams prepared in pure water and the re-entrant phase experiments deviate from this rule. The following table gives an overview on the different phase diagrams, which were established for this work.

Table 3: List of Phase diagrams which were established for this work.

polyelectrolyte	[I] / M	solvent	SIC	determination of turbidity
h-NaPSS-1	0.1	D_2O	Al^{3+}	visual
h-NaPSS-2	0.1	H_2O	Al^{3+}	visual
h-NaPSS-2	0.01	H_2O	Al^{3+}	visual
d-NaPSS	0.1 M	H_2O	Al^{3+}	visual
h-NaPSS-1	0.1 M	D_2O	Ba^{2+}	visual
h-NaPSS-2	0.1 M	H_2O	Ba^{2+}	visual
h-NaPSS-1	0.1 M	H_2O	Ba^{2+}	light scattering
h-NaPSS-1	---	H_2O	Ba^{2+}	light scattering
h-HPSS-1 pH 3	---	H_2O	Ba^{2+}	light scattering
h-HPSS-1 pH 5	---	H_2O	Ba^{2+}	light scattering
h-NaPSS-3	---	H_2O	Ca^{2+}	visual
h-NaPSS-3	---	H_2O	Sr^{2+}	visual

3.3 Determination of dn/dc for NaPSS in 0.1 M NaCl

Determination of absolute molar mass values of the NaPSS samples by light scattering requires the appropriate dn/dc (eq 5). The determination of dn/dc for NaPSS in 0.1 M NaCl had to be carried out with NaPSS solutions dialysed against 0.1 M NaCl. In the dialysis cell two cylindrical half cells were separated by a dialysis membrane (Fig. 11). First a stock solution of 8.6 g/L NaPSS-4 in 0.1 M NaCl was prepared and gently rotated for one night. At the same time a membrane for the dialysis cell (THOMAPOR-Dialysistube made of cellulosehydrate, Typ: RCT-88-09) was placed over night into aqueous 0.1 M NaCl and successively rinsed with ultrapure water, dried for one hour at ambient condition and inserted into the dialysis cell.[80] One half cell was filled with an aqueous solution of 0.1 M NaCl. The other half cell contained the NaPSS stock solution in 0.1 M NaCl. Both sides were sealed. After 72 h the solvent and the NaPSS stock solution were removed from the respective half-cells and used to prepare a dilution series of the dialysed NaPSS stock solution.[24]

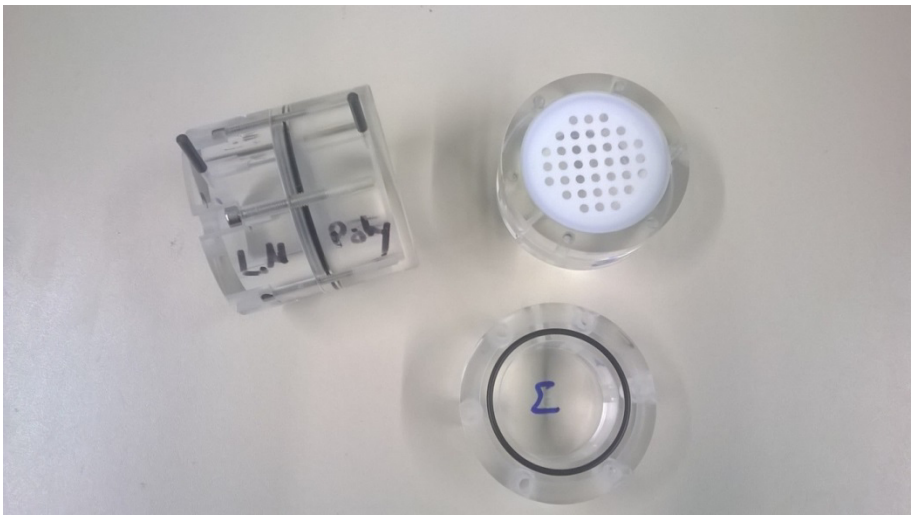

Figure 11: One closed and one opened dialysis cell. The cells were used for the dialysis of the NaPSS solution before determination of dn/dc for NaPSS in 0.1 M NaCl and for sample mixing by dialysis.

A differential refractometer (α-ref version 2.1 by SLS Systemtechnik) was used to determine the dn/dc value from the as prepared dilution series (Fig. 12).[81] The light source of the instrument was a red laser with λ_0=635 nm wavelength. A rectangular cuvette of optical glass with two chambers separated diagonally by a glass slide was used. All dn/dc measurements were performed at 25°C. First both chambers were filled with solvent and equilibrated for some time in the instrument until the signal of the refractive index was constant thereby establishing the reference state. Successively the sample chamber was drained, rinsed and filled with the first polymer solution. To minimize errors due to small amounts of the previous sample, the samples are used in order of increasing polymer concentration.

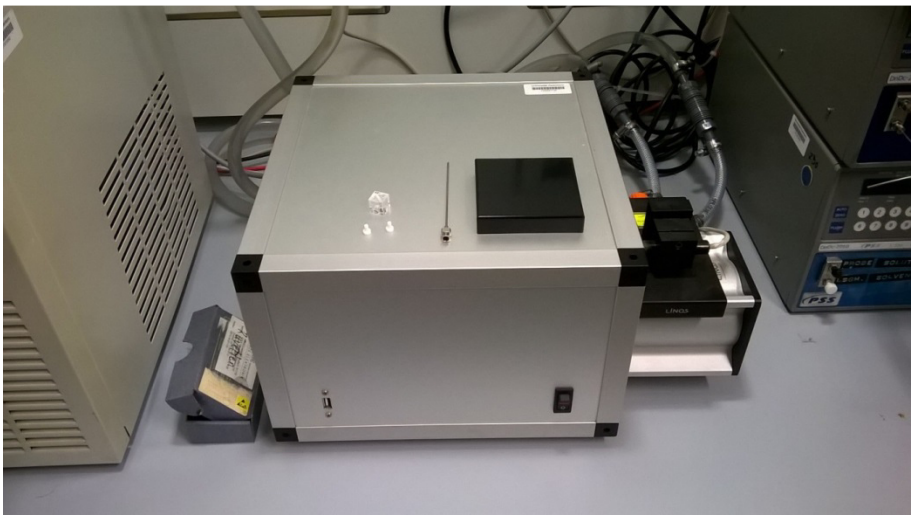

Figure 12: The differential refractometer „α-ref version 2.1" by SLS Systemtechnik was used for the determination of the dn/dc for NaPSS in 0.1 M NaCl.

All samples were measured in the normal and reverse direction. In the reverse case the measurement cell was rotated by 180 degrees compared to the normal case. This results in a negative change in dn. In the final graph the negative dn was plotted versus the

corresponding negative concentration values of the polymer (Fig. 13). The linear regression of the change in the refractive index with NaPSS concentration gives a value of dn/dc=0.1701 ± 0.00074 cm^3/g.

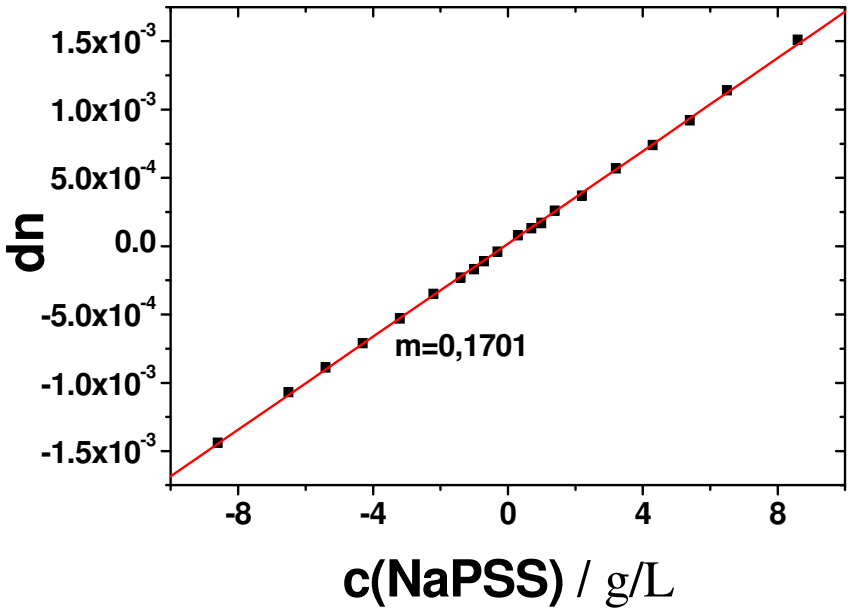

Figure 13: dn/dc measurement of NaPSS dissolved in 0.1 M NaCl solution. The red line shows the linear regression, which exhibits a slope of m=0.170.

3.4 Light Scattering Experiments

For the light scattering experiments done in Paderborn cylindrical Hellma cells made out of SUPRASIL quartz glass with a diameter of 25 mm were used. Prior to its use the scattering cuvettes were cleaned several times with aqueous detergents and rinsed with distillated acetone. Light scattering measurements are very sensitive towards dust particles incorporated in the light scattering cell. Therefore the cells were rinsed additionally for at least 10 minutes in an acetone fountain after cleaning. To get rid of the dust particles in the solvents and solutions, they were filtered with cellulose-mixed-ester filters with 200 or 450 nm pore sizes (Macherey-Nagel Chromafil A-20/25 and Macherey-Nagel Chromafil A-45/25) into the pre-cleaned scattering cuvettes. Because of some dust particles which could remain from the production process in the filter, the first 2 ml - 3 ml solution which leaves an unused filter are always discarded.

In case of the light scattering experiments performed in line with the SANS and SAXS experiments at the ILL, simple reaction tubes with a diameter of 10 mm were used as cuvettes. Because of the absence of an acetone fountain, the reaction tubes were rinsed before use several times with distillated acetone.

All light scattering experiments were performed at a constant temperature of 25°C except of the temperature dependent light scattering experiments.

3.4.1 Characterization of the Polyelectrolyte Samples

For the interpretation of the coil shrinking experiments it is necessary to know a reference value of the polymer sample. Therefore a characterization of the polymer by static and dynamic light scattering is done beforehand in the absence of SICs, which gives information about the non-apparent values of R_g, R_h, M_w extrapolated on c=0. The A_2-parameter which can be obtained by using a Zimm plot gives additional information about the quality of the characterized polymer. The second virial coefficient should be positive for NaPA and NaPSS dissolved in a 0.1 or 0.01 M inert salt solution. If the A_2-parameter obtains negative values, the polymer coils in the solution tend to aggregate. In that case this particular polyelectrolyte sample could not be used for the further shrinking experiments. Because in case of experiments in the presence of SICs it is important that the single coil behavior can be investigated by light scattering.

For each polyelectrolyte sample a stock solution was prepared by dissolving 20 mg of NaPSS in 20 ml of the respective inert salt solution. In case of NaPA the solutions were adjusted to a pH of 8-9. The polyelectrolyte solutions were gently dissolved for three days by rotation. Successively, a dilution series was made. The solvent was the same inert salt solution which was used for the polyelectrolyte solution. Solvents and solutions were filtered with cellulose-mixed-ester filters (Macherey-Nagel Chromafil A-20/25 for inert salt-solution and h-NaPSS-1 / Macherey-Nagel Chromafil A-45/25 for the other polyelectrolyte solutions) into pre-cleaned scattering cuvettes and characterized with the ALV 5000E Compact Goniometer System. In case of sample NaPA-1 the modified Fica 50 light scattering instrument was used. The resulting parameters were obtained by Zimm analysis. Table 4 gives a summary of the polyelectrolytes with their respective solvent, which were characterized for this work. The results of the characterizations can be found in chapter 4.1.

Table 4: List of the characterized polyelectrolyte samples.

polyelectrolyte	solvent
h-NaPSS-1	0.1 M NaCl
h-NaPSS-2	0.1 M NaCl
d-NaPSS	0.1 M NaCl
NaPA-1	0.01 M $NaNO_3$
NaPA-2	0.01 M NaCl

3.4.2 Light Scattering Experiments on Selected Points in the Phase Diagram

Light scattering experiments on selected points in the established phase diagrams were performed to get information about the shape and size of the polyelectrolyte coils in the respective states. The polyelectrolyte, inert salt and SIC stock solutions were prepared

according to the same procedure, applied for the preparation of the phase diagrams outlined in chapter 3.1 as method 2. The sample preparation was with some exceptions analogous to the method which is described in Figure 9. Instead of a reaction tube a pre-cleaned light scattering cell was used and each stock solution was filtered into the light scattering cell (Macherey-Nagel Chromafil A-20/25 for inert salt-solution and SIC solutions / Macherey-Nagel Chromafil A-45/25 for the polyelectrolyte solutions). The measurements were performed with the ALV 5000E Compact Goniometer System. Evaluation of the SLS and DLS data was based on eq. 13 and eq. 27 neglecting the concentration dependent part in both equations.

For PSS in the presence of Ba^{2+} and Al^{3+} different sample series were prepared. The samples which belong to one sample series were made out of a single polyelectrolyte stock solution and SIC stock solution respectively. The sample series and the composition of the samples which belong to these series are listed in Table 5.

Table 5: Overview of the samples investigated by combined SLS/DLS at constant temperature connected with information about the sample compositions.

system/polymer	series	sample	[I]	$[SO_3^-]$/mM	$[M^{z+}]$/mM	$[M^{z+}]/[SO_3^-]$
AlPSS/h-NaPSS-2	h-AlPSS-1	3-3-0.1	0.1	2.15	0.55	0.25
		3-3-0.4		2.05	2.08	1.02
		3-3-0.5		2.02	2.56	1.27
	h-AlPSS-2	3-3-0.2	0.1	2.09	1.08	0.51
		3-3-0.3		2.06	1.59	0.77
		3-3-0.4		2.02	2.08	1.03
		3-3-0.5		1.99	2.56	1.29
	h-AlPSS-3	1.5-4.5-0.1	0.1	1.06	0.54	0.51
		1.5-4.5-0.4		1.01	2.1	2.05
AlPSS/d-NaPSS	Dialysis	1	0.1	1.99	2.19	1.10
		2		1.94	2.37	1.22
		4		2.03	2.59	1.28
		6		1.95	0.84	0.43
		7		1.84	1.25	0.68

		8		2.02	1.55	0.77
BaPSS/h-NaPSS-2	BaPSS-3	3-1	0.1	1.44	16.67	11.58
		3-2		1.66	11.54	6.95
		3-3		1.96	4.55	2.32
		3-4		2.12	0.82	0.39
	BaPSS-4	4-1	0.1	0.72	16.67	23.15
		4-2		0.98	4.55	4.64
	BaPSS-5	5-1	0.1	0.72	16.67	23.15
		5-2		1	11.54	11.54
		5-3		2.16	16.67	7.72
		5-4		2.52	16.67	6.62

The samples of series BaPSS-3, BaPSS-4 and BaPSS-5 in case of PSS in the presence of Ba^{2+} system and h-AlPSS-1, h-AlPSS-2 and h-AlPSS-3 in case of PSS in the presence of Al^{3+} were investigated several times over a longer time period. To get information about the SIC depended shrinking of the polyelectrolyte coils the values for R_g, R_h and M_w were plotted versus the respective $[M^{z+}]/[SO_3^-]$ ratio of the sample. In case of BaPSS and AlPSS the mean values of R_g, R_h and M_w for each sample obtained from the single measurements were plotted versus the respective $[M^{z+}]/[SO_3^-]$ ratio.

The method typically used for combining the SIC stock solutions with the NaPSS solution for light scattering is to filter gently dropwise the SIC solution into the filtered polyelectrolyte solution. This may lead to strong, locally confined concentration fluctuations which may generate non-equilibrium morphologies like aggregates. In order to avoid such undesirable states, one sample series was established with sample d-NaPSS at [I]=0.1 M in which the NaPSS stock solution and the $AlCl_3$ solution was mixed by means of a dialysis cell. Dialysis is a more gentle method to bring the two solutions in contact with each other. For the experiment the NaPSS, NaCl and $AlCl_3$ stock solutions were prepared in the same way as applied for the determination of the phase diagrams. $AlCl_3$ solutions with different concentrations were established with the help of the $AlCl_3$ and NaCl stock solution. The membrane and dialysis cells were prepared with the same protocol applied for the dn/dc measurement [Chapter 3.3]. One half cell was filled with the NaPSS solution at [NaCl]=0.1 M while the other half cell was filled with one of the $AlCl_3$ solutions. Whereas $AlCl_3$ spread over both chambers, d-NaPSS did not. The concentrations of all components in the two chambers were selected in order to address distinct states at variable ratio $[Al^{3+}]/SO_3^-]$ in the stable

solution phase, achieved at the end of dialysis after mixing the two equilibrated solutions. Subsequently the cells were closed and stored for at least 6 days. After dialysis the solutions of both half cells were mixed in a vial. Each sample was filtered with cellulose-mixed-ester filters (Macherey-Nagel Chromafil A-45/25) into light scattering cells and measured by combined SLS/DLS.

For BaPSS and AlPSS additional temperature dependent shrinking experiments were performed. Each system was investigated with a slightly different method. The sample preparation was analogous to the method described in the same chapter above.

In case of AlPSS two samples were selected, which were located slightly above and below the phase boundary (Tab. 6). The temperature was changed stepwise. After each temperature shift the samples were equilibrated in the goniometer for half an hour, before the next light scattering measurement was started. The experiments were performed again with the ALV 5000E Compact Goniometer System. At the end the R_g, M_w and R_h values were plotted versus the respective sample temperature.

The three samples for BaPSS had the same Ba^{2+}-concentration but differed in the NaPSS concentration (Tab. 6). In these cases the development of the R_g, R_h and M_w values after each temperature step was followed by a time resolved SLD/DLS experiment. After each equilibration of the sample the values for R_g, R_h and M_w end up into a plateau. A mean value of R_g, R_h and M_w and the respective standard deviation was calculated from the plateau values and plotted versus the respective sample temperature. The measurements were performed with the ALV Multidetection Laser Light Scattering Goniometer System (ALV/CGS-3/MD-B).

Table 6: Overview of the samples investigated at different temperatures by SLS/DLS connected with information about the sample compositions.

System/polymer	sample	[I]	$[SO_3^-]$/mM	$[M^{z+}]$/mM	$[M^{z+}]/[SO_3^-]$
AlPSS/h-NaPSS-2	AlPSS-temp-1	0.1	2.02	2.08	1.03
	AlPSS-temp-2		2.6	3	1.15
BaPSS/h-NaPSS-2	BaPSS-temp-1	0.1	1.61	16.67	10.35
	BaPSS-temp-2		1.64	16.67	10.16
	BaPSS-temp-3		0.82	16.67	20.33

Additionally we were interested in the aggregation of the polyelectrolyte complexes which takes place if the aggregation threshold is passed. The experiments were performed with BaPSS.

Table 7: Overview of the samples investigated for the SLS/DLS aggregation experiments.

System/polymer	sample	[I]	$[SO_3^-]$/mM	$[M^{z+}]$/mM	$[M^{z+}]/[SO_3^-]$	method
BaPSS/h-NaPSS-2	BaPSS-CM-1	0.1	2.61	17.5	6.7	component mixing
	BaPSS-CM-2		2.61	18.5	7.09	
	BaPSS-CM-3		2.61	18.5	7.09	
BaPSS/d-NaPSS	BaPSS-TI-1		1.37	21.63	15.79	temperature induced
BaPSS/h-NaPSS-2	BaPSS-TI-2		1.61	16.67	10.35	

The sample preparation was analogous to the method described in the beginning of the same chapter. Two different methods were applied:

1) Samples were mixed with compositions close to the phase boundary. After addition of the three stock solutions to the light scattering cuvette, the sample in the cuvette was shaken for some seconds by hand. Successively the cuvette was transferred into the goniometer and the TR experiment was started immediately. The drawback of this method is that the samples in this area are very sensitive towards small changes in the SIC content. If the SIC content is slightly too high, the PSS coils aggregate very fast and the sample becomes turbid within minutes. In that case the aggregation is hard to follow and becomes impossible when the sample is turbid. If the SIC content is slightly too small, it could happen that either the NaPSS coils shrink but don't aggregate or it takes a long time until the aggregation process starts. Therefore this method turned out to be hard to handle. The advantage of the method is that the sample is the whole time in thermal equilibrium, which makes kinetic studies possible.
2) For the second method the aggregation process is started via a temperature jump. In this case one benefits from the temperature sensitive binding of the SIC towards the polyelectrolyte. The advantage of the method is that the aggregation can be tuned very easy via the temperature and that the process is reversible via temperature jump into the other direction. Hence, one single sample can be used for a series of aggregation experiments. The Disadvantage is that the aggregation can set in before the sample temperature reaches the desired value, which can influence the kinetics of the process and makes kinetic studies more difficult.

Independent of the method, the ALV Multidetection Laser Light Scattering Goniometer System (ALV/CGS-3/MD-B) was used to perform the experiments. Table 7 gives an overview of the samples which were used for the aggregation experiments.

3.5 Small Angle Scattering Experiments

3.5.1 SANS on AlPSS with Deuterated NaPSS at the FRMII

The sample d-NaPSS was utilized for a SANS experiment in H_2O as solvent. Based on the phase diagram established for d-NaPSS in 0.1 M NaCl in the presence of $AlCl_3$ one composition was selected as highly suitable for SANS. Preparation was based on three solutions: a polymer solution with 1.12 g/L d-NaPSS in 0.1 M NaCl, an aqueous 0.1 M NaCl as solvent and an $AlCl_3$ solution with 0.0333 M $AlCl_3$ at $3[Al^{3+}] + [Na^+] = 0.1$. Ultrapure water was used as solvent. The three solutions were mixed as follows to prepare the sample denoted as M-S-1: 4 ml of 1.12 g/L d-NaPSS + 4 ml 0.1 M NaCl + 0.8 ml 0.0333 M $AlCl_3$. The respective solvent was prepared with 8 ml 0.1 M NaCl + 0.8 ml 0.0333 M $AlCl_3$. Sample and solvent were stored for a few hours at room temperature prior of being transferred partially to Hellma cells with a sample thickness of 1mm for SANS and partially to light scattering cuvettes for SLS/DLS after return to the laboratory of the University of Paderborn.

Table 8: Overview of the samples investigated by SLS/DLS/SANS at constant temperature connected with information about the sample compositions. Red colored samples were not measured by SANS.

System/polymer	series	sample	[I]	$[SO_3^-]$/mM	$[M^{z+}]$/mM	$[M^{z+}]/[SO_3^-]$
AlPSS/d-NaPSS	d-AlPSS-1	V-M-1	0.1	2.57	0.81	0.32
		V-M-2		2.56	0.92	0.36
		V-M-3		2.55	1.08	0.42
		M-S-II		2.52	1.2	0.48
		3-3-0.4		2.45	2.08	0.85
		3-3-0.5		2.41	2.56	1.06
		M-S-I		2.38	3.03	1.27

The sample preparation and measurements were performed with the same protocol and instrument outlined in chapter 3.4.1. Macherey-Nagel Chromafil A-20/25 filters were used for the solvent and Macherey-Nagel Chromafil A-45/25 for the sample. Evaluation of the SLS and DLS data was based on eq. 13 and eq. 27 neglecting the concentration dependent part in both equations.

The SANS experiment with sample M-S-I was performed with the KWS-3 at JCNS located at the MLZ in Garching, Munich.[82] The sample was analyzed at a sample-to-detector distance of

1.3 m with a wavelength of λ = 12.8 Å, providing a q range of 0.015 nm^{-1} ≤ q ≤ 0.2 nm^{-1}. For the data reduction empty beam, direct beam, empty cell, solvent and sample were measured. The data reduction was carried out with the official software (QtiKWS), which is provided by the institute.[83] The sample cell and solvent cell were placed in a movable, motor-driven, tempered rack, which was connected to a thermostat. During the experiment the temperature was kept constant at 25°C.

3.5.2 SANS and SAXS Study on AlPSS and BaPSS with Hydrogenated NaPSS at the ILL and ESRF

A joint SANS/SAXS experiment was performed with the sample h-NaPSS-1 in D_2O containing 0.1 M NaCl in the presence of Al^{3+} and Ba^{2+}. To this end four suitable samples for the AlPSS system and 12 samples for the BaPSS system subdivided into two series were selected by means of the corresponding phase diagram (h-NaPSS-1 in D_2O with $z[M^{z+}] + [Na^+] = 0.1$ M). Sample preparation proceeded analogously to the procedure outlined in chapter 3.5.1 now using D_2O instead of H_2O.

All samples from one series contained the same concentration of polymer but differed in the content of M^{z+} and Na^+ (Tab. 9). All samples are located in the regime of stable solutions of the respective phase diagram. The as prepared samples were stored overnight on a roll mixer. Prior to the SANS experiment one part of each sample was filtered into a light scattering cuvette, while the other part was filtered into a Hellma cell. This enabled characterization of the samples before and during the SANS experiment also by light scattering. The sample preparation was performed with the same protocol outlined in the section which describes the characterization of the NaPSS samples. Macherey-Nagel Chromafil A-20/25 for solvents and samples. The light scattering experiments were performed with an ALV Compact Goniometer System 3 (ALV CGS-3) at 25°C at the Institut Laue Langevin (ILL) in Grenoble, France. Evaluation of the SLS and DLS data was based on eq. 12 and eq. 27 neglecting the concentration dependent part in both equations.

The SANS experiments were carried out with the D11 at the ILL. The samples were analyzed at a sample-to-detector distance of 1 m, 8 m and 34 m with a wavelength of λ = 6 Å making available a q range of 0.019 nm^{-1} ≤ q ≤ 5.2 nm^{-1}. For the data reduction empty beam, direct beam, empty cell, H_2O, solvent and sample was measured. The standard H_2O was measured in cuvettes with a sample thickness of 1 mm, all the other solutions and the solvent were measured in cuvettes with 5 mm sample thickness. The samples were placed in a movable, motor driven rack, which was connected to a thermostat. During the experiment the temperature was kept constant at 25°C. The data reduction was carried out with the official software (LAMP), which was provided by the institut.[84]

The samples AlPSS-S-1, AlPSS-S-8, BaPSS-S1-5, BaPSS-S1-6, BaPSS-S2-4 and BaPSS-S2-6 which were measured by combined SLS/DLS and SANS, were also measured by SAXS. To this end the content of the respective light scattering cuvette was used for the experiment.

Table 9: Overview of the samples investigated by SLS/DLS/SANS at constant temperature connected with information about the sample compositions. Red colored samples were not measured by SANS.

system/polymer	series	sample	[I]	$[SO_3^-]$/mM	$[M^{z+}]$/mM	$[M^{z+}]/[SO_3^-]$
AlPSS/h-NaPSS-1	AlPSS-S	AlPSS-S-1	0.1	2.91	1.73	0.6
		AlPSS-S-2			1.8	0.62
		AlPSS-S-3			1.83	0.63
		AlPSS-S-4			1.9	0.65
		AlPSS-S-5			1.97	0.68
		AlPSS-S-6			2.03	0.7
		AlPSS-S-7			2.08	0.72
		AlPSS-S-8			2.17	0.74
BaPSS/h-NaPSS-1	BaPSS-S1	BaPSS-S1-1	0.1	1.45	5	1.72
		BaPSS-S1-2			9	6.19
		BaPSS-S1-3			10	6.87
		BaPSS-S1-4			10.75	7.39
		BaPSS-S1-5			11.5	7.9
		BaPSS-S1-6			12	8.25
	BaPSS-S2	BaPSS-S2-1	0.1	2.91	10	3.44
		BaPSS-S2-2			10.75	3.69
		BaPSS-S2-3			11.25	3.87
		BaPSS-S2-4			11.5	3.95
		BaPSS-S2-5		2.96	11.75	3.97
		BaPSS-S2-6			13	4.39

The experiments were carried out with the ID02 located at the European Synchrotron Radiation Facility (ESRF) in Grenoble, France. The samples were analyzed at a sample-to-detector distance of 1.5 m with a wavelength of λ = 0.1 nm corresponding to a q range of 0.055 $nm^{-1} \leq q \leq 4\ nm^{-1}$. The samples were measured in a flow-through quartz capillary. The

high intensity of the x-ray beam can cause radiation damage in the sample. To minimize these damages the samples were measured sequentially 10 times for 1s. The measurements showed radiation damage in all samples [Chapter A2 in the appendix]. Therefore only the first run of both samples was further used. Absolute values were obtained by calibrating with water. During the experiment the temperature was kept constant at 25°C.

3.5.3 SAXS on BaPA at the ESRF

Polymer sample NaPA-1 was used for the experiment. With the help of the BaPA phase diagram in 0.01 M NaCl, established by Ralf Schweins[13], five samples from the stable part of the phase diagram were selected for the SAXS experiment. The samples contained the same NaPA concentration but differed in the content of Ba^{2+} and Na^{+} with $2*[Ba^{2+}] + [Na^{+}] = 0.01$ M Cl^{-} (Tab. 10). The sample preparation was done analogous to the procedure described in chapter 3.4.2. The inert salt solution contained 0.01 M NaCl. The pH of the inert salt solution and the NaPA solution in 0.01 M NaCl was adjusted to 8-9. The Ba^{2+}-solution contained 0.005 M $BaCl_2$. The 5 samples were characterized beforehand by SLS/DLS with the help of the ALV 5000E Compact Goniometer System in Paderborn. Afterwards the samples were send to Grenoble where they were measured at the ID02 at the European Synchrotron Radiation Facility (ESRF) in Grenoble, France. The samples were analyzed in a flow-through quartz capillary at a sample-to-detector distance of 1 m and 30 m with a wavelength of $\lambda = 0.995$ nm corresponding to a q range of $0.002\ nm^{-1} \leq q \leq 7\ nm^{-1}$. Absolute values were obtained by calibrating with water. During the experiment the temperature was kept constant at 25°C.

Table 10: Overview of the BaPA samples measured in the SAXS experiment in Grenoble.

sample	[I]	$[COO^{-}]$/mM	$[M^{z+}]$/mM	$[M^{z+}]/[SO_3^{-}]$
S1	0.01	1.55	0.83	0.54
S2			0.75	0.48
S3			0.67	0.43
S4			0.58	0.38
S5			0.42	0.27

3.5.4 SAXS on BaPA at MAX-lab

The experiment was a repetition of the experiment described in chapter 3.5.3. but with polymer sample NaPA-2 instead of NaPA-1. The experiments were performed at MAX-lab in Lund. Four stable samples, determined again with the help of the BaPA phase diagram in 0.01 M NaCl, were mixed with the same procedure described in chapter 3.5.3. These samples were also characterized beforehand by static and dynamic light scattering with the ALV 5000E Compact Goniometer System in Paderborn. Additionally a stock solution of the NaPA and 4 different SIC stock solutions were prepared which had to be mixed in Lund in a 1:1 ratio to create similar but fresh samples which were already mixed and characterized in

Paderborn. The completed samples and stock solutions were sent to MAX-lab in Lund where the aged and freshly prepared samples were measured at the I911-SAXS beamline. All measured samples contained the same NaPA concentration but differed in the content of Ba^{2+} and Na^{+} (Tab. 11) with $2*[Ba^{2+}] + [Na^{+}] = 0.01$ M Cl^{-}. The samples were analyzed by SAXS in a glass capillary with a diameter of 1.5 mm at a sample-to-detector distance of 1.9 m with a wavelength of $\lambda = 0.091$ nm corresponding to a q range of $0.08\ nm^{-1} \leq q \leq 4.89\ nm^{-1}$. Absolute values were obtained by calibrating with water. During the experiment the temperature was kept constant at 25°C.

Table 11: Overview of the BaPA samples measured in the SAXS experiment in Lund.

series	sample	[I]	$[COO^{-}]$/mM	$[M^{z+}]$/mM	$[M^{z+}]/[SO_3^{-}]$
BaPA-MAX-lab-O	O1	0.01	1.56	0.83	0.54
	O2			0.75	0.48
	O3			0.67	0.43
	O4			0.58	0.38
BaPA-MAX-lab-T	T1	0.01	1.56	0.83	0.54
	T2			0.75	0.48
	T3			0.67	0.43
	T4			0.58	0.38

3.6 Isothermal Titration calorimetry (ITC)

3.6.1 Preparation of the ITC Experiments

Table 12: Polymer samples used for isothermal titration calorimetry experiments (ITC)

Sample	Supplier	Polymer	M_w / g/mol	PDI
NaPSS-3	Sigma-Aldrich/Fluka	NaPSS	75600	<1.2
NaPA-3	PSS-Polymer Standards Service	NaPA	131200	1.67

For each ITC experiment two stock solutions were prepared. One stock solution contained $1.2\ g/L \leq [PE] \leq 8.6\ g/L$ of the polyelectrolyte. The polyelectrolytes were dried beforehand for 1 h at 60 mbar and 55°C in a vacuum oven. Pure water or aqueous NaCl solutions were used as solvent. The second stock solution contained the specifically interacting cation (SIC) dissolved in pure water at concentrations in a regime of $0.033\ M \leq [M^{z+}] \leq 2\ M$. Three cations, Ba^{2+}, Ca^{2+}, Al^{3+} were used as SIC. The compositions of the stock solutions for each experiment are listed in Table 1. The as prepared stock solutions were stored at ambient

conditions. In case of ITC experiments in the presence of NaCl as an inert salt the composition of the stock solutions solution assured constancy of $z[M^{z+}]+[Na^+]=[I]=0.1$ M during the titration process.

Table 13: Protocol of the ITC experiments

Experiment	$[X^-]$ / mol/L	$V(X^-)$ / mL	$[M^{z+}]$ / mol/L	solvent for X^-	Sequence of increments of V_i
CaPA-1	0.0512	9.5	1.031	pure water	1*1.905µL + 80*9.948µL
CaPA-2	0.0512	9.5	1.031	pure water	1*1.905µL + 80*7.938µL
BaPA-1	0.05	9.5	1.002	pure water	1*1.905µL + 41*7.937µL
BaPA-2	0.051	9.5	1.002	pure water	1*1.905µL + 60*7.937µL
AlPSS-pH3-1	0.0402	9.5	0.395	pure water	1*4.974µL + 80*11.959µL
AlPSS-pH3-3	0.0291	9.5	0.395	pure water	1*4.974µL + 124*7.938µL
AlPSS-pH6-1	0.0387	9.5	0.395	pure water	1*4.974µL + 110*8.89 µL
AlPSS-pH6-2	0.0291	9.5	0.395	pure water	1*4.974µL + 124*7.938µL
AlPSS-NaCl-pH3-1	0.006	9.5	0.033	0.1 M NaCl	1*9.79µL + 119*19.844µL
AlPSS-NaCl-pH3-2	0.006	9.5	0.033	0.1 M NaCl	1*9.79µL + 124*19.844µL
BaPSS-1	0.0411	9.5	1.012	pure water	1*4.974µL + 80*9.948µL
BaPSS-2	0.0417	9.5	1.013	pure water	1*4.974µL + 94*7.938µL
BaPSS-3	0.0217	9.5	1.013	pure water	1*4.974µL + 99*9.948µL
BaPSS-NaCl-1	0.0066	5	0.050	0.1 M NaCl	1*9.79µL + 124*19.844µL
BaPSS-NaCl-option	0.0039	8.4	0.118	0.06 M NaCl	1*9.744µL + 125*19.844µL
CaPSS-1	0.0217	9.5	1.969	pure water	1*4.974µL + 99*9.948µL
CaPSS-2	0.0223	9.5	1.969	pure water	1*4.498µL + 249*9.79µL

The ITC experiments were performed at 25°C with a TAM III thermostat from TA instruments. Prior to its use in an ITC experiment the polyelectrolyte solution was degassed for 10 minutes. A volume of 5 ml ≤ $V(X^-)$ ≤ 9.5 ml of the degassed polyelectrolyte solution with $X^-=COO^-$ or SO_3^- was filled into the sample container and the sample container was

connected with the stirrer. The entire unit was equilibrated overnight at 25°C in the calorimeter.

The sample container was connected by a peltier element to the water tank of the calorimeter, which was controlled by a thermostat. The SIC solution was uptaken by a syringe, which was connected by long, flexible cannula with the sample container. The syringe was placed in the computer controlled titration unit. Successively a program routine was started and an internal dynamic calibration of the calorimeter was performed. After an additional waiting time the experiment was started. Experiments and their protocols are listed in Table 13.

3.6.2 Procedure of the Turbidity Experiments

To unravel the spike-like peaks in the ITC diagrams, optical titration experiments were carried out with the same protocol, which was used for the correspondent ITC experiment. With the help of the optical titration experiment, the sample composition was determined where the polyelectrolyte-SIC complex begins to precipitate. For the turbidity experiments stock solutions with the same concentrations were prepared, which have been used for the ITC experiments. A polyelectrolyte stock solution was transferred to a vial containing a magnetic stirring bar. Afterwards small aliquots of the SIC stock solution were added under stirring to the NaPSS stock solution. After each addition the sample was repeatedly checked visually for turbidity.

3.6.3 Procedure of the DLS Measurements Reproducing Experiment BaPSS-3

Stock solutions were prepared with the same concentrations, as have been used for the BaPSS-3 ITC experiment. The NaPSS stock solution was filtered in a light scattering cuvette by a Macherey-Nagel Chromafil A-20/25 filter and measured at an angle of 40° with the ALV 5000E Compact Goniometer System (ALV 5000E CGS). Successively small volume increments of the $BaCl_2$ solution were added to the NaPSS solution in the cuvette. After addition of each aliquot of $BaCl_2$ the cuvette was placed in the goniometer and measured again. The procedure was repeated until the solution became visually turbid. The corresponding field-time correlation functions g1(τ) were analyzed in the following by a biexponential fit,

$$g_1(\tau) = b + \mu_1 \times e^{-\Gamma_1 \times \tau} + \mu_2 \times e^{-\Gamma_2 \times \tau} \tag{65}$$

where b is the value for the baseline and μi and Γi have the equal meaning as in eq 22, 23 and 24. As a result the apparent Diffusion coefficient D_1, D_2 and $D_{average}$ is obtained. The diffusion coefficient D_x was used to calculate the effective hydrodynamic radius R_h via eq 28.

4. Results and Discussions

4.1 Characterization of the NaPSS and NaPA Samples

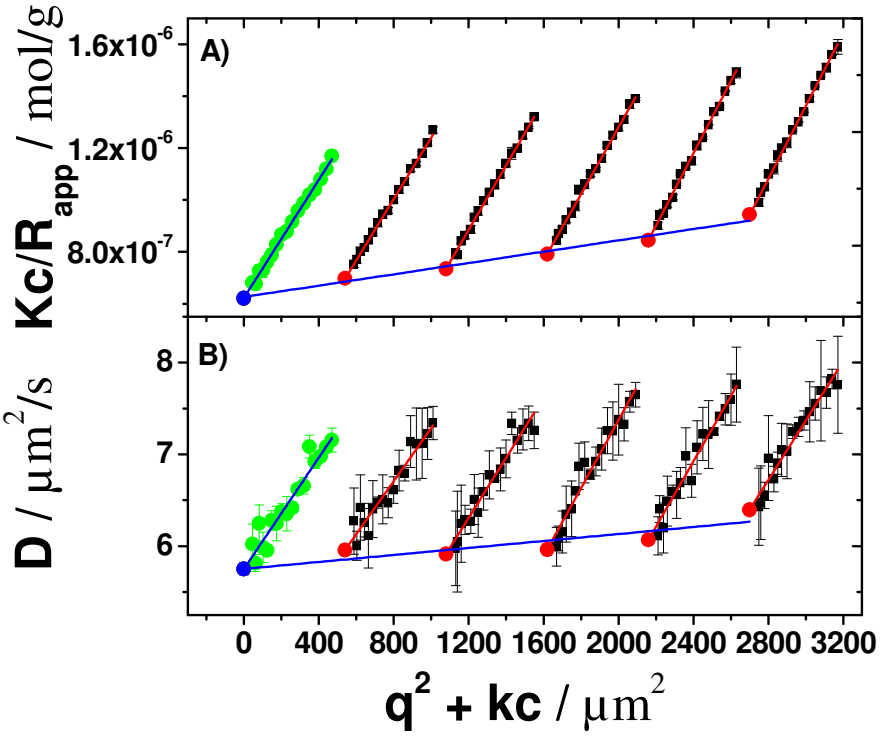

Figure 14: Zimm-plot of sample h-NaPSS-1 at 25°C and [I]=0.1. The results of the Zimm-plot are listed in table 14.

A characterization of the polymer is necessary when R_g and M_w values are to be determined which are not affected by the second virial coefficient. The characterizations of the different polyelectrolyte samples were done by the method described by Zimm.[49] First a dilution series of the polymer has to be prepared, which is measured by light scattering. In the Zimm-plot, Kc/R is plotted versus q^2+kc, whereby k is an arbitrary constant and c is the concentration of the respective sample. Each scattering curve is extrapolated by means of the Zimm equation (eq 12) towards q^2=0 (red lines in Fig. 14 A, 15 A and 17 A). The different q^2=0 values which are denoted by red dots in the Zimm-plots are extrapolated afterwards versus c=0 (lower blue line Fig. 14 A, 15 A and 17 A). The slope of the regression correlates with $2*A_2$, while the intercept is the reciprocal M_w value which is not affected by the second virial coefficient. Additionally an extrapolation of the Kc/R values, which exhibit the same scattering angle, versus c=0 is done (green circles in Fig. 14 A, 15 A and 17 A). The different versus c=0 extrapolated values are fitted successively via linear regression towards q^2=0, whereby the slope correlates with $R_g^2/3M_w$ and the intercept represents again the reciprocal M_w value. The extrapolation of the diffusion coefficients following equation 27 is done by the same protocol. The intercepts of both blue lines correlates with the q^2=0 and c=0 extrapolated diffusion coefficient D_z (Fig. 14 B, 15 B, 17 B and 18 B) which can be converted to the respective hydrodynamic Radius via eq 28. The slope of the lower blue line in Figure 14, 15, 17 and 18 represents the k_D-value.

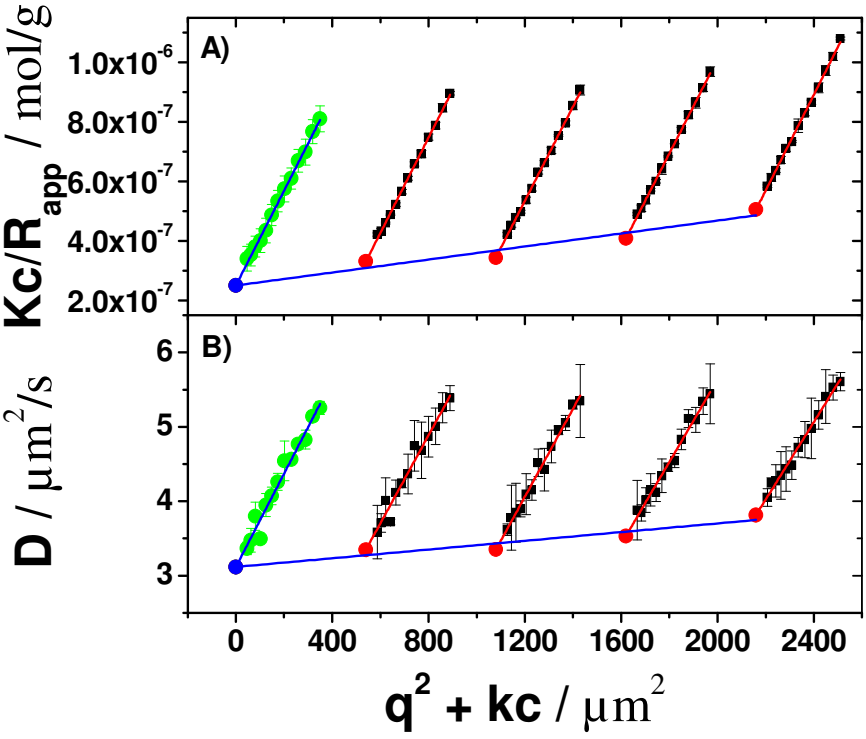

Figure 15: Zimm-plot of sample h-NaPSS-2 at 25°C and [I]=0.1. The results of the Zimm-plot are listed in table 14.

Another related method to use the Zimm plot for a characterization was used for sample NaPA-1. The sample preparation and the procedure for the measurement is the same, which was applied for the first method. After having done the measurement the scattering curves are analyzed also in that case with the help of the Zimm equation versus $q^2=0$. The different interceptions of the extrapolated scattering curves are plotted successively versus the sample concentration and extrapolated versus c=0 (Fig. 16 A). The slope of the fitted function correlates with $2*A_2$ and the intercept is the reciprocal M_w value. Additionally the slopes which were obtained by the Zimm extrapolations of the SLS curves are plotted versus the sample concentration and fitted by linear regression versus c=0 (Fig. 16 B). The intercept of that function represents $R_g^2/3M_w$ from which the non-apparent R_g value of the sample can be obtained with the help of the c=0 extrapolated M_w value.

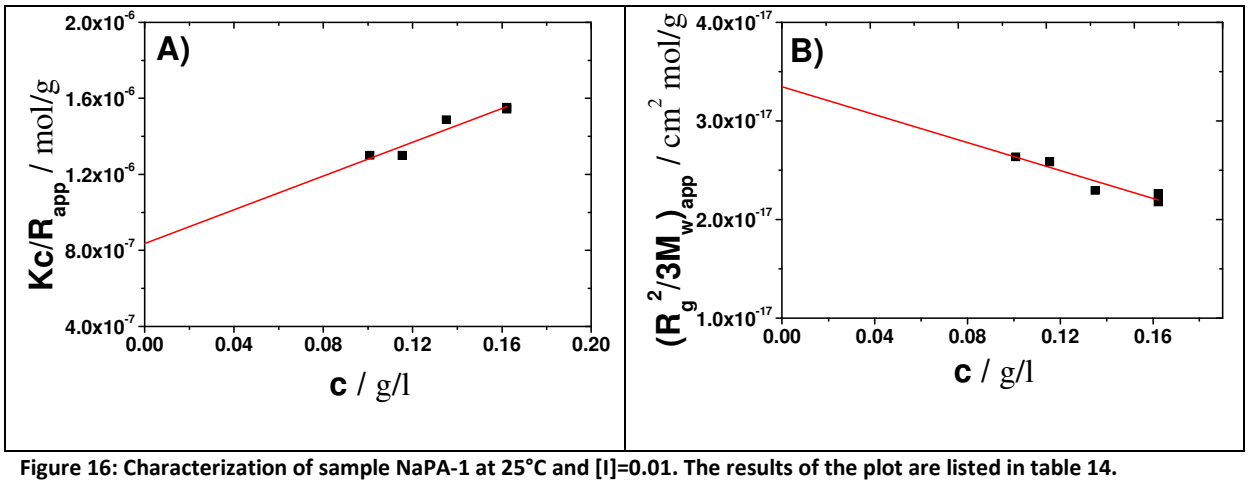

Figure 16: Characterization of sample NaPA-1 at 25°C and [I]=0.01. The results of the plot are listed in table 14.

The results of the different characterizations are presented in Table 14. They serve as reference data for all further experiments. The A_2 parameter has to be mentioned, because it gives an indication on the quality of the polymers.

All polymers exhibit a positive A_2-value, which is important for our experiments. If the A_2-value would be negative, it would be a hint that also in the absence of SICs aggregates exist. That would be problematic because these aggregates would distort the scattering experiments. An investigation of the single coil behavior in dependence of the SIC-concentration would be not possible anymore.

Additionally it can be observed that in the cases where a combined SLS/DLS analysis of the polymer was done, the structure sensitive parameter exhibits values of 1.6 to 1.75, which was expected for polyelectrolytes without SICs and which fits nicely to an polymer coil. Only sample NaPA-2 exhibits a ρ-value which is a little bit too low.

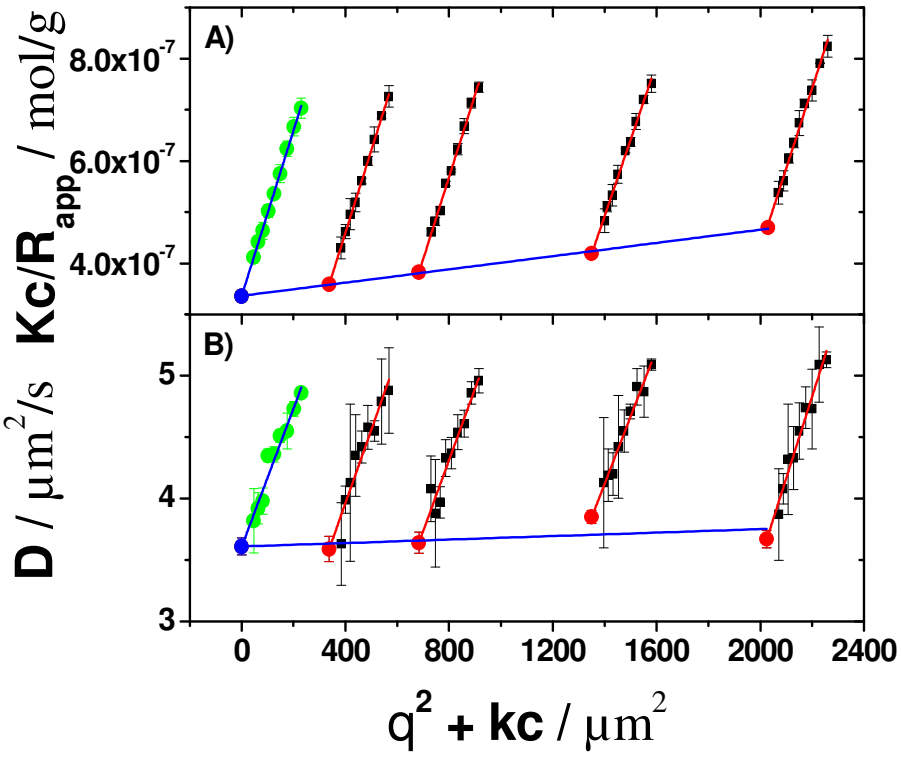

Figure 17: Zimm-plot of sample d-NaPSS at 25°C and [I]=0.1. The results of the Zimm-plot are listed in table 14.

Based on the molecular parameters of a polymer (Tab. 14) it is furthermore possible to estimate an overlap concentration according to $c^* = 3M_w/4\pi N_A R_g^3$. This value represents the state in the absence of specifically interacting cations. It also serves as a valuable guess for the state in the presence of specifically interacting cations, where the coils are expected to be smaller. It is important to run light scattering experiments below the critical overlap concentration in order to guarantee existence of the single coil behavior.

Table 14: Characterization of the polymer samples.

Sample	R_g / nm	R_h / nm	M_w / g/mol	ρ	A_2 / l*mol/g^2	k_D / l/g
h-NaPSS-1	74	43	1.609 x 10^6	1.72	3.347 x 10^{-7}	0.1987
h-NaPSS-2	138	79	4.001 x 10^6	1.74	3.275 x 10^{-7}	0.5632
d-NaPSS	120	68	2.974 x 10^6	1.76	1.947 x 10^{-7}	0.1176
NaPA-1	109	-	1.197 x 10^6	-	2.221 x 10^{-6}	-
NaPA-2	106*	77	1.132 x 10^6*	1.37	3.750 x 10^{-6}*	3.416

*Determined by Berry-Plot[85]

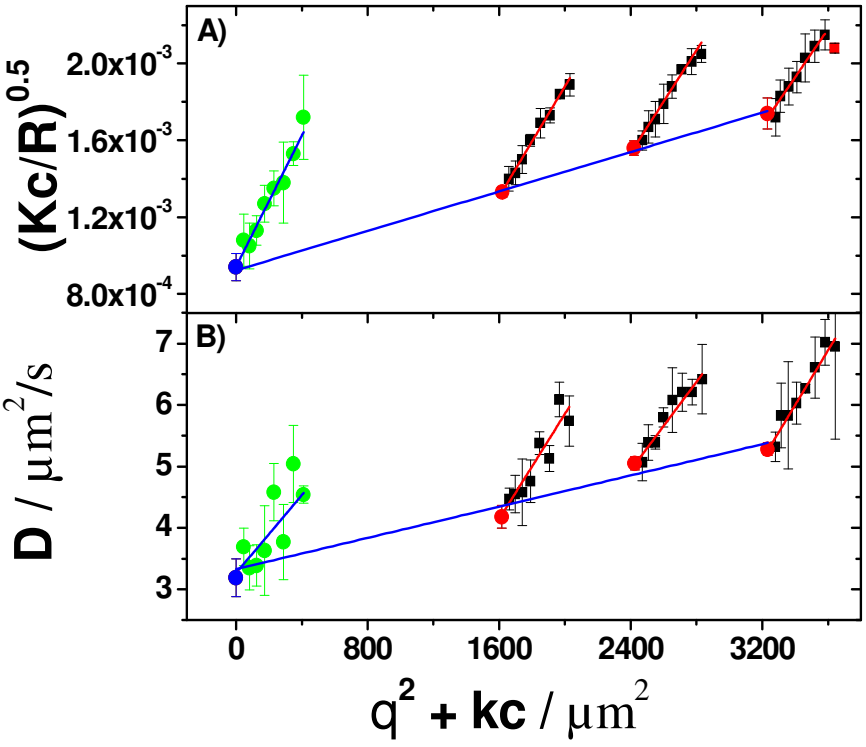

Figure 18: Berry-plot[85] of sample NaPA-2 at 25°C and [I]=0.01. The results of the Berry-plot are listed in table 14.

4.2 NaPSS in the Presence of Al^{3+}

4.2.1 Solution Behavior and Phase Diagram

The main features of the solution behavior of NaPSS in saline solutions in the presence of Al^{3+} cations were established with sample h-NaPSS-2.

The phase diagram of aqueous solutions of AlPSS at [I]=0.1 M can be subdivided into three different regimes. In the regime with low contents of Al^{3+} limited by eq 1, the solutions are clear and light scattering measurements show single coil behavior. In an intermediate regime the solutions become opaque directly after mixing. After several hours an oil like transparent deposit is formed on the bottom of the glass vials and the overlaying solutions become clear again. Light scattering with the overlaying solutions shows aggregates. The phase boundary, separating stable solutions from solutions where aggregation and precipitation takes place, exhibits a stoichiometric correlation between $[Al^{3+}]_{pb}$ and $[SO_3^-]_{pb}$

where $[Al^{3+}]_{pb}$ and $[SO_3^-]_{pb}$ are the molar concentrations of aluminum cations and of PSS in terms of monomers at the phase boundary defined by eq 1.

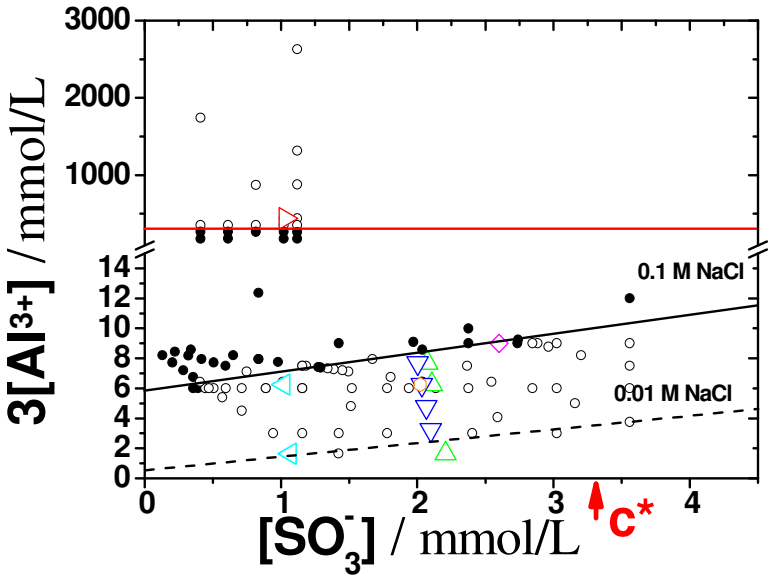

Figure 19: Phase diagram of sample h-NaPSS-2 at [I]=0.1 M in the presence of Al^{3+}. Open symbols denote stable samples, i.e. clear solutions. Full symbols indicate instable samples, i.e. turbid solutions. Colored open symbols indicate samples characterized by light scattering: series h-AlPSS-1 (△), series h-AlPSS-2 (▽), series h-AlPSS-3 (◁), sample above re-entrant phase boundary (▷), AlPSS-temp1 (□) and AlPSS-temp2 (◇). The lines have the following meaning (from top to bottom): line of re-entrant phase (red), phase boundary (black) and for comparison a phase boundary in 0.01 M NaCl (black, dashed).

The slope of the phase boundary of h-NaPSS-2 in the presence of Al^{3+} exhibits a value close to 1/3, which indicates that at the phase boundary every negative charge in the PSS chain is neutralized by a positive charge from the trivalent Al^{3+} cations (see Table 15 for i and m values). The correlation of eq 1 is in close analogy to the trends observed with polyacrylates in the presence of alkaline earth cations, Cu^{2+} and Pb^{2+}.[12–15]

Table 15: Values for i and m according to eq 1 for the phase boundaries obtained with polymer sample h-NaPSS-2 at different [I].

$[Na^+]+3[Al^{3+}]=[I]$	intercept i in mmol/L	slope m
h-NaPSS-2 at [I]=0.1 M (H_2O)	1.95	0.42
h-NaPSS-2 at [I]=0.01 M (H_2O)	0.18	0.30

At higher Al^{3+}-concentrations a second phase boundary occurs, which limits the regime of aggregation/precipitation. Above this boundary, the samples remain clear from the beginning and light scattering measurements reveal stable R_g, M_w and R_h values comparable to the values of the AlPSS coils close to but below the lower phase boundary (Fig. 20 and Tab. 16). We conclude that once the concentration of the Al^{3+}-cations gets high enough PSS coils undergo a charge reversal due to an increasing excess of Al^{3+}-cations decorating the

polyelectrolyte. The resulting electrostatic repulsion prevents coils from aggregating.[19,20,86,87] It has to be emphasized here that values of M_w closest to both boundaries are getting close to twice as large as the values of single coils. As detailed below, this may indicate occurrence of a small amount of equilibrated aggregates or may be caused by a variation of the scattering contrast.

An additional analysis at $[I]=3[Al^{3+}]+[Na^+]=0.01$ M provides information of the impact of an inert salt on the phase behavior. As it is demonstrated in Figure 1 the slope m=1/3 is the same as observed at [I]=0.1 M. Yet, the phase boundary observed at [I]=0.01 M is clearly below the corresponding line at [I]=0.1 M (Fig. 19 and values for i in Tab. 15). The reason for this effect is the exchange pressure exerted by the Na^+-cations on the Al^{3+} bound to the sulfonated groups of the polymer. When switching from [I]=0.1 M to [I]=0.01 M, the concentration of Na^+ cations and along with it their exchange pressure decreases. The same effect has been observed for CaPA and for CaPMA in aqueous NaCl.[12,18,88,89]

Since the values are stable at both boundaries and close to values observed for single coils the results establish the existence of an instable regime limited by a threshold according to eq 1 and a re-entrant phase. The same feature has also been observed with Th^{4+} and La^{3+} with PSS[19,20,90] and with La^{3+} and Y^{3+} and proteins.[86,87] This feature together with the reduction of the regime of instability with increasing [I] is in qualitative agreement with predictions by Olvera de la Cruz et al.[20] and Solis[34], who developed a model which takes into account attractions between negatively charged residues and positively charged complexes of an n-valent cation with less than n negatively charged residues.

Table 16: Light scattering results from samples located beyond the re-entrant phase boundary.

Location in Fig. 1	M_w / g/mol	R_g / nm	R_h / nm	ρ
Point in path 2 closest to the phase boundary defined by eq 1	7.18E+06	85.2	59.6	1.4
Sample above re-entrant phase boundary (freshly prepared)	8.64E+06	102.8	78.2	1.3
Sample above re-entrant phase boundary (2 days of aging)	7.52E+06	96.7	73.78	1.3

Noteworthy, Jia and Zhao[90] did not only observe a re-expansion of LaPSS coil dimensions upon re-entering the upper solution phase due to charge reversal but also a coil shrinking of PSS with a size minimum followed by re-expansion for Cs^+ and Ca^{2+} , which at least for Cs^+ cannot be interpreted with a charge reversal. However, PSS neither showed a re-entrant phase with Cs^+ nor with Ca^{2+}.

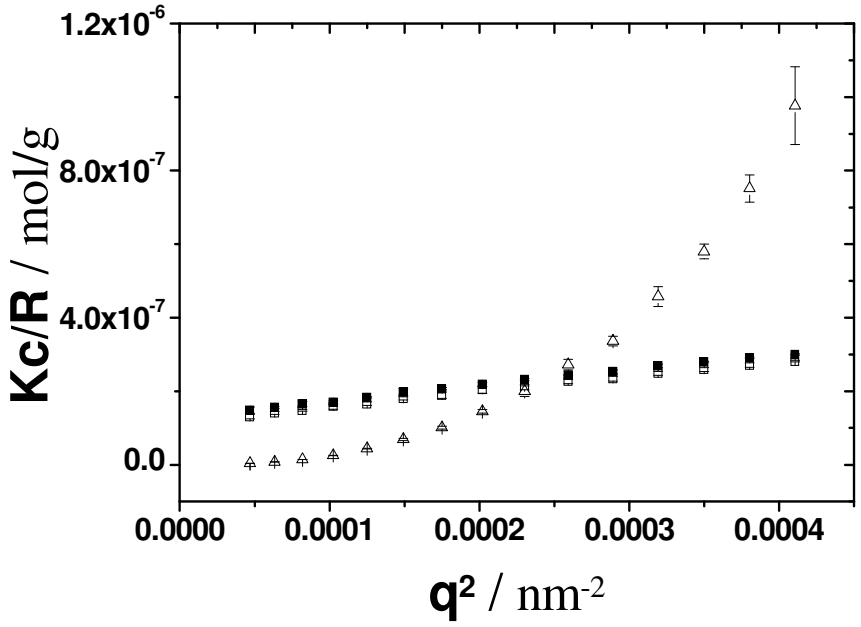

Figure 20: Scattering curves of two samples close to the re-entrant phase boundary: freshly prepared state below the re-entrant phase boundary (△), state located above the re-entrant phase boundary freshly prepared (□) and after an aging time of two days (■).

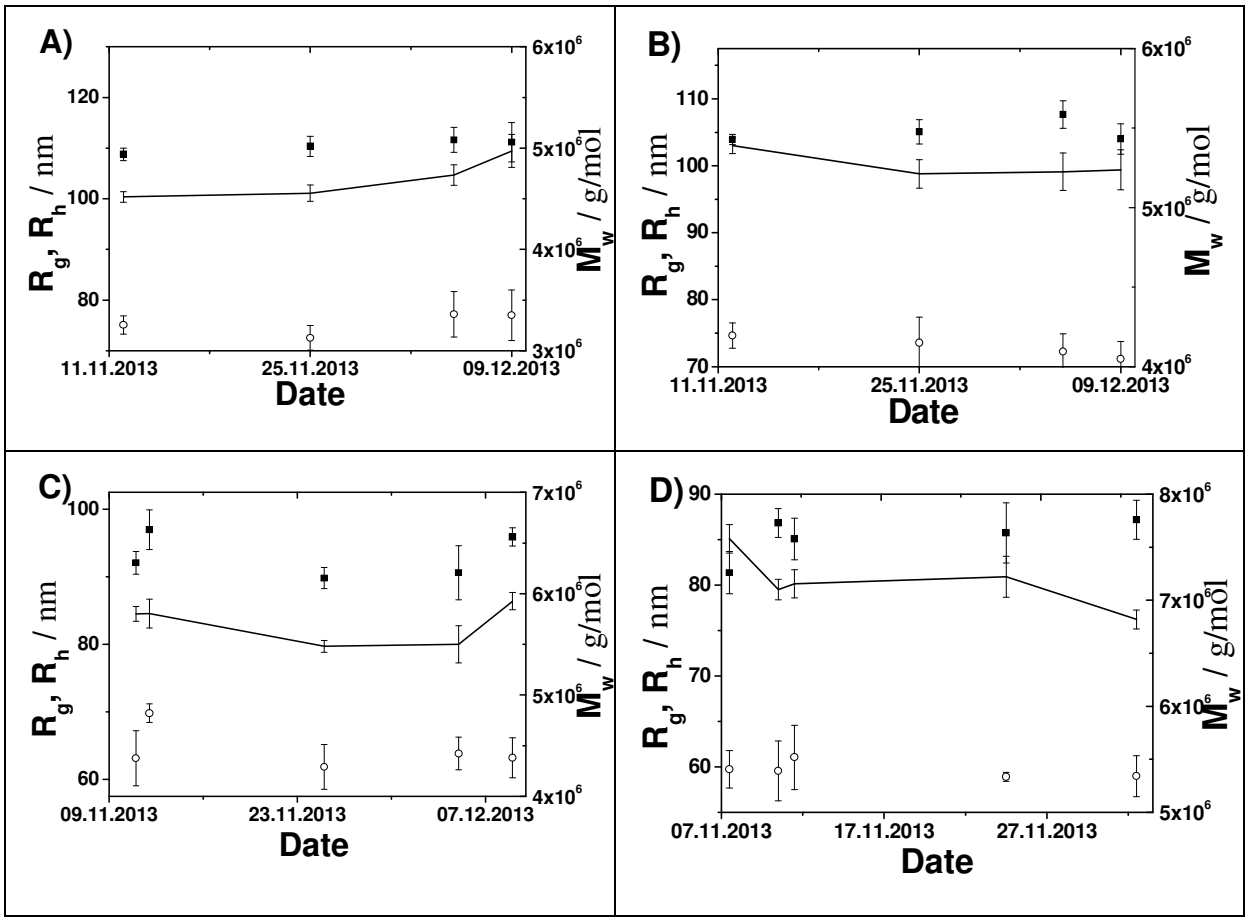

Figure 21: Results of repeating light scattering measurements of sample series h-AlPSS-2 in a periode of one month: A) 3-3-0.2, B) 3-3-0.3, C) 3-3-0.4 and D) 3-3-0.5. R_g (■), R_h (○) and M_w (solid line).

Further experiments have been performed to reveal the shrinking of the PSS coils as a function of the Al^{3+} concentration in the regime of stable coils limited by the phase boundary

which obeys eq 1. To this end solutions of h-NaPSS-2 close to the phase boundary separating single coils (low Al^{3+} content) from the regime where aggregates/precipitates occur (higher Al^{3+} content) have been analyzed by combined SLS/DLS. Samples from different dilution series, established with polymer sample h-NaPSS-2 were measured repeatedly over a longer period of time to scrutinize the stability of the samples for the AlPSS system. The scattering curves were analyzed by the Zimm approximation.[49] If a sample is stable the results from repeated measurements (Fig. 21) of this sample are averaged and plotted versus the ratio $[Al^{3+}]/[SO_3^-]$ ratio (Fig. 22).

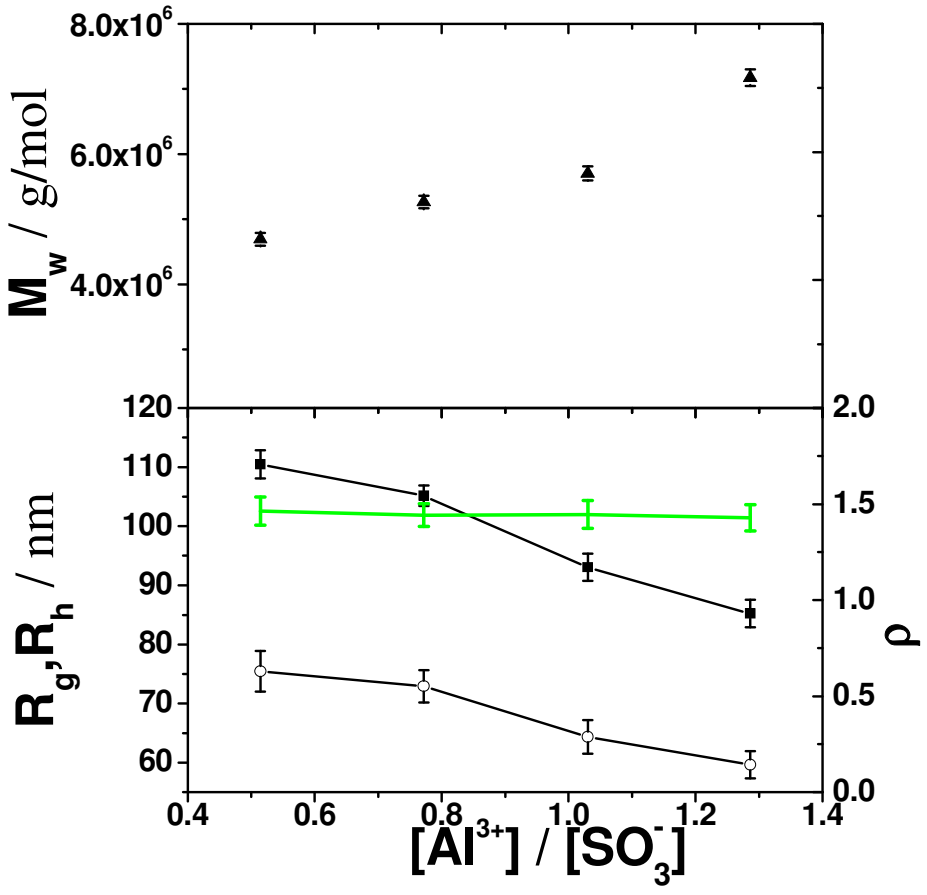

Figure 22: R_g (■), R_h (○), M_w (▲) and ρ (green line) of h-NaPSS-2 at [I]=0.1 M as a function of the ratio of $[Al^{3+}]/[SO_3^-]$.

The values for series h-AlPSS-2 are outlined in Figure 22 as an example. The experiments for h-AlPSS-1 and h-AlPSS-3 show comparable results and are presented in Chapter A1 of the appendix. The radius of gyration (R_g) of the PSS coils decreases from 110 nm to 85 nm with increasing amount of Al^{3+}-cations. The same trend can be observed for the hydrodynamic radius (R_h), which decreases from 75 nm to 60 nm. This shrinking of coils induced by Al^{3+} goes beyond mere electrostatic screening from the corresponding charges of the added salt(s) as we apply a constant overall concentration of cationic charges (by ion replacement technique) usually at an excess of Na^+ ions. Two causes are possible for this extraordinary shrinking, bridging between oppositely charged segments and charge neutralization of segments. Bridging is more likely to occur with trivalent cations than with bivalent cations

because the chance for a survival of positive net charges after complexation is higher in case of trivalent cations than in case of bivalent cations. A complex between Al^{3+} and two neighboring negative residues still results in a positive net charge of the corresponding segment. The charge neutralization renders coils more hydrophobic with increasing metal cation concentration making the decorated coils increasingly less soluble.

In this latter case attraction among segments are induced by their highly positive Flory-Huggins parameter. Although both features are capable in principle of inducing a coil shrinking and of generating phase boundaries obeying eq 1, nothing can be said about the relative impact of the two influences. Noteworthy, phase boundaries according to eq 1 can be reconciled equally well with models based on either bridging[19,37] or charge neutralization[89]. However, according to earlier findings, bridging may play a significant role only once the valency of the cations is larger than two and increase of the Flory-Huggins interaction parameters due to chain neutralization dominates shrinking and aggregation in case of combinations of bivalent cations like alkaline earth cations with polyacrylates. Horkay et al.[91] succeeded to separate the contribution of mixing, chain elasticity and distribution of ions to the free energy of a polyacrylate gel in the presence of a series of alkaline cations and alkaline earth cations and could show that though the alkaline earth cations show a collapse of the gels at a certain cation concentration, they do not modify the effective crosslinking density thus excluding significant bridging and confirming that charge neutralization is the dominating cause for the extraordinary shrinking in case of at least the bivalent alkaline earth cations interacting specifically with polyacrylates.

The corresponding apparent molecular weight along dilution path of series h-AlPSS-2 increases from the point with the lowest concentration of Al^{3+} to the point with the highest concentration of Al^{3+} from 4500 to 7000 kDa. This increase seems to contradict states, where just single coils exist. However, the increase of the apparent molecular weight may be partly caused by a decoration of the coils with Al^{3+}-cations which gradually changes NaPSS to AlPSS and which leads to a change in the dn/dc value, entering the contrast factor K in eq 10 as squared value. Nevertheless formation of a small amount of aggregates cannot be entirely excluded. In such a case, coexistence of a small fraction of oligomeric aggregates aside from dominating single chains would suffice to explain the increase of the weight averaged molar mass by a factor of 1.5 – 2.0. If such a small extent of aggregation would occur its impact on the size would have been outweighed by a coil contraction since the values for R_g and R_h decrease with respect to the size of the PSS coils without specifically interacting cations.

If a small fraction of aggregates would be responsible for the slight increase in the apparent M_w in Fig. 22, formation of such a small fraction of chain oligomers may occur during mixing the two component solutions by hand whereby the SIC solution is gently dropped into the polyelectrolyte solution. Strong concentration fluctuations close to the dissolving drops may generate non-equilibrium morphologies like aggregates. In order to avoid such undesirable states, one series with sample d-NaPSS at [I]=0.1 M was established by mixing the NaPSS stock solution and the $AlCl_3$ solution with a dialysis cell. After dialysis the samples were

measured by combined light scattering and compared with results established by the usual mixing method. The light scattering results show full agreement between both sample series with respect to R_g, R_h, ρ and M_w (Fig. 23). Hence, mixing of the SIC solution with the PSS solution by hand can be ruled out as a cause of aggregates in solution. The result of the dialysis experiment in fact is even in favor of a change in the scattering contrast as the main reason for the slight increase in the apparent M_w.

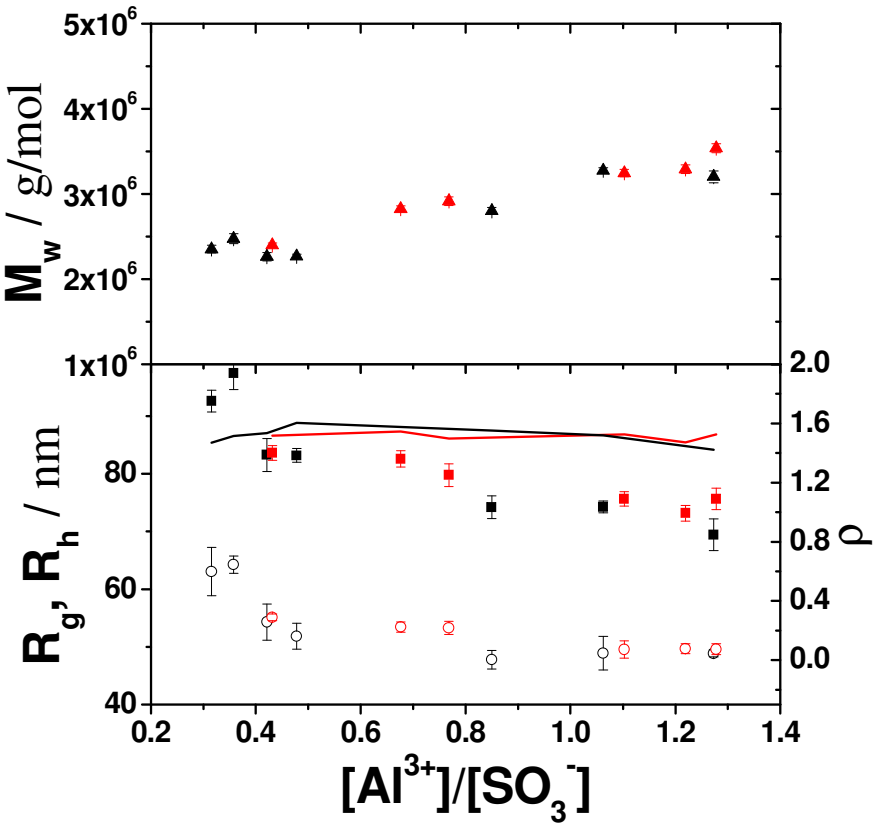

Figure 23: Variation of R_g (■), R_h (○), M_w (▲) and ρ (line) with ratio of $[Al^{3+}]/[SO_3^-]$ of d-NaPSS at [I]=0.1 M. Black symbols and lines represent values of solutions prepared by hand mixing (identical to data in Figure 28). Red symbols and lines represent values obtained from an experimental series where the d-NaPSS solutions and the $AlCl_3$ solutions were mixed with the help of a dialysis cell.

For polyacrylates in the presence of alkaline earth cations it is known that the polyacrylates shrink from expanded coils to compact spheres.[12,13] The AlPSS coils also shrink by 40 % but the ρ ratio keeps constant at 1.4 throughout the entire range of shrinking thereby excluding significant changes of the shape. One reason may be that the aggregation process of AlPSS may start, before the chains are fully collapsed, thus preventing the shrinking coils from adapting a fully collapsed structure.

4.2.2 Temperature Dependent Coil Collapse

The effect of temperature on the solution behavior of AlPSS was investigated by light scattering with two compositions. First, the sample denoted as AlPSS-temp1 was selected which lies further apart from the threshold in the phase diagram. The temperature was

changed from 298 K to 318 K. After each heating step, the sample was thermally equilibrated for half an hour before being measured. The radius of gyration decreased with increasing temperature from 95 nm to 70 nm (Figure 24). At the same time the hydrodynamic radius decreased from 68 nm to 55 nm. The trends in size can be reconciled with a variation in the extent of decoration with specifically interacting cations. Since the structure sensitive parameter stays constant close to a value of ρ = 1.3 -1.4, we conclude that the shrinking polymers keep their coil-like structure. It is noteworthy, that the temperature induced decrease of coil dimensions was accompanied by a small reversible increase of the apparent M_w value and vice versa (Fig. 24). As this is in full analogy to the trend observed during a variation of $[Al^{3+}]/[SO_3^-]$ (Fig. 22) the trend can again be attributed to variation of the scattering contrast of NaPSS inferred by the decoration with Al^{3+}-cations and/or the occurrence of a small fractions of chain oligomers.

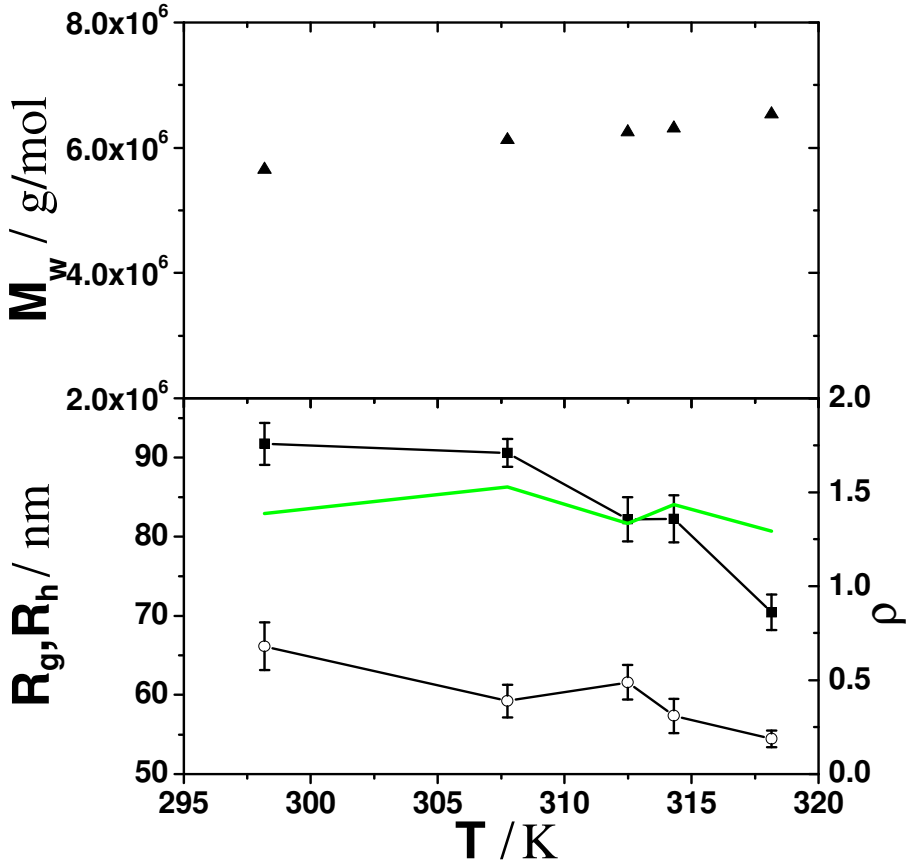

Figure 24: Temperature dependence of R_g (■), R_h (○), M_w (▲) and ρ (green line) of the PSS in the presence of Al^{3+} at the composition of 2.02 mM h-NaPSS-2 and 2.08 mM $AlCl_3$ at [I]=0.1 M. The sample is denoted as AlPSS-temp1 in Fig. 19.

The sample denoted as AlPSS-temp2 was opaque already at 25°C and showed aggregates in the light scattering measurement. Therefore the temperature was decreased to 20°C. The solution became clear and the radius of gyration adopted a value of 69 nm. Successively, the sample was heated by small temperature increments from 20°C to 25°C. After each increase of the temperature, the sample was thermally equilibrated in the goniometer for half an hour. The data were analyzed with the Guinier approximation[50]. At 22°C the sample was still

clear, but the radius of gyration increased to 259 nm, which indicates that the aggregation process has started (Figure 25). Between 22°C and 23°C the solution became opaque. After an equilibration to 25°C, the solution was cooled again. Turbidity disappeared and the solution showed again single chain behavior, thus proving complete reversibility of the aggregation process close to the threshold.

The experiments also nicely confirm that the apparent M_w ~$5*10^7$ g/mol at 20°C corresponds to an equilibrium state independent on whether that state is given by single coils with a slightly modified scattering contrast or by mixture of single coils and a small fraction of oligomers.

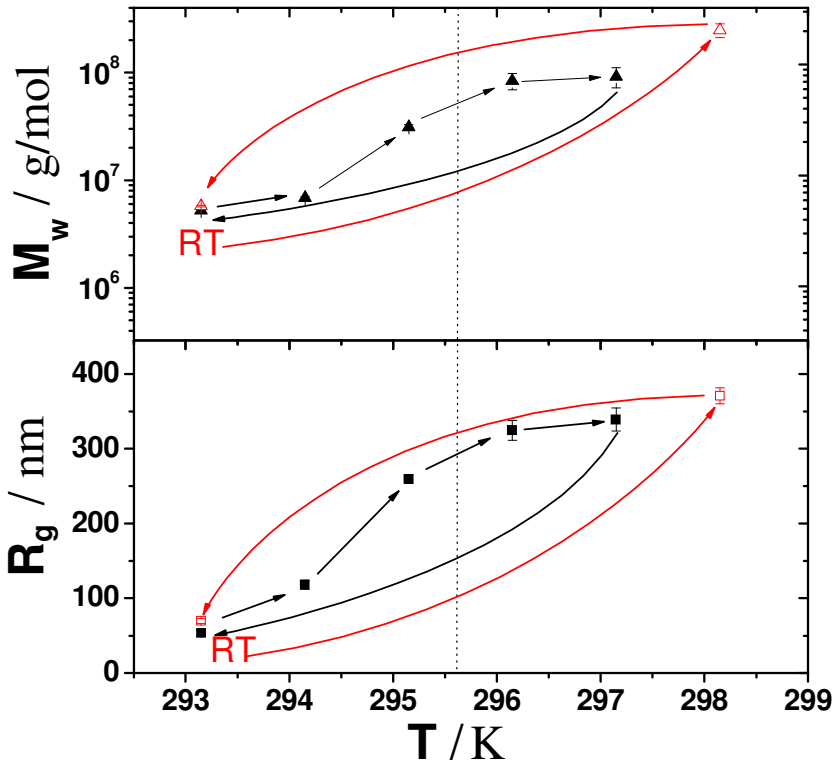

Figure 25: Temperature dependence of R_g and M_w value for PSS in the presence of Al^{3+} at the composition of 2.6 mM h-NaPSS-2 and 3 mM $AlCl_3$ at [I]=0.1 M. The sample is denoted as AlPSS-temp2 in Fig. 19. Red symbols denote heating/cooling process 1 and black symbols represent values for the heating/cooling process 2.

Lages et al.[30] have investigated this effect for CaPA complexes. By increasing the temperature from 15°C to 35°C, the radius of gyration of the PA coils decreased from 70 to 23 nm in qualitative agreement with the present observations on PSS in the presence of Al^{3+}. Since an entropic driving force could be verified for the binding of Ca^{2+} to anionic PA chains[29], we conclude that a similar driving force governs the binding of Al^{3+} to the anionic residues of PSS. However, this pattern is not as general as it might appear. Prabhu et al.[36,37] revealed a shift of the phase boundary to lower concentrations of Ba^{2+} cations with

decreasing temperature for aqueous solutions of BaPSS. Strikingly, this is inverse to the trend expected for the same cation in the in combination with NaPA.

4.2.3 SANS/SAXS Experiments

By means of a combination of light scattering and small angle neutron and x-ray scattering Schweins et al.[25] could show that anionic polyacrylate chains in the presence of alkaline earth cations undergo a continuous transformation from extended coils to highly compact spheres, whereby pearl necklace like states are adopted by intermediates close to the phase boundary. Although the shape sensitive parameters remain constant in case of AlPSS, this cannot fully exclude pearl necklace like intermediates also in the present study. In order to shed further light on the structure of intermediates along paths approaching the phase boundary of AlPSS small angle neutron and x-ray scattering experiment were carried out.

4.2.3.1 SANS Experiments with Deuterated NaPSS

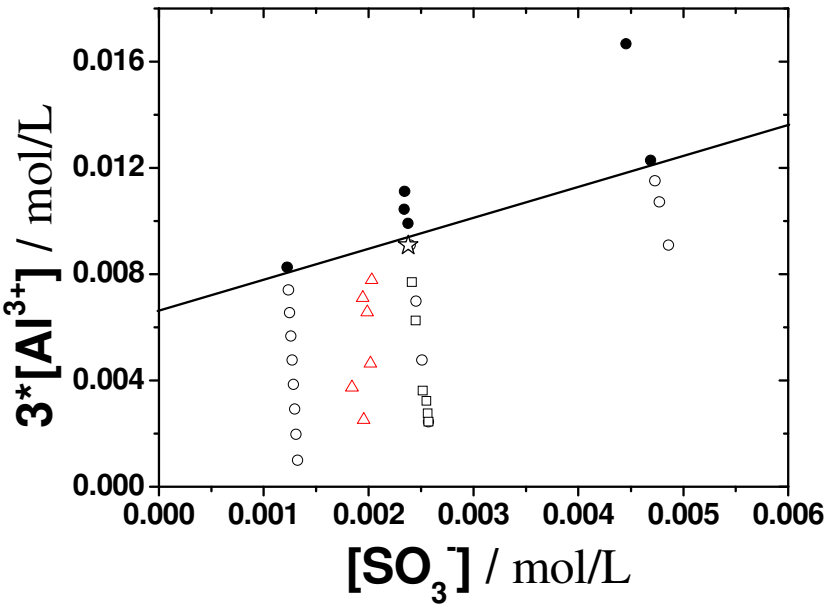

Figure 26: Phase diagram of sample d-NaPSS at [I]=0.1 M in the presence of Al^{3+}. Open symbols denote stable samples, i.e. clear solutions. Full symbols indicate instable samples, i.e. turbid solutions. Open squares (□) indicate samples which were characterized only by light scattering. Sample M-S-I which was analyzed by light scattering and SANS is denoted by an open red star (☆). Triangles (△) represent the experimental series where the d-NaPSS solutions and the $AlCl_3$ solutions were mixed with the help of a dialysis cell.

Prior to the SANS experiment a phase diagram has been established for the deuterated NaPSS in 0.1 M aqueous NaCl in the presence of Al^{3+}-cations (Fig. 26). As expected, a similar phase diagram could be revealed for d-NaPSS as shown in Fig. 19 for h-NaPSS-2. The threshold obeys a trend of eq 1 with i=2.21 and m=0.39 in close agreement with the values for h-NaPSS-2. Light scattering experiments showed again a shrinking of the polymer coils with increasing [Al^{3+}] (Fig. 27).

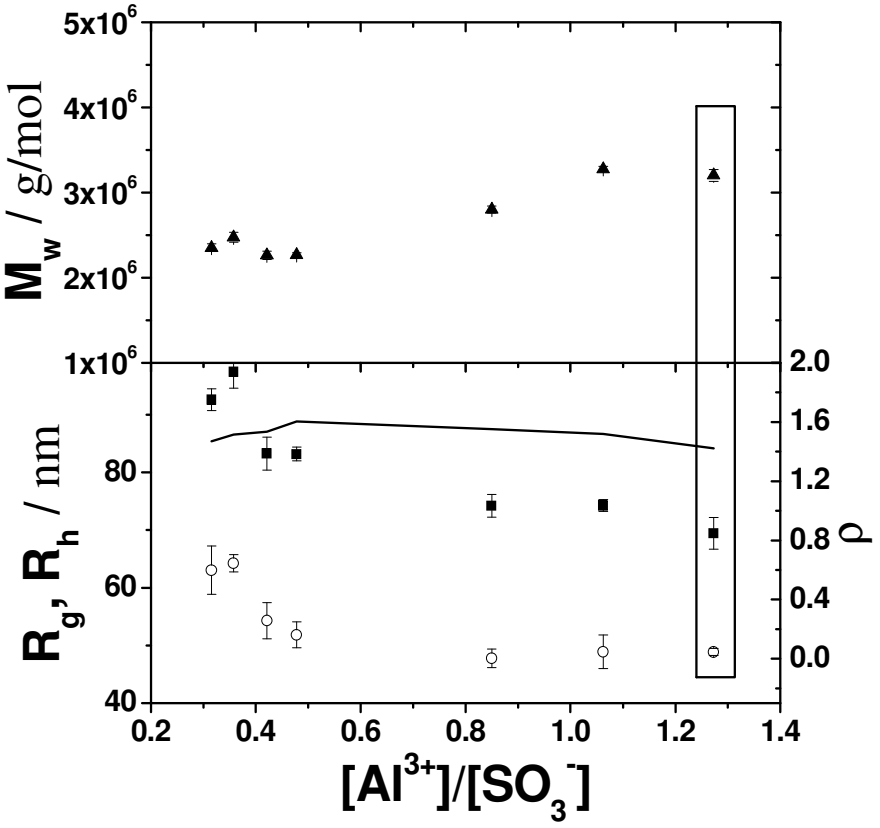

Figure 27: Variation of R_g (■), R_h (○), M_w (▲) and ρ (line) with ratio of $[Al^{3+}]/[SO_3^-]$ of d-NaPSS at [I]=0.1 M. The symbols in the open box column indicate the values for R_g, R_h, M_w and ρ which were obtained by combined SLS/DLS for sample M-S-I.

For the SANS experiment with d-NaPSS in H_2O sample M-S-I located close to the phase boundary in the stable part of the phase diagram has been selected. The light scattering experiment of M-S-I analyzed by the Zimm approximation[49] shows a R_g of 69.4 nm and a R_h of 48.9 nm (Fig. 27). The SANS curve in Fig. 28 was overlayed with the corresponding light scattering data by multiplying the values of the light scattering curve with a constant value. The resulting curve in the log-log plot of Fig. 28 exhibits a slope close to -2 which is typical for an unperturbed coil conformation of the chains. Indeed, the composite curve is in good agreement with the form factor of a polydisperse Gaussian chain according to eq 45 (Fig. 28).[68,75] This result further confirms that the shrinking of the AlPSS coils is not accompanied by a significant change of the shape.

Table 17: Fit parameters of the model of a Gaussian chain to the joint SANS/SLS curve and R_g obtained from SLS.

sample	R_g(fit) / nm	U	χ^2/Npts	R_g(exp.) / nm (SLS)	P (SLS/DLS)
M-S-I	64.85	0.0797	5.8399	69.4	1.42

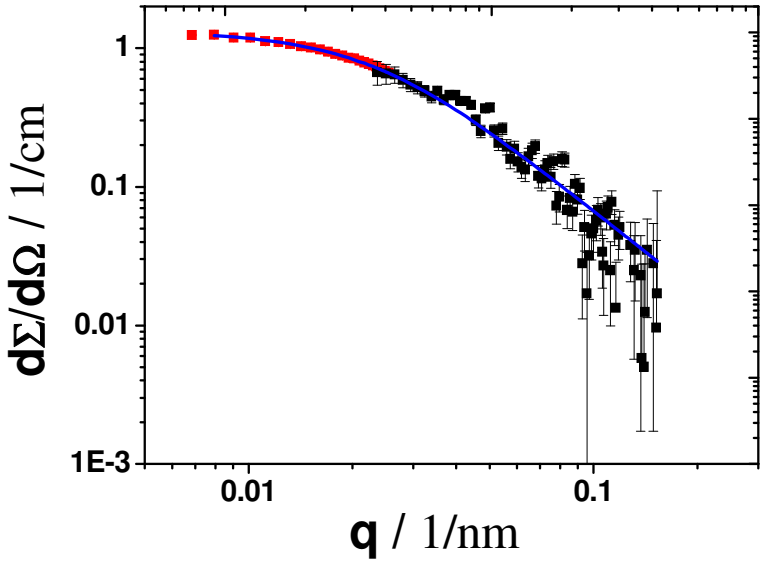

Figure 28: Joint SLS(■) and SANS(■) scattering curve of deuterated d-NaPSS in H_2O at [I]=0.1 M. The blue line overlaying the data of M-S-I indicates a fit with the model of a polydisperse Gaussian chain.[68,75]

4.2.3.2 SANS/SAXS Experiments with Hydrogenated NaPSS

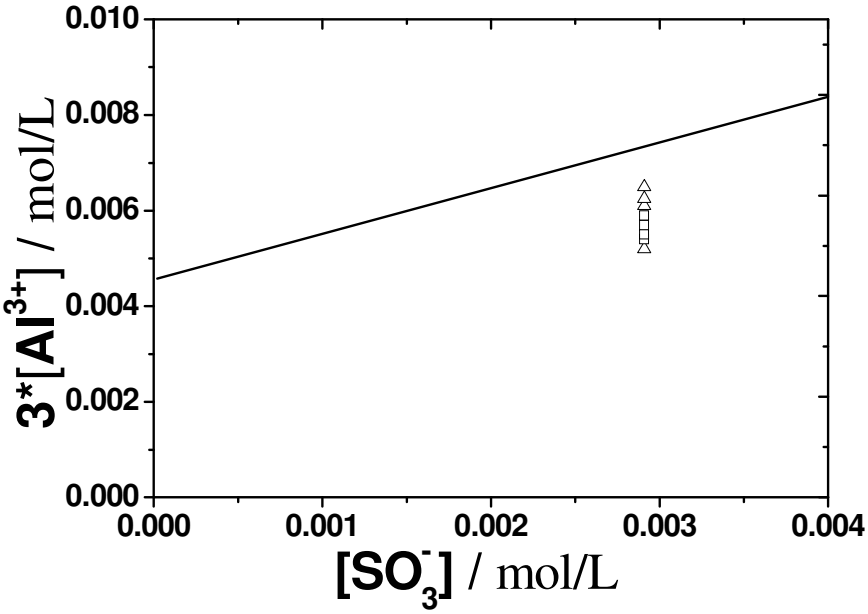

Figure 29: Phase diagram of sample h-NaPSS-2 in D_2O at [I]=0.1 M in the presence of Al^{3+}. Open symbols indicate samples which were characterized by light scattering. Samples which were analyzed by light scattering and SANS are denoted by open triangles (△).

A proper phase diagram had to be established also for the study of hydrogenated NaPSS in 0.1 M aqueous NaCl based on D_2O (Fig. 29). In agreement with the phase boundary of h-NaPSS-2 in H_2O and d-NaPSS in H_2O a stoichiometric correlation between $[Al^{3+}]$ and $[SO_3^-]$ could be verified with a slope m close to 1/3 (Tab. 18) for the sample h-NaPSS-1 in D_2O at [I]=0.1 M.

Table 18: Values for i and m according to eq 1 for the phase boundaries obtained with different PSS samples and solvents.

	intercept i in mmol/L	slope m
h-NaPSS-2 in 0.1 Mol NaCl (H_2O)	1.95	0.42
h-NaPSS-2 in 0.01 Mol NaCl (H_2O)	0.18	0.30
d-NaPSS in 0.1 Mol NaCl (H_2O)	2.21	0.39
h-NaPSS-1 in 0.1 Mol NaCl (D_2O)	1.59	0.32

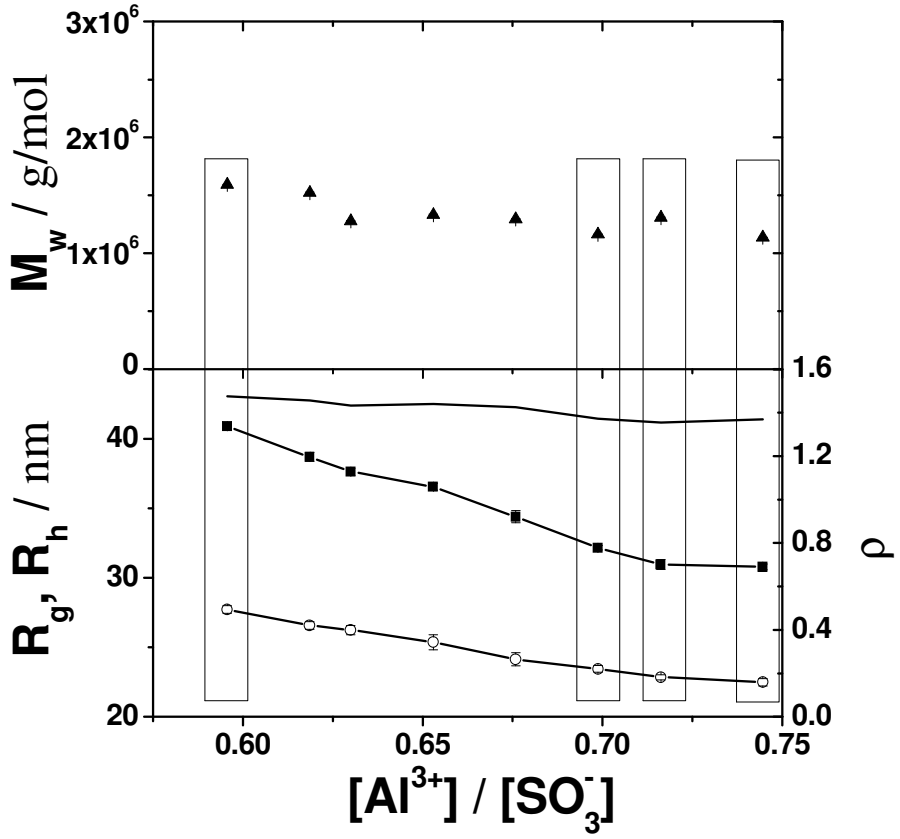

Figure 30: Variation of R_g (■), R_h (○), M_w (▲) and ρ (line) with ratio of $[Al^{3+}]/[SO_3^-]$ of h-NaPSS-1 in D_2O at [I]=0.1 M. The values in open boxes indicate values for R_g, R_h, M_w and ρ obtained for the samples AlPSS-S-1, AlPSS-S-6, AlPSS-S-7 and AlPSS-S-8 (from left to right) which were analyzed by SANS. The values of those four samples correspond to time averages recorded during the respective SANS experiments.

The SANS/SAXS study is based on a series with variable $[Al^{3+}]$ at a PSS concentration fixed at $[SO_3^-]$=0.00291 mol/L located in the stable regime of the phase diagram. Light scattering experiments along this series show a decrease of R_g from 42 nm to 31 nm with increasing $[Al^{3+}]$ (Fig. 30). The R_h decreases also from 27 nm to 22 nm. The value for the structure

sensitive parameter decreases slightly from 1.47 to 1.36 which is again an indication, that the structure of the PSS-chains is still far from adopting a compact sphere.

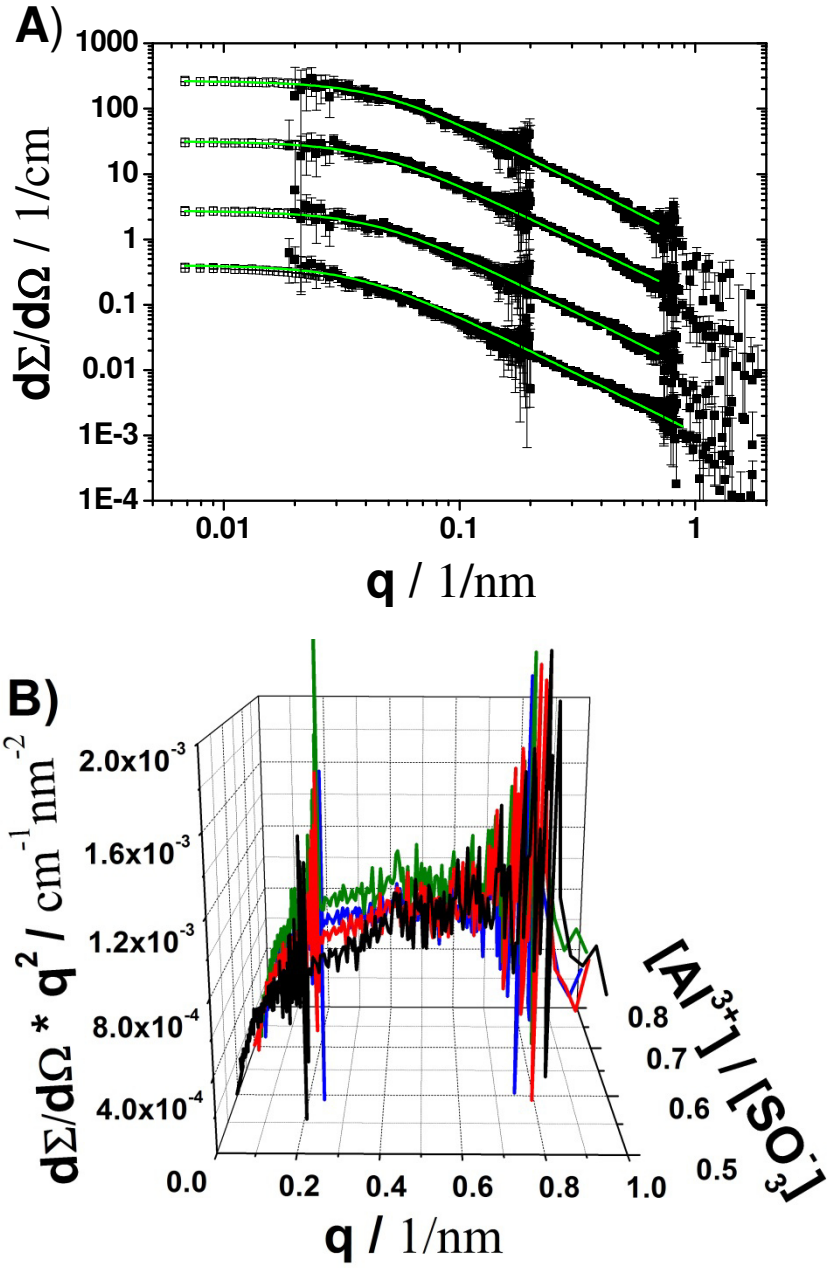

Figure 31: A) Combined SLS(□) and SANS(■) scattering curves (from bottom to top) of sample AlPSS-S-1 (lower curve), AlPSS-S-6 (shifted by factor of 10 to higher scattering intensities), AlPSS-S-7 (shifted by afactor of 100 to higher scattering intensities) and AlPSS-S-8 (shifted by a factor of 1000 to higher scattering intensities) in comparison to the corresponding polymer excluded volume fit (green lines).[73,74] The respective fitting parameters are shown in Tab. 4 of the manuscript. The joint curves are adjusted to the respective SANS experiment. B) Kratky plots of the combined SLS and SANS curves of the samples from series AlPSS-S represented as a function of the ratio Al^{3+}/SO_3^- in a 3D-plot.

Four of these eight samples denoted as AlPSS-S-1, AlPSS-S-6, AlPSS-S-7 and AlPSS-S-8 were selected for an investigation with SANS. These four samples comprise the solutions with the lowest $[Al^{3+}]$ and the three highest values of $[Al^{3+}]$. The scattering curves obtained from SANS were overlaid with the respective curves from light scattering, by multiplying the light scattering curves with an appropriate shift factor. The log-log plot of the resulting form

factor for all four curves shows slopes close to -1.8, which is again an indication that even the most shrunken PSS-coils of the series exhibits a structure close to that of a coil. No structural change can be observed with increasing [Al^{3+}] (Fig. 31 A). The model of chains with excluded volume is expected to agree better with experiment than unperturbed chains since the experimentally found Porod exponent is closer to 5/3 than to 2. Hence, all curves were fitted with the model of a polymer chain with excluded volume based on the theory of Benoit and Hammouda.[73,74] Good agreement is achieved with the experimental SLS/SANS curves and the model curves (Table 19 and Fig. 31 A). R_g obtained from the fit with the excluded volume chain satisfactorily agree with the R_g derived from Zimm fits to the respective SLS curves.

A 3D Kratky plot, which contains all four scattering curves, illustrates that PSS coils undergo no structural change with increasing Al^{3+}-content (Fig. 31 B). In the Kratky plot the scattering intensity I(q) is multiplied with q^2. Therefore the scattering curves of sample series AlPSS-S, which show a power law with an exponent of -2 turn into a plateau.

Table 19: Fit parameters for SANS/SLS form factor and R_g obtained from SLS.

sample	R_g(fit) / nm	Porod-Exponent	χ^2/Npts	R_g(exp.) / nm (SLS)
AlPSS-S-1	37	1.79	2.43	41.8
AlPSS-S-6	31.8	1.81	885.78	32.4
AlPSS-S-7	31.9	1.76	2.72	30.9
AlPSS-S-8	30.6	1.83	9.04	30.9

Two of the four samples (AlPSS-S-1 and AlPSS-S-8) were analyzed additionally by SAXS in order to get further information on the impact of the Al^{3+} distribution on the scattering curves and to offer support on whether the compact domains are also locations with accumulated Al^{3+} cations Overlay of the either SAXS curve with the respective SLS/SANS curve by multiplying it with the proper shift factor in Figure 32, indicates a perfect match of the SAXS curve with the SLS/SANS curve in both cases . Although this may serve as a hint for an alignment of the Al^{3+} density with the SO_3^- density, a reliable proof for a match of the two densities could only be provided with a highly elaborate ASAXS experiment in case of metal cations[92] or SANS in case of organic cations[93]. ASAXS on dilute solutions of anionic polyacrylate brushes decorated with Rb^+ ions have indeed revealed a perfect match of the density distributions of Rb^+ and COO^- not otherwise observed for linear polyelectrolytes[92]. A similar match also with linear chains has only been observed by an ASAXS experiment where linear polyacrylates were exposed to alkaline earth salts acting as SIC[13].

It can thus be concluded that the structure of the shrinking h-PSS chains remain coil-like even close to the phase boundary. An intermediate pearl necklace like state, which was

found for the CaPA, SrPA and PbPA[15,25,27], could not be identified in case of the AlPSS in water even at states very close to the phase boundary. A similar observation, although in semidilute solutions of NaPSS in the presence of Ba^{2+} has been made by Prabhu et al.[36,37] with SANS. They also revealed a shrinking of the chain dimensions with increasing concentration of Ba^{2+} and the coils remained in a coil-like structure without any indication for the occurrence of entirely collapsed subdomains.

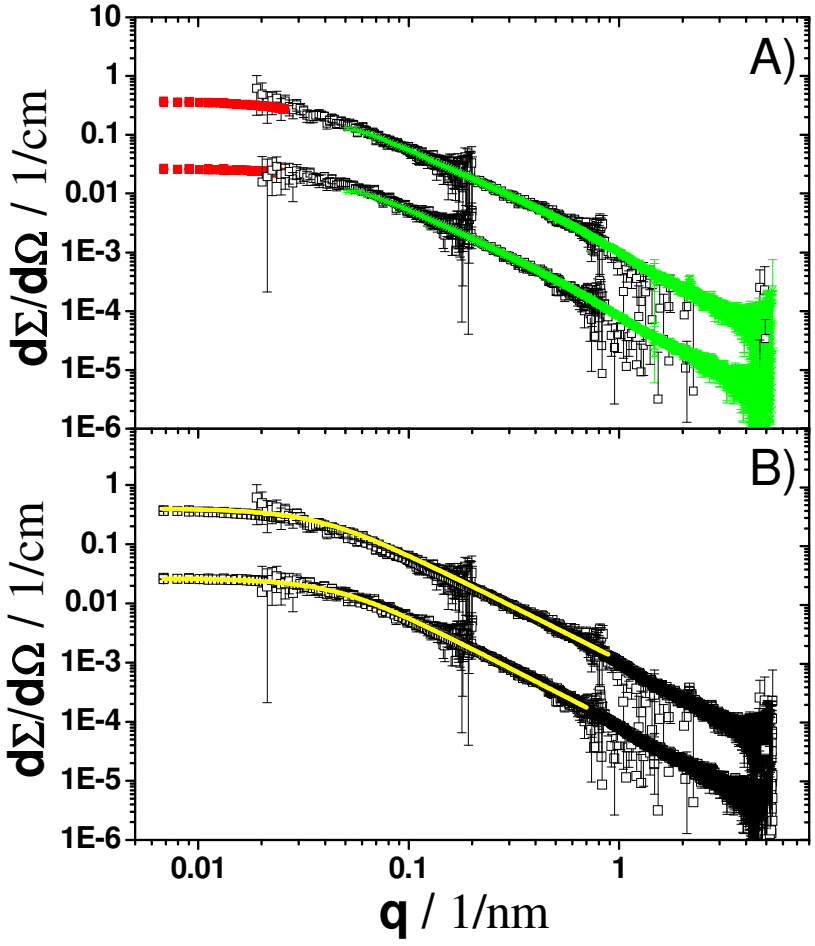

Figure 32: Combined SLS(■), SANS(□) and SAXS(X) scattering curves of sample AlIn (upper curve) and AlVIIIn (lower curve). B: Combined SLS/SANS/SAXS curves (□) of the same data as shown in A in comparison to the corresponding polymer excluded volume fit (yellow curves).[73,74] The joint data are adjusted to the respective SANS experiment. In both graphs the values of the combined AlVIIIn scattering data were shifted by a factor of 0.1.

Two features may affect the shrinking process and prevent chains from totally collapsing, chain stiffness and bridging. The persistence length of PSS[7,94,95] chains is estimated to 0.69 – 1.2nm, which is close to but lower than the persistence length of PA (~2.5 nm) ruling out chain stiffness as a cause of the lack of a full collapse of AlPSS coils. The tendency to form intra- and intermolecular bridges is expected to be higher in case of the trivalent Al^{3+}-cations in combination with polystyrenesulfonate than for the alkaline earth polyacrylates, because

binding of even two neighbouring negative residues to one trivalent cation leaves us with a positively charged entity, ready to "crosslink" with another negative residue of the chain. Taken together, both features may cause a start of the aggregation process before a collapse of the coils is completed.

4.2.4 Summary

Compared to those SIC-PA combinations and to SIC-PSS combinations, which have been investigated extensively in the past, striking similarities and differences could be revealed to combination of Al^{3+} and PSS. The phase boundary of AlPSS follows an L-type threshold, which was also observed for NaPA in the presence of alkaline earth cations, Cu^{2+} and Pb^{2+}.[12–15,17,18,88] An increase of the inert salt content from [I]=0.01 M to [I]=0.1 M, increases the exchange pressure on Al^{3+} cations bound to the ionic residuals of the PSS chains, which results in a shift of the threshold towards higher Al^{3+}-concentrations. This effect has also been reported for CaPA and CaPMA.[12,18,88,89]

In further analogy to the respective pattern of alkaline earth salts of NaPA significant shrinking of the PSS coils could be observed in the presence of Al^{3+} by approaching the L-type threshold. Only the extent of shrinking observed with the latter type of complex turned out to be weaker.

In agreement with predictions by Olvera de la Cruz et al.[20] and Solis[34] the complex of PSS with Al^{3+} cations exhibit a two phase regime which is limited by a re-entrant phase signified by a horizontal line and by an L-type precipitation line. Accordingly, AlPSS behaves like LaPSS and ThPSS[19,20], as two other combinations of polystyrene sulfonate with cations of a valence larger than 2. It is this large valence which particularly favors two features, charge reversal at high degrees of decoration and coexistence of units with opposite charges in a chain. A valence of three or more seems to be a prerequisite for the appearance of a re-entrant phase since no such re-entrant phase has been observed with bivalent cations. The interactions among the oppositely charged residues are also readily explaining the resulting L-type behavior.[20,34] Above all bridging can be easier reconciled with a premature aggregation at the threshold preventing the coils from totally collapsing, than a charge neutralization would do it.

In case of CaPA, SrPA and PbPA small angle scattering experiments revealed pearl necklace like intermediate states while approaching the state of compact spheres at the threshold and a collapse towards compact spheres could be identified via combined light scattering. With the help of SANS and joint SANS and SAXS experiments it could be shown that the chains of the AlPSS chains do not change their form factor while their states approach the L-type threshold causing a shrinking. Their shape remains coil-like even at states, which can be found very close to the phase boundary. Condensed domains within the chains could not be observed. Hence, the shrinking of the PSS chains in the presence of Al^{3+} was not as distinct as in the case of polyarcylates in the presence of alkaline earth cations, a feature which has also been observed with NaPSS in semi-dilute solution in the presence of Ba^{2+} cations.

Aside from the level of a monovalent salt, temperature turned out to be a tool to modify the L-type threshold line of alkaline earth salts of polyacrylates. An increase of T promotes shrinking of CaPA and SrPA coils and shifts the L-type threshold to lower values.[30] The shrinking of the AlPSS chains with increasing temperature fits to these observations as does the reversible aggregation and de-aggregation of AlPSS coils along temperature cycles which cross the threshold line. For AlPSS like for CaPA the binding of the SIC by the anionic polyelectrolyte chain is an entropically driven process. Although plausible, the temperature induced features do not obey a unique trend. As has been revealed by the work of Prabhu et al.[36,37] and by studies which went parallel to the present work, a temperature decrease causes a decrease of the solubility in solutions of NaPSS in the presence of Ba^{2+} cations. It is these subtle differences which offer great potential in applications and which makes it worthwhile to gain further knowledge on the solution behavior of polyelectrolytes in the presence of specifically interacting cations.

4.3 NaPSS in the Presence of Alkaline Earth Cations

4.3.1 Solution Behavior and Phase Diagram

The phase diagram of h-NaPSS-2 at [I]=0.1 M in the presence of Ba^{2+} can be subdivided into two regimes (Fig. 33). In an upper regime limited by a horizontal line, solutions become turbid and precipitation takes place. In the lower regime the samples remain clear.

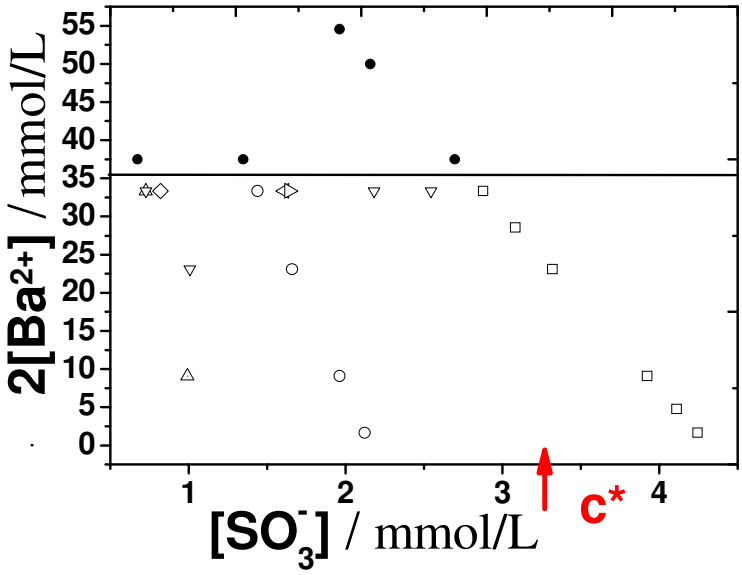

Figure 33: Phase diagram of h-NaPSS-2 in the presence of Ba^{2+} at [I]=0.1 M determined by visual inspection. The filled symbols show points where solutions became turbid. The open symbols represent clear samples. Data belong to the following dilution series: series 2 (□), series 3 (○), series 4 (△), series 5 (▽). The clear states of series 2 correspond to aggregates and the clear states of series 3, 4 and 5 are governed by single coils. The following three samples were characterized by light scattering at variable temperature: BaPSS-T-1 (◁), BaPSS-T-2 (▷) and BaPSS-T-3 (◇). An overlap concentration c* based on R_g in 0.1 M NaCl is indicated by the red arrow.

In the lower left part of the phase diagram solutions are clear and light scattering measurements reveal stable solutions of single coils. In the lower right part of the phase diagram solutions are also clear, but after a certain time aggregation sets in. In this region

the concentration of the NaPSS is close to or larger than the overlap concentration and the Ba^{2+}-cations may readily connect the coils in close contact. Although there are just a few aggregates, they affect the results of the SLS/DLS measurements. In the presence of aggregates the scattering curves of the SLS measurement bend in the low q-regime due to increased scattering intensities from the aggregates. The existence of aggregates are also proved by DLS measurements, which either reveals a second mode or a broadened peak in the CONTIN analysis[96,97] or a significant shift towards lower diffusion coefficients extracted from a cumulant analysis[56].

Compared to the respective phase behavior of sodium polyacrylate in the presence of alkaline earth cations the threshold line in the present case does not show a slope. Muthukumar et al. investigated NaPSS without inert salt in the presence of $BaCl_2$ and also found a horizontal phase boundary for PSS below the overlap concentration.[36,37] Compared to these results the threshold identified in the present case is shifted towards higher Ba^{2+} concentration, which is due to the presence of the inert salt. This effect has already been reported for CaPA, CaPMA and AlPSS and had been attributed to an exchange pressure on the domains of the polyelectrolyte coils exerted by the Na^+ cations of the inert salt.[12,18]

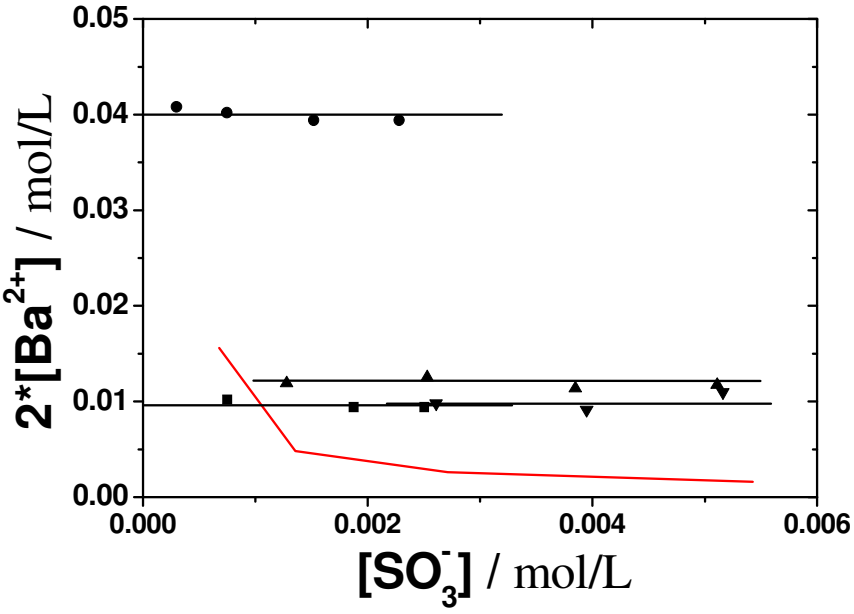

Figure 34: Phase diagrams of h-NaPSS-1 in the presence of Ba^{2+} at [I]=0.1 M (●) , h-NaPSS-1 at [I]=0 both at pH 6.5 (■), h-HPSS-1 at pH 3 (▲) and h-HPSS-1 at pH 5 both at [I]=0 (▼) determined by means of light scattering experiments. These data are compared with the visual observations by Keller et al.[21] with HPSS at pH 3 at [I]=0 (red line).

In contrast to the horizontal threshold lines found in the present work and by Muthukumar et al.[36,37], Keller et al.[21] reported a threshold for BaPSS, which obeys the law of mass action. Those authors used HPSS instead of NaPSS, as they performed their experiments at a pH of 3. They did not use an additional inert salt. In order to scrutinize this behavior, further experiments at variable pH and inert salt content were established. The regime was kept below the overlap concentration of h-NaPSS-1. Since turbidity for small PSS concentrations

in the presence of Ba^{2+} can be hardly observed by visual inspection, those experiments were performed by means of light scattering experiments.

The precipitation threshold of h-NaPSS-1 in salt free solution is shifted to lower values compared to the one observed at [I]=0.1 M, which can be explained by the impact of cation exchange (Fig. 34). However, a horizontal phase boundary was established under both conditions. Additional phase diagrams of acidic PSS at pH 3 and pH 5 also show horizontal phase boundaries. The slight increase of the threshold line with decreasing pH may be caused by the enhanced competition exerted by protons. Therefore we can neither confirm the results of Keller et al.[21], nor can we find the slightly negative slope of the threshold, reported by Dubin[35], for NaPSS in the absence of an inert salt.

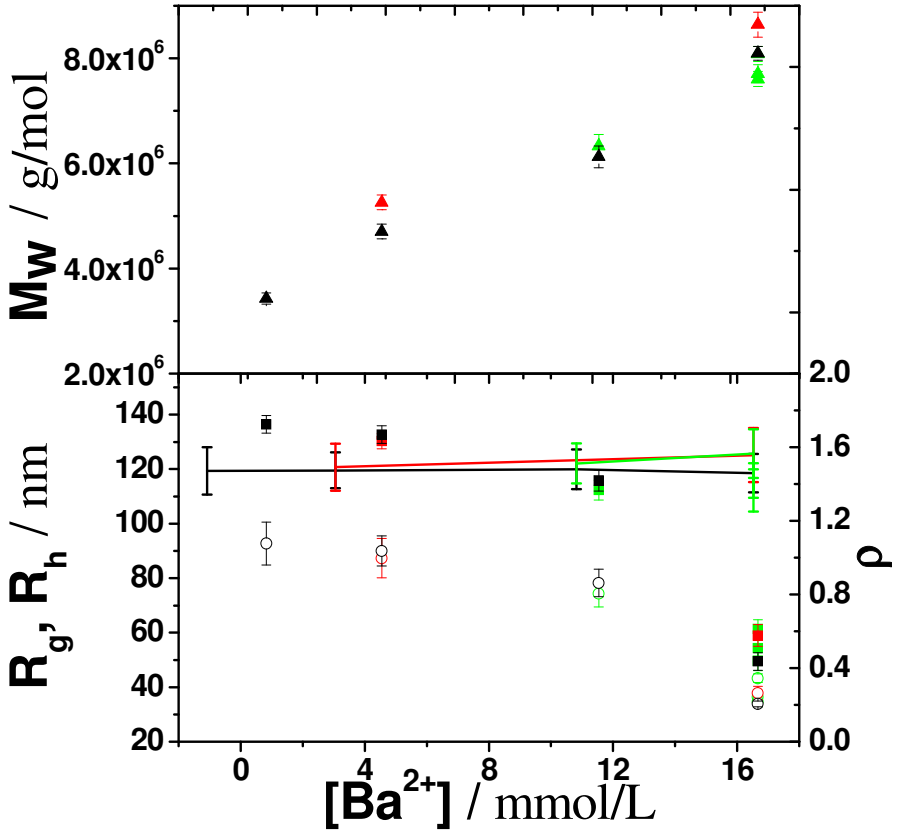

Figure 35: Average values of R_g (■), R_h (○), M_w (▲) and ρ (line) of series BaPSS-3 (black symbols), series BaPSS-4 (red symbols) and series BaPSS-5 (green symbols) along the respective paths which are denoted the phase diagram of aqueous BaPSS at [I]=0.1 M (Figure 33).

In close analogy to our earlier work on NaPA in the presence of SICs, we investigated the shrinking pattern of the PSS coils as a function of the Ba^{2+} concentration near the horizontal phase boundary. To this end solutions of h-NaPSS-2 close to the phase boundary separating single coils (low Ba^{2+} content) from the regime where aggregates or precipitates occur (higher Ba^{2+} content) have been analyzed by combined SLS/DLS. In total 4 series of samples were established in the regime where the samples remain clear and stable after mixing. To confirm stability of the samples the same samples were repeatedly analyzed. Except for the

respective sample closest to the precipitation threshold, all solutions did not only remain stable, but revealed the final coil size within minutes.

As an example the results from series BaPSS-3 are discussed. However it can be seen from Figure 35 that series BaPSS-4 and series BaPSS-5 reproduce independent from the PSS concentration nicely the values of series BaPSS-3. The radius of gyration R_g of the PSS coils extracted from SLS, decreases from 135 nm to 50 nm while increasing the amount of Ba^{2+}-cations. The Ba^{2+}-cations, as multivalent cations, can bind to more than one sulfonated group, which may lead to intramolecular crosslinking and charge neutralization. Neutralization as well as crosslinking induces a coil shrinking. The corresponding apparent molecular weight in dilution series 3 increases from 4000 to 8000 kDa in going from the point with the lowest concentration of Ba^{2+} to the point with the highest concentration of Ba^{2+}. This increase seems to contradict the stable state, where just single coils can be observed. However, the increase of the apparent molecular weight is only moderate and may be partly caused by a decoration of the coils with Ba^{2+}-cations which gradually changes NaPSS to BaPSS and which leads to a change in the scattering contrast (~dn/dc). The value of dn/dc enters the contrast factor K in eq 10 as squared value. Although, formation of aggregates cannot be entirely excluded and coexistence of a small fraction of oligomeric aggregates aside from a dominating monomeric chain may suffice to explain the increase of the apparent weight averaged molar mass by a factor of 2. If such a small extent of aggregation does occur it did not reverse the trend of coil shrinking, because the values for R_g and R_h are smaller than in case of the PSS coils without specifically interacting cations. This could be explained only by a partial aggregation which goes simultaneously along with a compaction of the aggregates.

The structure sensitive parameter, in all these cases lies in between 1.4 and 1.5 (Figure 35). A value of 1.6 is typical for an expanded coil. A compact sphere has a value of R_g/R_h = 0.77.[57,58] This suggests, that NaPSS keeps their coil-like structure in the presence of Ba^{2+} in all cases which have been analyzed in the present work.

The sample with the highest amount of Ba^{2+} in the dilution series 3 indicates an interesting trend with time. The radius of gyration and the hydrodynamic radius decrease over one day from 85 to 50 nm and from 65 to 35 nm respectively before approaching stable plateau values (Fig. 36). Whereas the size of the PSS coils show an initial drop constancy of the molecular weight excludes aggregation. Similar time dependent shrinking is also observed with the samples from the dilution series 4 and 5 which are closest to the phase boundary.

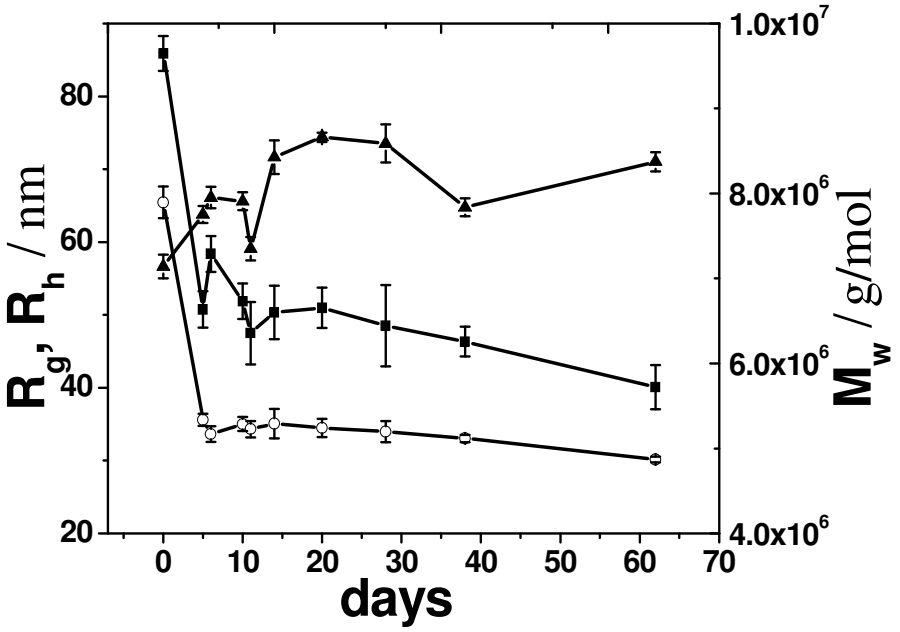

Figure 36: Variation of R_h (○), R_g (■), M_w (▲) for NaPSS at [I]=0.1 M in the presence of Ba^{2+} with time. The experiments, which extended over two months were carried out with the solution with the highest amount of Ba^{2+} in dilution series 3 of Figure 1 in the manuscript.

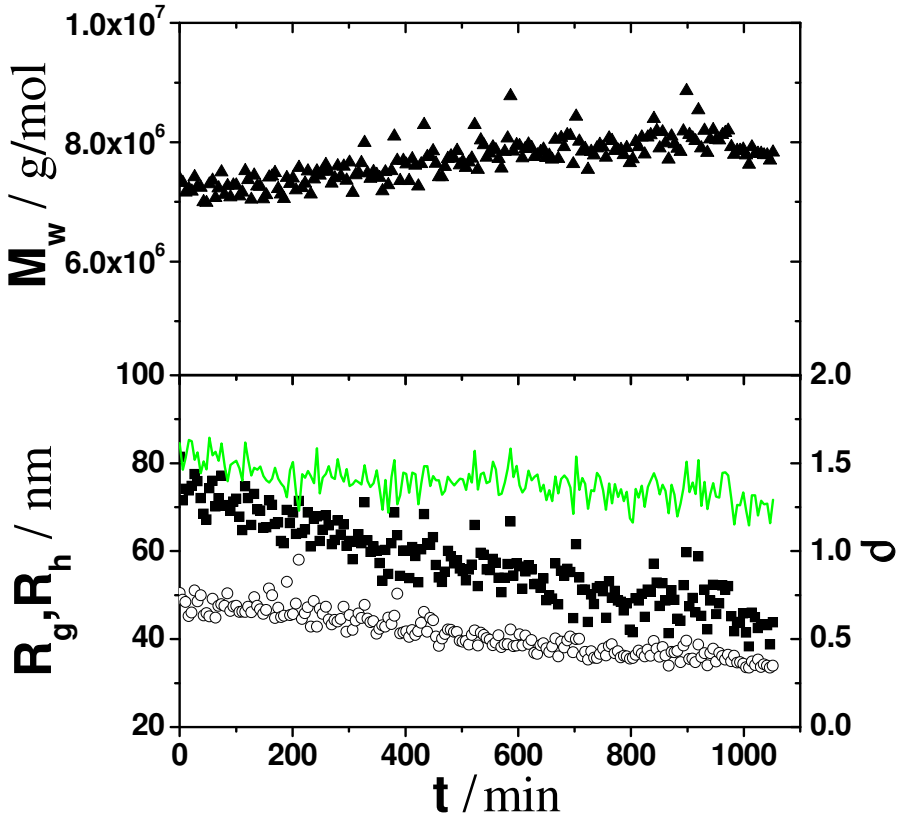

Figure 37: Variation of R_g (■), R_h (○), M_w (▲) and ρ (green line) with time t in sample BaPSS-T2 during the first hours after mixing the NaPSS solution with the corresponding BaCl solution at [I]=0.1 M.

The sharp drop in size observed during the first hours is analyzed in more detail with a time-resolved SLS/DLS-analysis of sample BaPSS-T-2 covering the first hours after mixing (Fig. 37). The values for the radius of gyration and the hydrodynamic radius decrease gradually over a time of 17 hours. Along with this gradual drop, the value for the structure sensitive parameter shows hardly any change fluctuating around $\rho \sim 1.4$ typical for coil-like structures. Constancy of the apparent M_w and ρ suggests that time resolved SLS/DLS records a self-similar shrinking over time.

In order to investigate whether the horizontal phase boundaries observed with Ba^{2+} are a general feature of aqueous solutions of alkaline earth salts of PSS, additional experiments have been performed with Sr^{2+} and Ca^{2+} cations. The phase diagrams for CaPSS and SrPSS which were established in the absence of an inert salt, do not show any phase boundaries. The samples remain clear even at alkaline earth cation concentrations as high as 1.6 mol/L (Fig. 38). This result renders further tests in solutions with an inert salt obsolete as the additional inert salt rather extends the regime of stable solutions than makes it narrower.

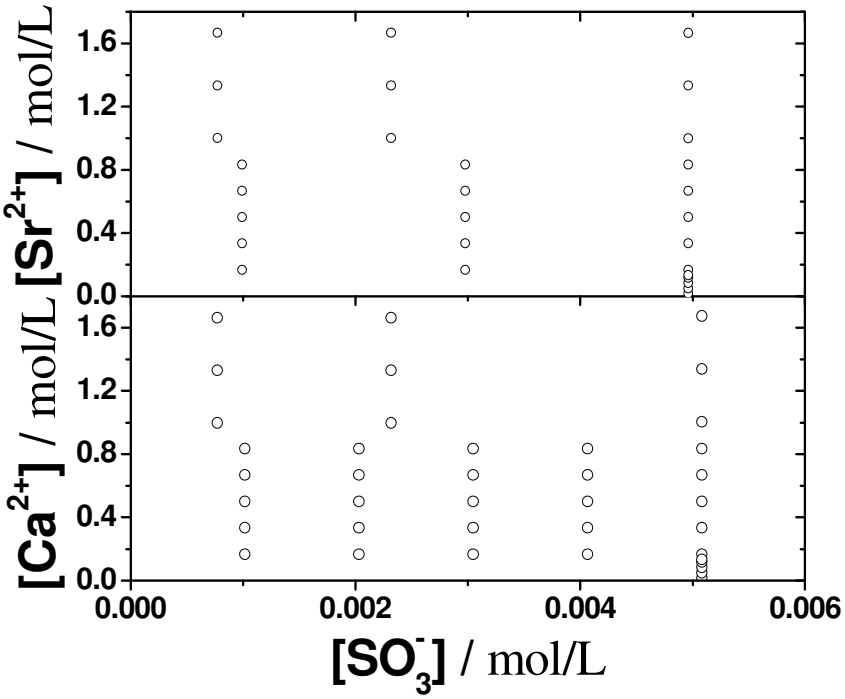

Figure 38: Phasediagram of SrPSS and CaPSS in pure water at 25°C. The open symbols represent stable and clear samples. Both phase diagrams were established with polymer sample h-NaPSS-3.

To further scrutinize the non-specific nature of interactions between Ca^{2+} and PSS light scattering experiments for CaPSS were performed with sample d-NaPSS at [I]=0.1 M. First, the apparent M_w increases by a factor of 2 as the concentration of Ca^{2+} is increased (Fig. 39). This increase starts at a value of $1.6 * 10^6$ g/mol and leads to $3.5 * 10^6$ g/mol, which is still close to the value specified in Table 14. Therefore, the increase of the apparent molecular weight is predominantly caused by a decrease in the second virial coefficient as the apparent M_w value only approaches the value determined by the characterization of the sample (Table

14). Second, values for R_g and R_h do not change as the Ca^{2+} concentration is increased. Due to the fact that Ca^{2+} had been introduced by replacing the respective amount of Na^+, the overall concentration of cationic charges remained constant. Accordingly the constancy of coil size is governed by [I]=0.1 M, which in turn points to non-specific interactions between Ca^{2+} and PSS, i.e. to its EIC nature.

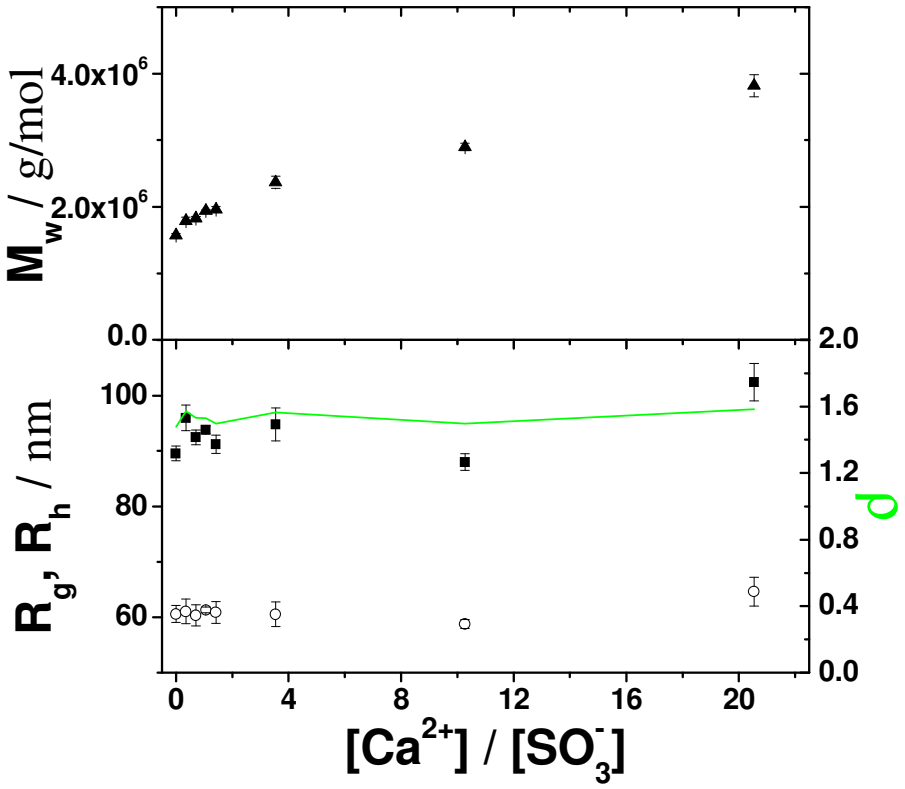

Figure 39: Variation of R_g (■), R_h (○), M_w (▲) and ρ (green line) as a function of the Ca^{2+}-concentration for sample d-NaPSS at [I]=0.1 M.

4.3.2 Temperature Dependent Coil Collapse

Lages et al.[30] showed that the coil collapse of polyacrylate chains in the presence of Ca^{2+}or Sr^{2+}-cations can be tuned by a variation of the temperature. An increase of the temperature from 15°C to 35°C led to a decrease in the R_g from 70 to 23 nm in case of the CaPA solutions. Obviously the binding of the cations to the ionic groups of the polyacrylate is entropically driven. ITC experiments performed by Antonietti et al.[29] on the same system corroborate this hypothesis. They observed a positive molar binding enthalpy of Ca^{2+} to COO^- residues, which for the first titration increment is 17 kJ/mol. Qualitative considerations revealed that ten water molecules and two Na^+-cations are liberated per Ca^{2+}-cation bound to COO^-.[29]

As BaPSS shows a phase behavior which differs significantly from that of alkaline earth salts of polyacrylates the question arises to which extent this finds expression in a temperature dependent variation of the coil dimensions for states close to the horizontal threshold line. Accordingly we investigated three different compositions by static and dynamic light

scattering. After each change of the temperature the variation of R_g, R_h and M_w was followed by time resolved SLS/DLS. It can be shown that the trends of R_g, R_h and M_w values as a function of temperature overlay for all three samples, independent from the PSS concentration (Fig. 40).

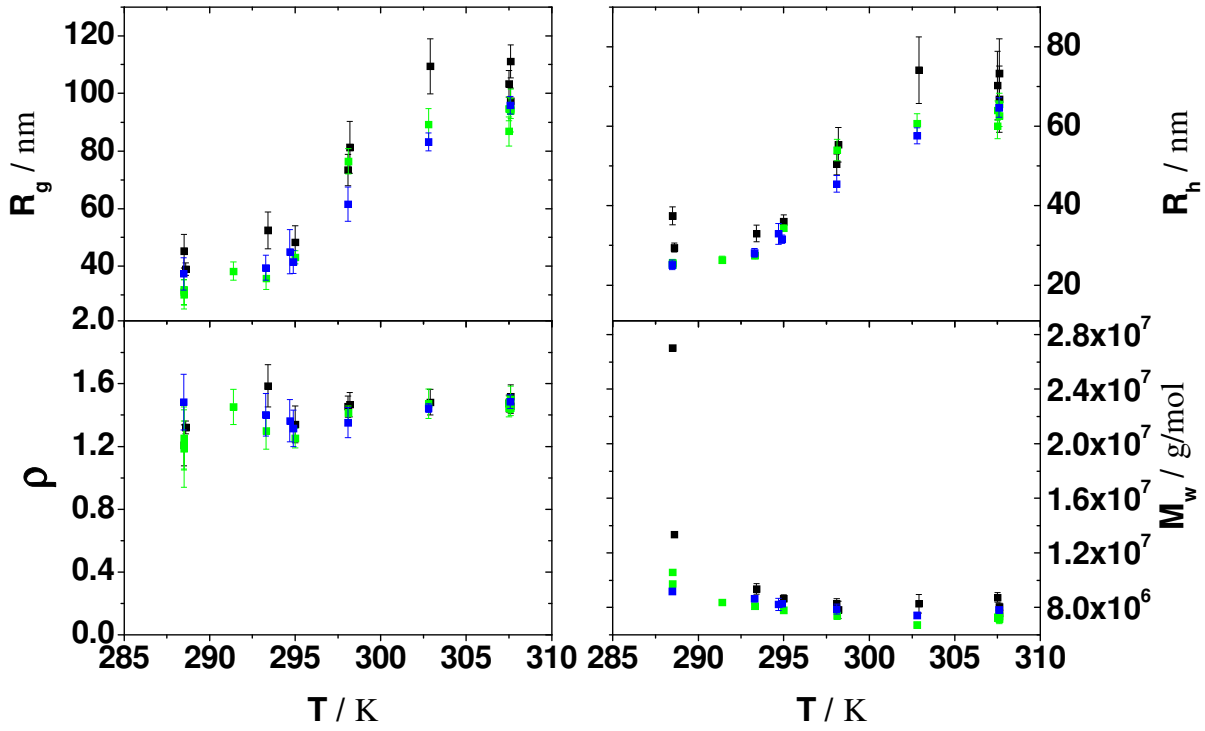

Figure 40: Rg, Rh, Mw and ρ in dependence of the temperature for sample BaPSS-temp-1 (■), BaPSS-temp-2 (■) and BaPSS-temp-3 (■).

The binding of the Ba^{2+}-cations to the styrene sulfonate monomers induces a strong temperature dependence of the coil dimensions. The plateau values which are adopted when the sample is equilibrated were used for further analyses. The R_g decreases with decreasing temperature from 90 nm to 30 nm. At the same time the R_h decreases from 60 nm to 25 nm. The corresponding structure sensitive parameter stays constant close to a value of ρ = 1.3-1.4, which indicates that the polymers keep a coil-like structure. At the same time the apparent molecular weight varies only slightly. Only at 15°C a strong increase in the scattering intensity sets in with time while the values of the hydrodynamic radius and the radius of gyration still remain constant. At a temperature of 12°C, all three values increase drastically with time, which indicates that aggregation sets in. The temperature dependent trends could be fully reversed by increasing the temperature. Strikingly, the response of the system towards the temperature variation is opposite compared to CaPA and SrPA. This suggests that the thermodynamics of the binding process of the Ba^{2+} cations to the sulfonated groups differs from that to carboxylate functions. Further details on the

thermodynamics of the binding process for different polyeletrolyte-SIC systems can be found in chapter 4.6.

4.3.3 SANS/SAXS Experiments

Anionic polyacrylate chains undergo a continuous transformation from extended coils to highly compact spheres upon addition of alkaline earth cations, whereby pearl necklace-like states are adopted at compositions close to the phase boundary.[13,25] In the present study, we will try to learn, if similar intermediate structures exist in solutions with BaPSS. Although the shape sensitive ρ-parameter remains constant, a constant ρ-ratio cannot fully exclude pearl necklace-like intermediates, because pearl necklace-like intermediates might also adopt ρ-values similar to those of coils. In order to shed further light on the structure of intermediates along paths approaching the phase boundary of dilute solutions of BaPSS at [I]=0.1 M small angle neutron and x-ray experiments were carried out.

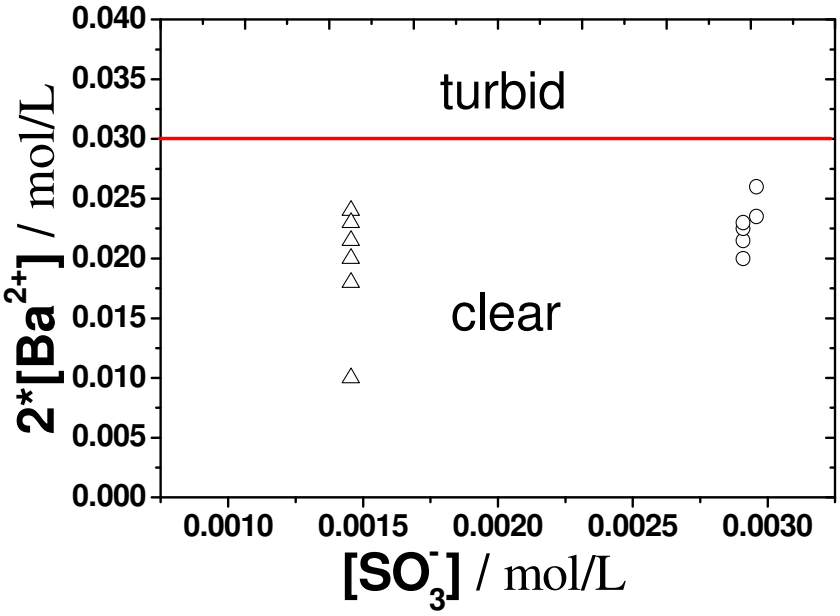

Figure 41: Phase diagram of BaPSS at [I]=0.1 M in D_2O determined by visual inspection. The experiments were carried out with sample h-NaPSS-1. The open symbols represent clear samples from two different dilution series, which were analyzed by SLS/DLS and SANS: BaPSS-SANS-1 (△) and BaPSS-SANS-2 (○).

In order to guide SANS experiments with suitable samples, a phase diagram had to be established for h-NaPSS-1 at [I]=0.1 M in deuterated aqueous solutions in the presence of Ba^{2+}-cations (Fig. 41). As expected a phase diagram could be revealed for h-NaPSS-1 in D_2O which is similar to the one shown in Fig. 33 for h-NaPSS-2 in H_2O and in Fig. 34 for h-NaPSS-1 in H_2O. The phase boundary of h-NaPSS-1 in D_2O remains horizontal, but is shifted to values of a Ba^{2+}-concentration lower than in case of H_2O (Fig. 41). In total three series of samples with two different polymers were established and analyzed by SLS/DLS and SANS. Discussion is focused on series BaPSS-SANS-1 and BaPSS-SANS-2 which were established with sample h-NaPSS-1. It can be nicely shown that the light scattering results of both series as a function of $[Ba^{2+}]$ overlay each other (Figure 42). The value for R_g decreases with increasing $[Ba^{2+}]$ from 86 nm to 33 nm in series BaPSS-SANS-1 and from 40 nm to 27 nm in series BaPSS-SANS-

2. The same trend can be observed with the R_h which decreases from 50 nm to 20 nm in series BaPSS-SANS-1 and from 24 nm to 18 nm in series BaPSS-SANS-2. The value for the structure sensitive parameter remains constant at a value of 1.6.

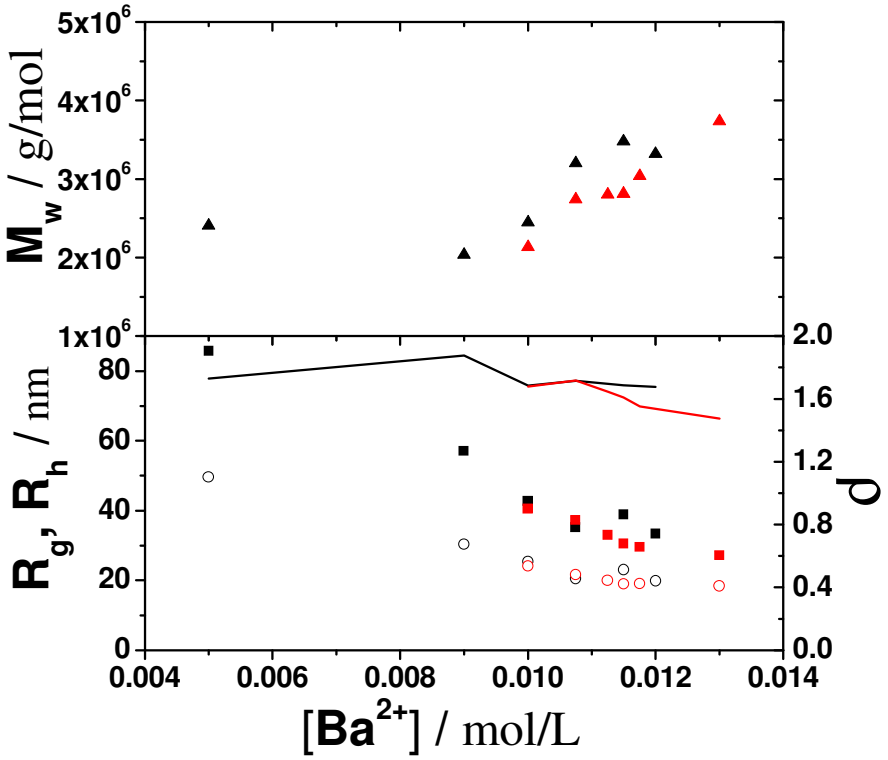

Figure 42: R_g (■), R_h (○), M_w (▲) and ρ (line) as a function of the Ba^{2+}-concentration for BaPSS-SANS-1 (black symbols) and BaPSS-SANS-2 (red symbols). The series were established with sample h-NaPSS-1 at [I]=0.1 in deuterated aqueous solutions.

Six samples of each series were selected for an investigation with SANS. The scattering curves obtained from the SANS experiment were merged with the respective curves from light scattering, by multiplying the light scattering curves with appropriate shift factors.

Log-log plots of the scattering curves with the lowest Ba^{2+}-content exhibit a slope close to but always below -2. A power law with an exponent close to -2 suggests a structure of an unperturbed coil. A coil expanded under good solvent conditions shows an exponent of -1.67. The samples with the higher Ba^{2+} contents, which are closer to the phase boundary show a slope close to -3, which is a hint for a more compact structure (Fig. 43 and Fig. 45). A 3D Kratky plot, which contains all six scattering curves, better illustrates the structural change PSS coils undergo with increasing Ba^{2+}-content (Fig. 44 and Fig. 46). In the Kratky plot the scattering intensity I(q) is multiplied with q^2. Therefore the first three scattering curves of sample series BaPSS-S1 and sample BaPSS-S2-1, which show a power law with an exponent of -2 turn into a plateau. In the scattering curves with a higher Ba^{2+}-content a peak appears in the Kratky plots, which becomes higher with increasing Ba^{2+}-concentration. Peaks in the Kratky plot point to domains with a more compact structure. The position of the peak maximum is correlated with the size of the compact domain or sphere according to

$q_{max}=2.5/R_{g,domain}$ or $q_{max}=2.081/R_{sphere}$ respectively.[98] Accordingly, the present peaks suggest domains with Rg~13 nm, which is 2 to 3 times smaller than the size of the entire shrinking coil, where a range of 33 nm < R_g < 38 nm has been detected by SLS. Compact domains, which are significantly smaller than the overall size of the coils may be attributed to the formation of pearl necklace chains (Table 20). However a shoulder in the low q-regime of the scattering curve, characteristic for a pear-pearl distance in such a chain cannot be clearly identified.

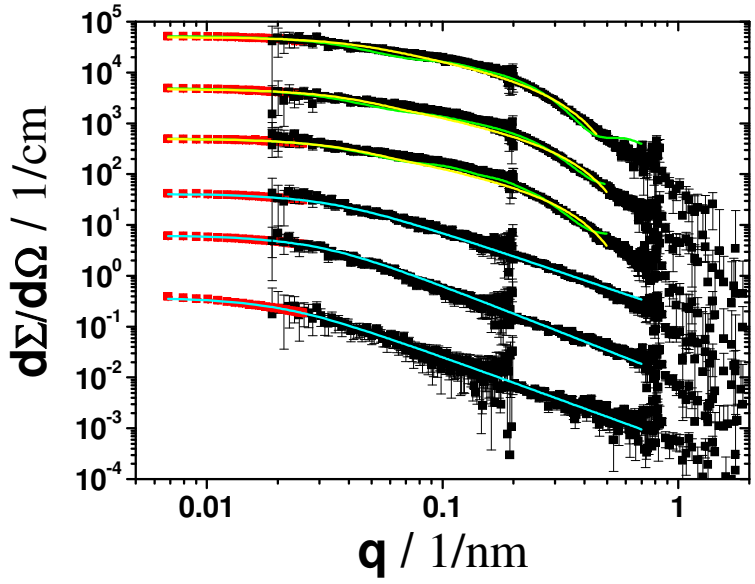

Figure 43: Combined SLS(■) and SANS(■) scattering curves of sample series BaPSS-S1 from bottom to top with increasing content of Ba^{2+} in comparison to the corresponding polymer excluded volume fit (light blue lines)[73,74], cylinder model fit (yellow line)[50] and pearl necklace model fit (green line)[26]. The respective fitting parameters are shown in Tab. 2. The curves are increasingly shifted by a factor of 10^0, 10^1, 10^2, 10^3, 10^4 and 10^5

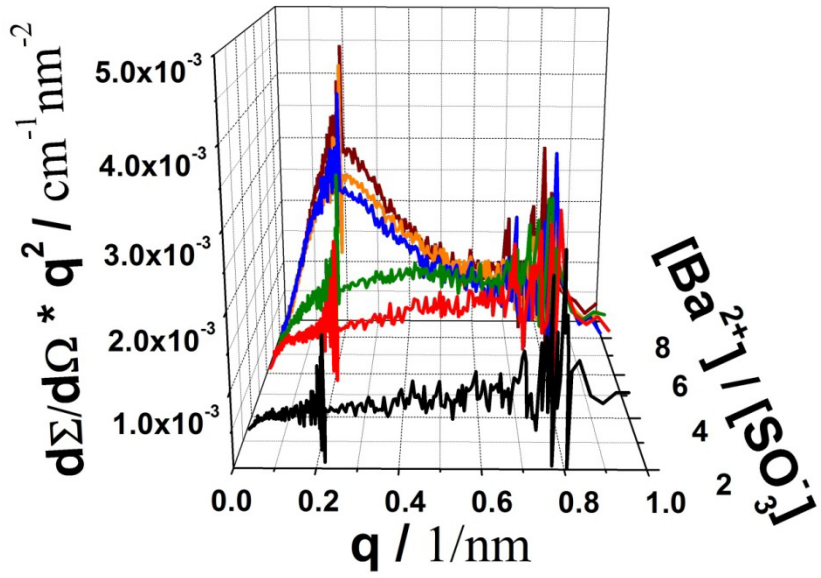

Figure 44: Kratky plots of the combined SLS and SANS curves of the samples from BaPSS-SANS-1 represented as a function of the ratio Ba^{2+}/SO_3^- in a 3D-plot.

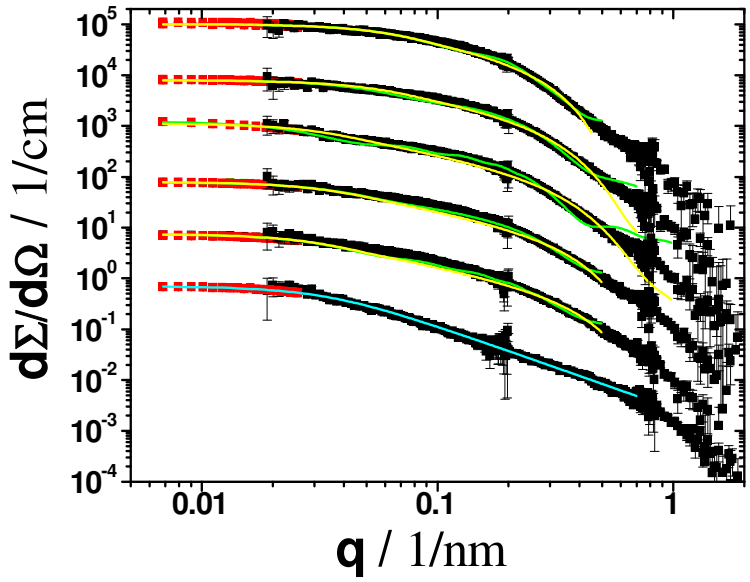

Figure 45: Combined SLS(■) and SANS(■) scattering curves of sample series BaPSS-S2 from bottom to top with increasing content of Ba^{2+} in comparison to the corresponding polymer excluded volume fit (light blue lines)[73,74], cylinder model fit (yellow line)[50] and pearl necklace model fit (green line)[26]. The respective fitting parameters are shown in Tab. 2. The curves are increasingly shifted by a factor of 10^0, 10^1, 10^2, 10^3, 10^4 and 10^5

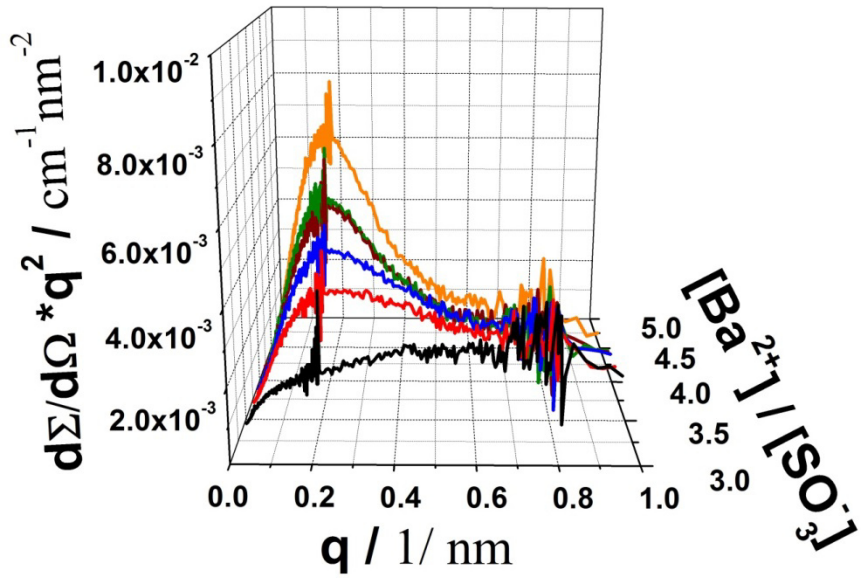

Figure 46: Kratky-plots of the combined SLS and SANS curves of the samples from BaPSS-SANS-2 represented as a function of the ratio Ba^{2+}/SO_3^- in a 3D-plot.

The three scattering curves with the lowest Ba^{2+}-content of sample series BaPSS-S1 and sample BaPSS-S2-1 were fitted with the model of a polymer chain with excluded volume based on the theory of Benoit[73] and Hammouda[74] with the SasView program. For these curves a good agreement is achieved between SLS/SANS curves and model curves (Fig. 43, Fig. 45 and Tab. 20). The three scattering curves with the highest amount of Ba^{2+} of sample series BaPSS-S1 and the five scattering curves with the highest amount of Ba^{2+} of sample

series BaPSS-S2 were fitted by a cylinder model and a pearl necklace model, however, none of these models fit the scattering curves perfectly (Fig. 43, Fig. 45 and Tab. 20). The structure could well be more cigar like or the neighboring pearls could exhibit irregular distances and/or shapes. This would explain, why the shoulder at low q correlating with the distance of the compact domains is missing and why the pearl necklace model and the cylinder model do not perfectly reproduce the experimental scattering curves.

Table 20: Fit parameters obtained from different models applied on combined SLS/SANS scattering curves from sample series BaPSS-S1.

model of a polymer with excluded volume[73,74]					
sample	R_g(fit) nm	Porod-Exponent		χ^2 Npts	R_g(SLS) nm
BaPSS-S1-1	66.2	1.69		1.310	85.8
BaPSS-S1-2	47.7	1.83		2.377	57.1
BaPSS-S1-3	39.6	1.58		2.118	42.7
BaPSS-S2-1	39.7	1.65		0.991	40.6
model of a cylinder[50]					
sample	R_g from fitting parameters	length nm	radius nm	χ^2 Npts	R_g(SLS) nm
BaPSS-S1-4	31.6	108.8	5.2	6.975	35.3
BaPSS-S1-5	30	103.2	5.1	14.328	38.9
BaPSS-S1-6	22.1	75.2	5.6	8.1322	33.3
BaPSS-S2-2	38	131.9	4.5	40.26	37.3
BaPSS-S2-3	31.1	107.1	4.9	18.547	33
BaPSS-S2-4	34.5	119.2	4.1	28.01	30.5
BaPSS-S2-5	19.9	67.9	5.2	14.613	29.6
BaPSS-S2-6	19.2	64.4	6.6	42.67	27.3

model of a pearl necklace[26]						
sample	R_g from fitting parameters	Number of pearls	pearl radius nm	edge separation nm	X^2 Npts	R_g(SLS) nm
BaPSS-S1-4	32.5	2	9.8	56.9	2.94	35.3
BaPSS-S1-5	35.8	2	9.3	64.4	3.373	38.9
BaPSS-S1-6	31.5	2	9.4	51.6	6.453	33.3
BaPSS-S2-2	37.1	2	9.7	75.8	37.13	37.3
BaPSS-S2-3	31.4	2	9.5	50.8	7.277	33
BaPSS-S2-4	46.2	2	9.9	89.5	25.232	30.5
BaPSS-S2-5	23.9	2	8.23	30.43	9.099	29.6
BaPSS-S2-6	18.8	2	9.24	18.18	39.5	27.3

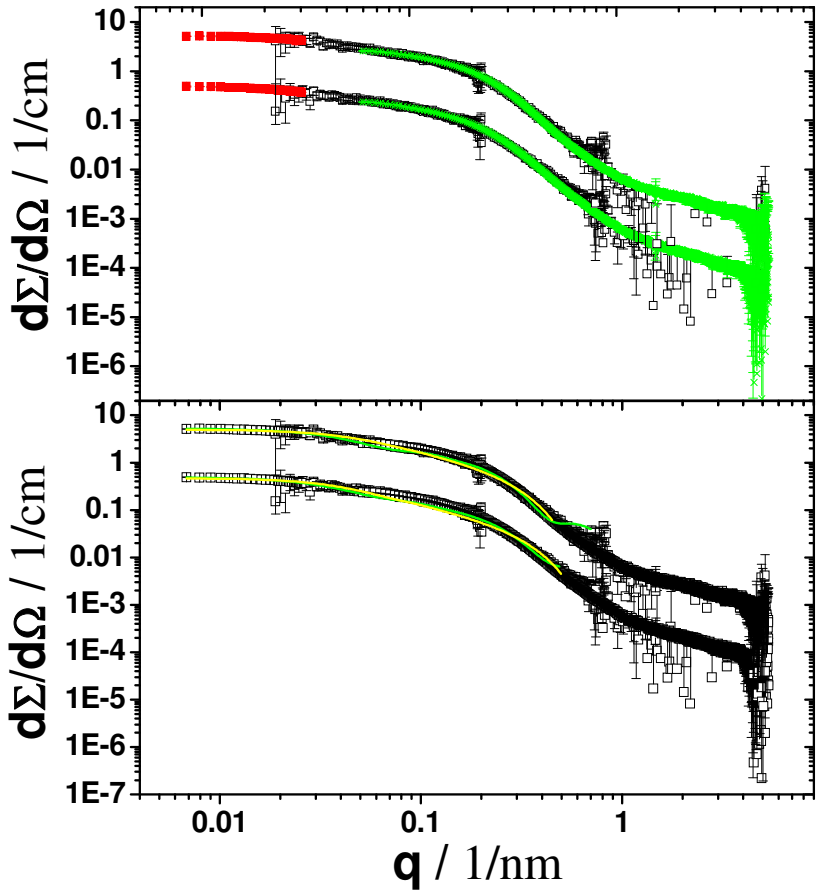

Figure 47: A) Combined SLS(■), SANS(□) and SAXS(X) scattering curves of sample BaPSS-S1-6 (upper curve) and BaPSS-S1-5 (lower curve). B) The same data as shown in A are compared to the respective fit with the cylinder (yellow line) and pearl necklace chain (green line) model. The SLS and SAXS curves are adjusted to the respective SANS experiments. In both graphs the values of the combined BaPSS-S1-6 scattering curve was multiplied by a factor of 10.

Two of the six samples from each sample series (BaPSS-S1-5, BaPSS-S1-6, BaPSS-S2-4 and BaPSS-S2-6) were further analyzed by SAXS in order to turn the focus onto the distribution of the Ba^{2+} cations within the shrinking BaPSS chains. The first SAXS curve of each sample was overlaid with the respective SLS/SANS curve by multiplying it with the proper shift factor. As it is clearly demonstrated in Figure 47 and Figure 48 SAXS and SANS curves perfectly overlay. It can thus be concluded that the distribution of Ba^{2+} follows the distribution of SO_3^- residues.

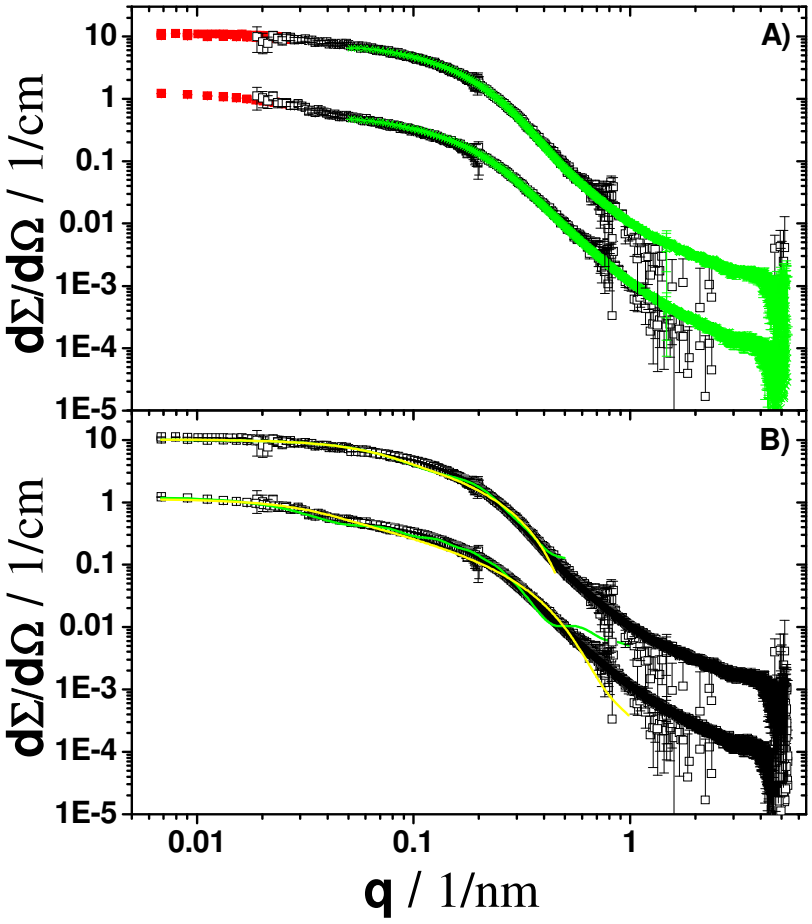

Figure 48: A) Combined SLS(■), SANS(□) and SAXS(X) scattering curves of sample BaPSS-S2-6 (upper curve) and BaPSS-S2-4 (lower curve). B) The same data as shown in A are compared to the respective fit with the cylinder (yellow line) and pearl necklace chain (green line) model. The SLS and SAXS curves are adjusted to the respective SANS experiments. In both graphs the values of the combined BaPSS-S2-6 scattering curve was multiplied by a factor of 10.

Another feature of the SAXS curve turned out to be even more striking. In the regime of $1 < q < 5$ nm^{-1} where SANS already suffered from poor data quality the SAXS data still remain significant and showed a trend of $d\Sigma/d\Omega \sim q^{-1}$. As this q-regime probes segments smaller than the persistence length, which is in the order of nm, q^{-1} trend indicates that elongated string-like elements survived within the shrinking chains and thus further supports the pearl necklace shape for the must shrunken species (Fig. 49 and Fig. 50).

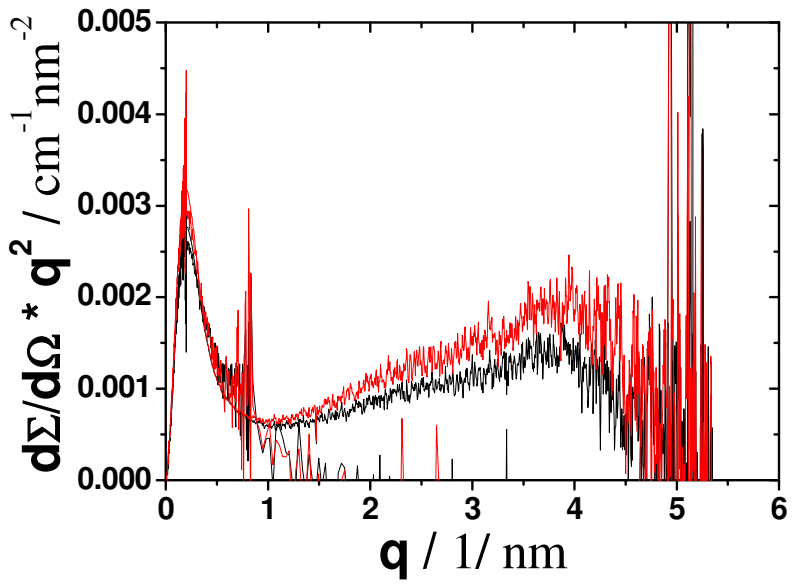

Figure 49: Kratky plot of combined SANS) and SAXS scattering curves of sample BaPSS-S1-5 (black) and BaPSS-S1-6 (red).

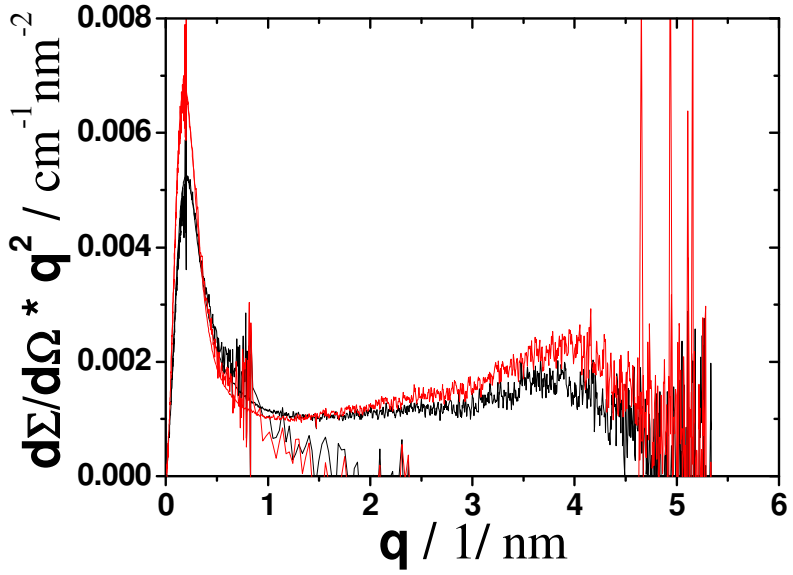

Figure 50: Kratky plot of combined SANS) and SAXS scattering curves of sample BaPSS-S2-4 (black) and BaPSS-S2-6 (red).

In case of CaPA the shrinking of the coils, was much more pronounced, where a transition from coils towards spheres could be observed by approaching the phase boundary.[12] By comparing dilute solutions of AlPSS directly with dilute solutions of BaPSS, beginning from the same starting point (h-NaPSS-2, R_g 138 nm), it can be demonstrated that the finally achieved degree of shrinking of the PSS chains, is stronger in case of the BaPSS (h-NaPSS-2, R_g 50 nm) than in case of AlPSS (h-NaPSS-2, R_g 85 nm)[Chapter 4.2.1 and Chapter 4.3.1].

Small angle scattering experiments on solutions of CaPA and PbPA revealed pearl necklace-like intermediate states[15,25], which could not be confirmed for AlPSS, where the chains remain coil-like, even close to the threshold [Chapter 4.2.3]. Yet, for BaPSS condensed

domains could be established via SANS and SAXS experiments at intermediate states in the BaPSS phase diagram. These condensed domains are best compatible with an irregular pearl necklace chain showing a distribution of pearl-pearl distances along the chain and having irregular pearl-like domains with an averaged radius close to 10 nm. This is close to the value inferred from the peak maximum of the Kratky plot.

4.3.4 Aggregation Experiments with BaPSS

The aggregation of the BaPSS coils was induced by two different methods; by component mixing and by temperature variation. For the first method points were selected in the phase diagram, which are located close to the phase boundary (open circles in Fig. 51).

For the aggregation induced by component mixing the samples were mixed, shaken by hand and placed in the goniometer of the light scattering instrument immediately after homogenization. Subsequently the time dependent light scattering measurement was started. The results of three different measurements will be shown with only measurement BaPSS-CM-3 discussed in detail. Two samples denoted as BaPSS-CM-2 and BaPSS-CM-3 exhibit the same sample composition and have the highest content of Ba^{2+}. Sample BaPSS-CM-1 has the same PSS concentration and differs only in the Ba^{2+}-content (Fig. 51). After an induction period of 1000 min, the BaPSS coils which had a size of R_g in between of 80 and 95 nm, began to aggregate (Fig. 52).

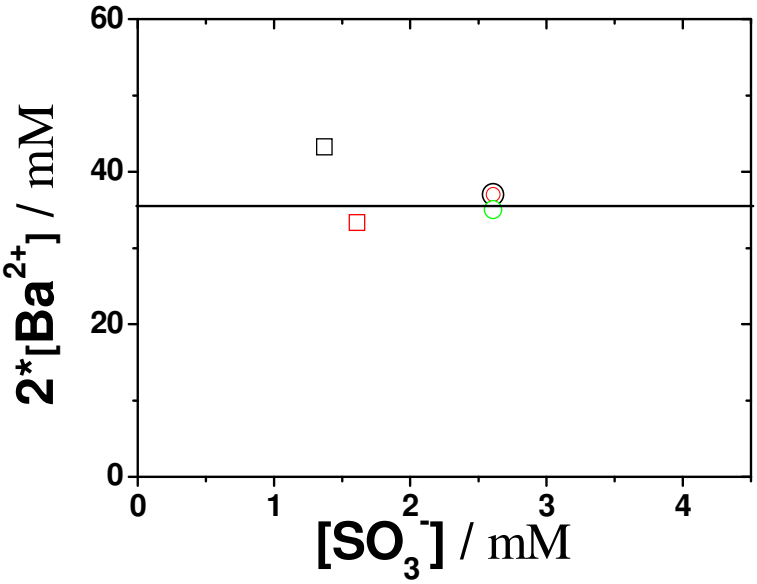

Figure 51: Phase diagram of h-PSS-2 in the presence of Ba^{2+}-cations at [I]=0.1 M. All states represent samples which were analyzed by time resolved light scattering: BaPSS-TI-1 (□), BaPSS-TI-2 (□), BaPSS-CM-1 (○), BaPSS-CM-2 (○) and BaPSS-CM-3 (○). While squares illustrate samples of aggregation experiments, which were induced by a temperature jump, states of aggregation experiments induced by component mixing are represented by circles.

The induction period elongated with decreasing Ba^{2+}-content. In the beginning a fast increase in size up to R_g=140 -160 nm and in mass from $1*10^7$ towards $1.5*10^7$ g/mol was observed. Thereafter the increase in size and mass with time became less drastic. The value for the structure sensitive parameter decreased from 1.6 towards 1.2 which gives a hint that

the structure became more compact. A closer look on the beginning of the process shows that compared to the light scattering experiments done with the same polymer at [I]=0.1 on stable samples, the values for R_g and M_w were a little higher, which could be a hint that directly after the mixing process a certain fraction of the BaPSS chains is already aggregated (Fig. 52). Also a post shrinking process which was typical for stable samples with a high Ba^{2+}-content is only visible for the unstable sample with the lowest Ba^{2+}-content in the series, denoted as BaPSS-CM-1 (Fig. 52 A). For this particular sample the structure sensitive parameter started with a value of 1.2 and rised to 1.6 with the beginning aggregation process, which may indicate that the degree of aggregation right after mixing is lower compared to the two samples with the higher Ba^{2+}-content (Fig. 52).

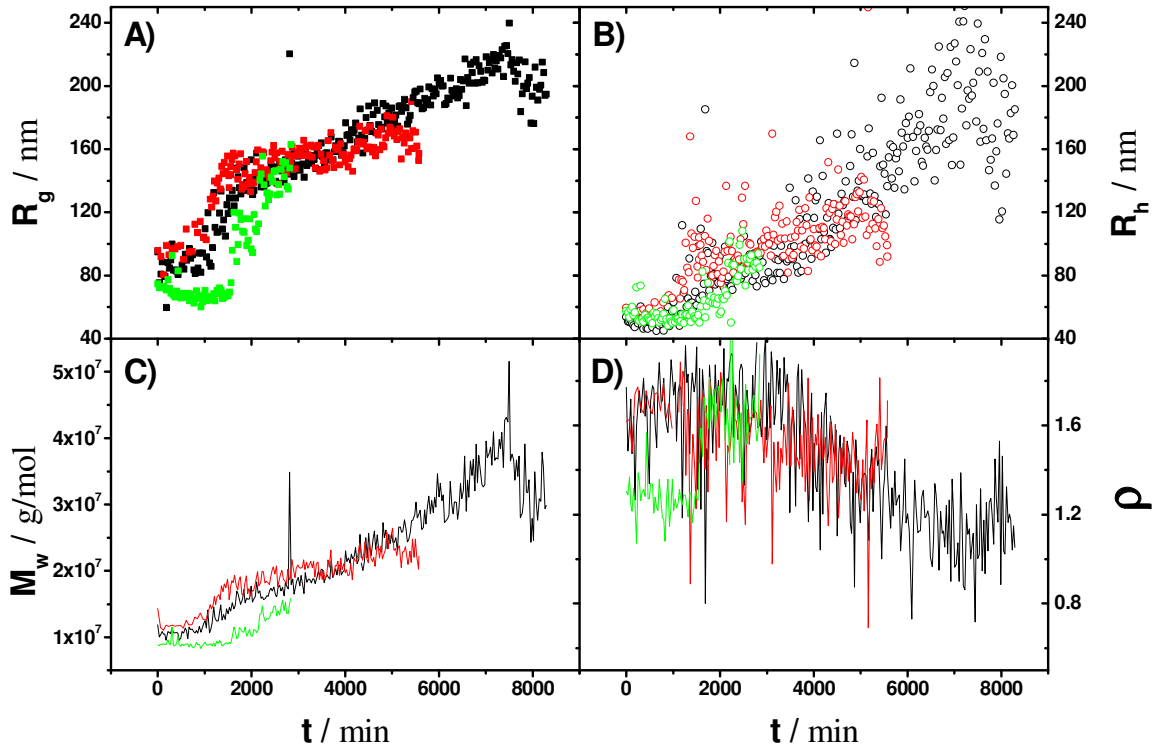

Figure 52: Results of the aggregation experiments iduced by component mixing: A) R_g vs time, B) R_h vs. time, C) M_w vs. time and D) ρ vs. time for the samples BaPSS-CM-1 (green) BaPSS-CM-2 (red) and BaPSS-CM-3 (black).

A logarithmic plot of R_g versus M_w or R_h versus M_w provides information on the morphology of the aggregating particles once it obeys a power law of the form,

$$R_g \approx M_w^{\alpha} \tag{66}$$

resulting in α=0.33 for compact spheres, 0.6 for self-avoiding walks and 1.0 for rods.[99] By plotting R_g and M_w of sample BaPSS-CM-3 in such a plot, it can be seen that the exponent decreases from 1.2 in the beginning over 0.6 towards 0.38 (Fig. 53). Exponents which are larger than 1 are unusual.

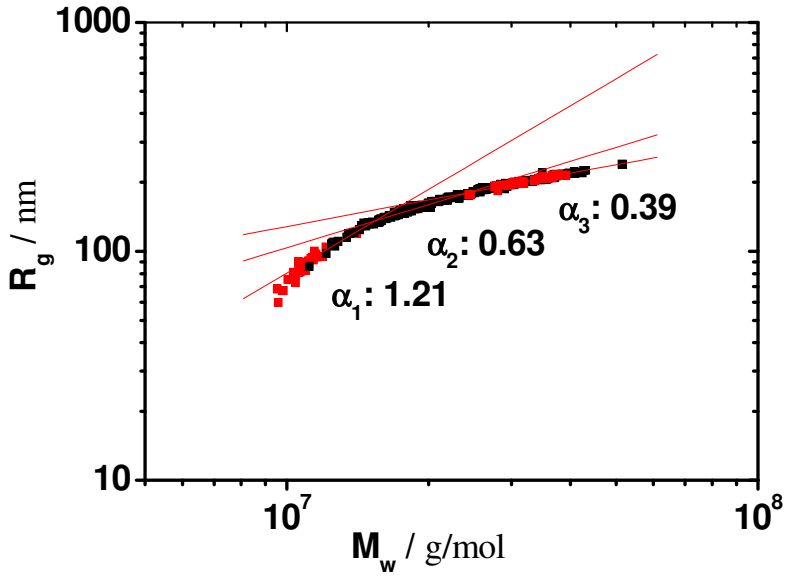

Figure 53: A logarithmic plot of R_g versus M_w for sample BaPSS-CM-3.

However, an explanation could be that the polydispersity of the sample was large in the beginning of the aggregation process. A decreasing exponent can be a first sign that the aggregates became denser during the aggregation process. In the end of the process the exponent exhibits a value close to the one which is expected for compact spheres. By comparing the R_g/M_w plots of sample BaPSS-CM-1, BaPSS-CM-2 and BaPSS-CM-3 it can be observed that the trend is reproducible and that the trends of the different samples overlay independent from small changes in the Ba^{2+}-content (Fig. 52 and Fig. 57).

For the temperature induced aggregation experiments two samples differing in polymer molecular weight (d-NaPSS and h-NaPSS-2), in polymer concentration and in different Ba^{2+}-contents were mixed. After mixing the samples were placed in the goniometer and heated. Subsequently the aggregation was induced by cooling down the sample in the goniometer.

In the following the sample denoted as BaPSS-TI-1 is discussed in detail. The sample was generated with the help of polymer d-NaPSS at [I]=0.1 M. This sample was turbid at room temperature. After heating to 38°C, the sample was checked by a time resolved light scattering experiment for single coil behavior. Subsequently the sample was cooled down to room temperature (Figure 54, bottom). As a consequence the radius of gyration was shrinking from 70 nm to 45 nm which is in line with the temperature dependent shrinking experiments on BaPSS reported in Chapter 4.3.2. Afterwards the aggregation started. The radius of gyration increased from 45 nm to 250 nm. At the same time a drastic increase of the molecular weight from $2.64*10^7$ g/mol to $2.0*10^9$ g/mol became visible. The structure sensitive parameter changed from 1.6 to values below 0.8, which serves as a hint that the aggregates become more compact during the process. In the beginning of the experiment the shrinking of the BaPSS coils went along with a strong increase of the M_w from $4.73*10^6$ g/mol to $2.64*10^7$ g/mol. However, this effect is still not settled. It may be explainable by a

building of fluffy aggregates which shrink at the same time. This assumption is underlined by the value of the structure sensitive parameter which increases after 150 minutes from 1.2 to 1.6.

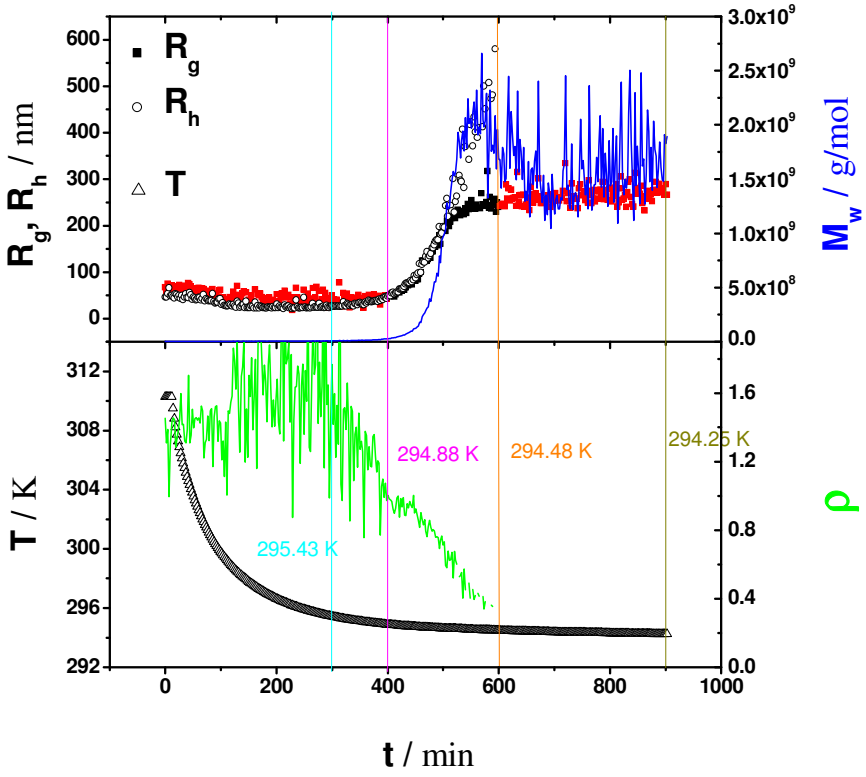

Figure 54: R_g (■), R_h (○), M_w (blue line) and ρ (green line) as a function of time and temperature (△) for sample BaPSS-TI-1.

Aggregation of BaPSS-TI-2 showed trends comparable to BaPSS-TI-1. The most important difference between both samples is the molecular weight and that sample BaPSS-TI-2 was cooled in more steps until aggregation occurred. The aggregation process of BaPSS-TI-2 represents the last cooling step from 15°C to 12°C of the temperature dependent light scattering experiment done with sample BaPSS-temp-1 [Chapter 4.3.2]. In contrast to sample BaPSS-TI-1, BaPSS-TI-2 was generated with polymer sample h-NaPSS-2.

Adaption of R_g versus M_w obtained from aggregation experiment with sample BaPSS-TI-1 according to eq 66 gives a slope of α=0.39 which is a hint that also in the case of the temperature induced aggregation experiments compact aggregates are formed. But in contrast to the experiments which were induced by component mixing these compact aggregates are formed directly from the beginning of the process (Fig. 56).

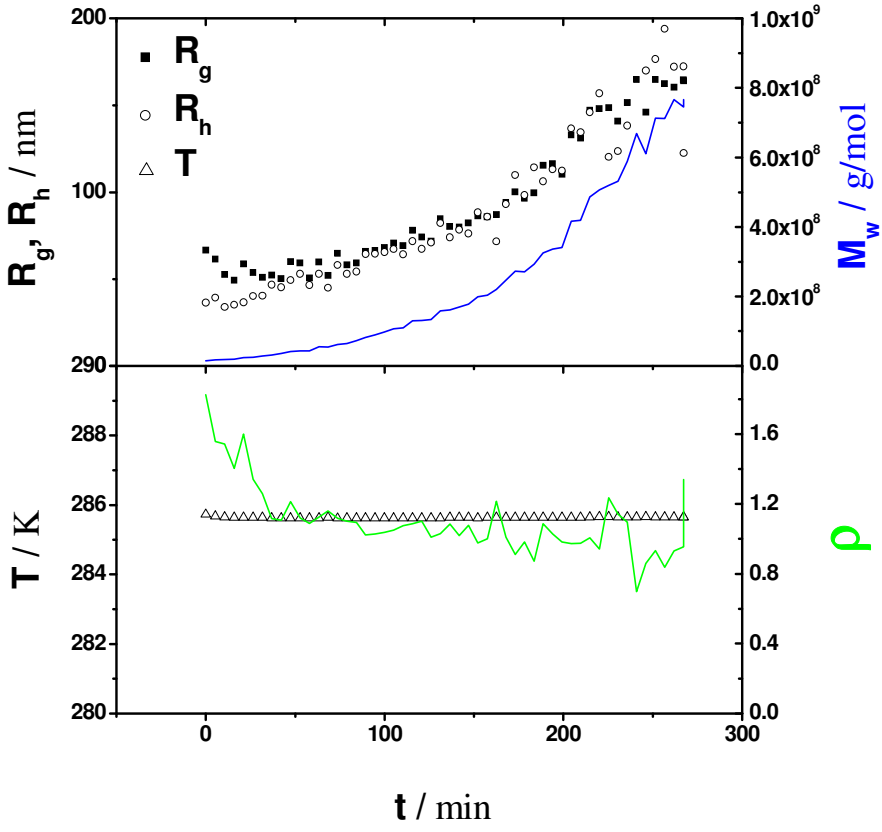

Figure 55: R_g (■), R_h (○), M_w (blue line) and ρ (green line) as a function of time and temperature (△) for sample BaPSS-TI-2.

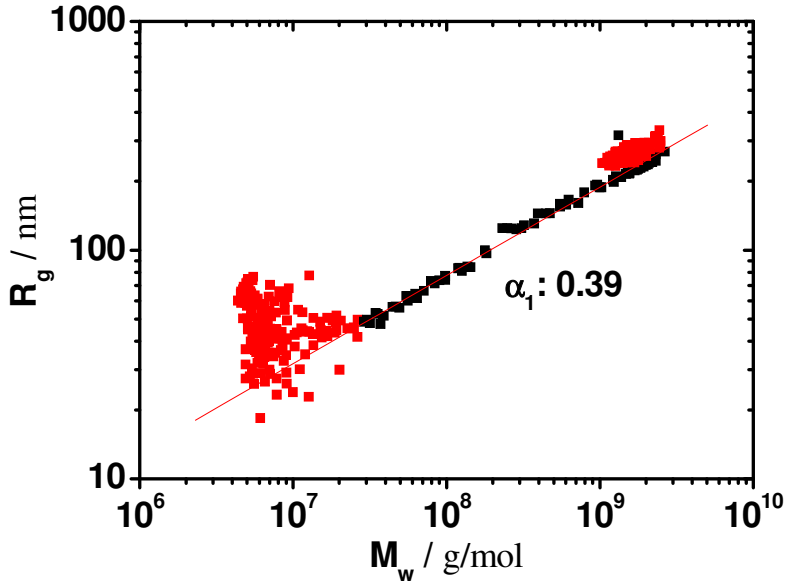

Figure 56: A logarithmic plot of R_g versus M_w for sample BaPSS-TI-1.

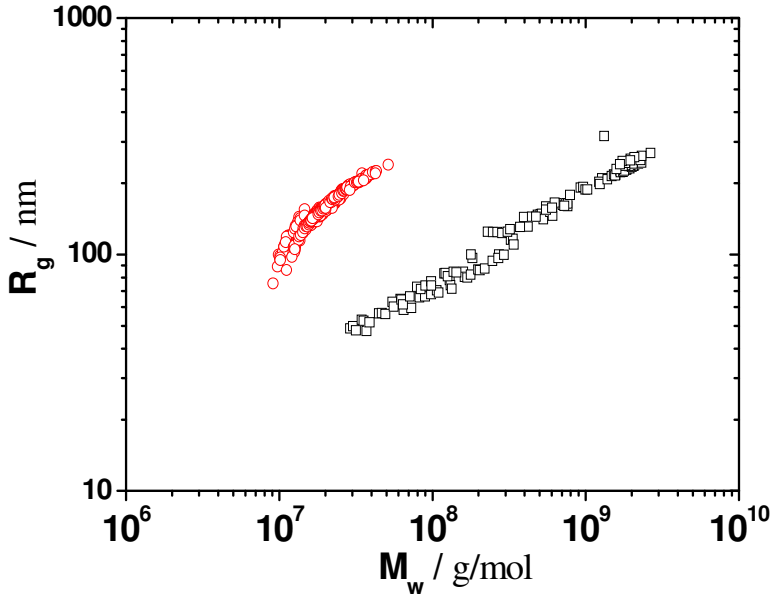

Figure 57: Comparison of the R_g vs. M_w trend for all aggregation experiments induced by component mixing ○ and by T variation □.

By comparing all five experiments in one logarithmic plot of R_g versus M_w it can be observed that the experiments with the same induction method follow the same trend and that both methods lead in the end to comparable compact structures inferred from the approach of an exponent close to 1/3 (Fig. 57).

The explanation for the different trends in the beginning could be that the coils in the temperature induced aggregation assemble more gradually and allow premature and simultaneous compaction, while the coils in the aggregates induced by component mixing aggregate much faster, thereby kinetically trapping extended states which inhibit further shrinking.

4.3.5 Summary

The phase boundaries of BaPSS established in the present work below the overlap concentration of the respective PSS coils follow horizontal trends independent of the PSS concentration. The height of the threshold increases at low pH and increases in the presence of an EIC salt like NaCl but remains horizontal. A phase boundary which follows the law of mass action[21] or which has a slightly negative slope[35] could not be verified.

The intercept of the horizontal phase boundary of BaPSS without inert salt exhibits a value of 5 mM [Ba^{2+}], which is slightly higher than in case of SIC-polyelectrolytes which obey L-type thresholds. Once the NaPSS is dissolved in 0.1 M NaCl the phase boundary is shifted by a factor of 4. The shift towards higher critical Ba^{2+}-values in 0.1 M NaCl can be explained by the increased exchange pressure at the residual groups exerted by the Na^+-cations. It was also observed for many other combinations like CaPMA, CaPA and AlPSS which exhibit an L-type phase boundary.

A significant extent of shrinking of the PSS coils was observed upon approaching the threshold lines via an increase of the Ba^{2+} concentration at [I]=0.1 M. While shrinking, the coils adopt structures close to deformed cylinders or irregular pearl necklaces based on aligned randomly, spaced nodules with a significant shape distribution. A transition to compact spheres by approaching the phase boundary could however not be observed for the PSS coils in the presence of Ba^{2+}-cations. Similar shapes were also observed for CuPA[14] and PbPA[15]. However by comparing BaPSS with AlPSS the total shrinking of the chains is stronger in case of BaPSS. The fact that the shrinking of the PSS chains is not as drastic as in case of the PA chains, may be explained by a premature competition with precipitation.

Whereas chains of CaPA, SrPA and AlPSS shrink with increasing temperature, the chains of BaPSS shrink with decreasing temperature, which indicates that the binding between the Ba^{2+}-cations and the PSS chains is an enthalpically driven process. Strikingly, these opposing trends open a new route to prepare block copolymer systems where one block of polyelectrolyte in the presence of Ba^{2+} decreases its dimensions in response to a temperature jump while the other block increases its dimensions. A similar type of mixed response has been published as schizophrenic systems.[100]

The relatively high threshold values of [Ba^{2+}] in the presence of inert salt and the concentration independent threshold lines are similar to H-type thresholds, which are established by Ikegami et al.[17] This raises the question about the nature of interactions of PSS with the Ba^{2+}-cation. Does $BaCl_2$ act as an inert salt, as SIC or as a salt in between? At least the values of the intercept and the lack of a slope of the threshold, give a hint, that the binding strength of the Ba^{2+}-cations to the residual groups is less pronounced than in case of AlPSS. However, the interactions cannot be merely of EIC-type as significant differences have been observed to the impact of Sr^{2+} and Ca^{2+}, which turned out to be of EIC-type. Neither of the two cations show a phase boundary as Ba^{2+} does. In line with this, shrinking experiments with Ca^{2+} cations did not show an effect on the PSS coils which goes significantly beyond that of Na^{+} cations, whilst Ba^{2+} generates an extra shrinking with partially collapsed domains. These findings are in full agreement with observations made by Tirrell et al. on the response of polyelectrolyte brushes with outer PSS layers to the addition of Mg^{2+}, Ca^{2+} or Ba^{2+} where the power to induce a shrinkage of the brush layer follows the trend $Mg^{2+} < Ca^{2+} < Ba^{2+}$.[101]

The aggregation trend of the BaPSS coils depends on the induction method. By using component mixing fluffy aggregates are formed right after mixing which become denser during the aggregation process. In case of temperature induced aggregation dense aggregates are created right from the beginning.

4.4 NaPA in the Presence of Ba^{2+} a SAXS Study

4.4.1 Phase Diagram at [I]=0.01 M

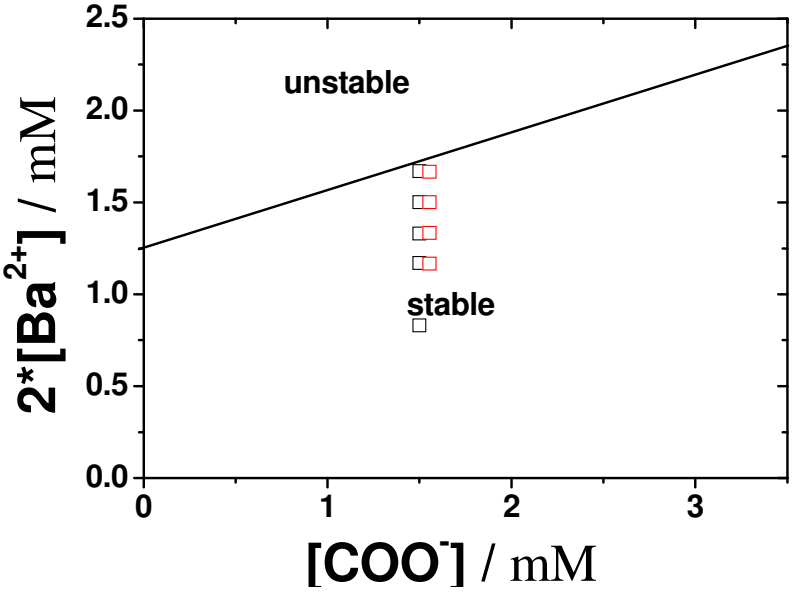

Figure 58: Phase diagram of polyacrylate in the presence of Ba^{2+}-cations at [I]=0.01 M.[13,24] Black open squares represent samples from series BaPA-ESRF measured by SAXS at ID02 in Grenoble indicating from bottom to top samples S5, S4, S3, S2 and S1. Red open squares represent samples from BaPA-MAX-lab-O and BaPA-MAX-lab-T measured at the I911-SAXS beamline in Lund indicating from bottom to top samples O- and T4, O- and T3, O- and T2 and O- and T1

The phase diagram of the BaPA system at [I]=0.01 was established by Schweins et al..[13,24] The phase boundary which separates the unstable regime at high Ba^{2+}-concentrations from the stable regime at low Ba^{2+}-concentrations exhibits a stoichiometric trend between Ba^{2+} and COO^-, which is typical for polyacrylates in the presence of alkaline earth cations[11–13], Cu^{2+} and Pb^{2+} (Figure 58)[14,15]. The slope of the phase boundary of NaPA in the presence of Ba^{2+} exhibits a value of m=0.160 at [I]=0.01 M NaCl. This is the smallest value, which was obtained for an alkaline earth cation-PA combination.[13] The value is also smaller than the slopes which were obtained from the different AlPSS phase diagrams (Tab. 18). Taking into account the valence of the cation, the value shows that in contrast to the AlPSS system at the phase boundary, only 1/3 of COO^- residues are neutralized by Ba^{2+}.

Schweins et al.[13] could also show by means of combined light scattering measurements, that the PA chains fully collapse while the Ba^{2+}-concentration is increased. The structure of the chains changes thereby from coils to compact spheres, which can be found at states close to the phase boundary. A further increase of the Ba^{2+}-concentration beyond the critical threshold value leads to aggregation and precipitation.[13,24]

4.4.2 Solution Behavior and SAXS Experiments

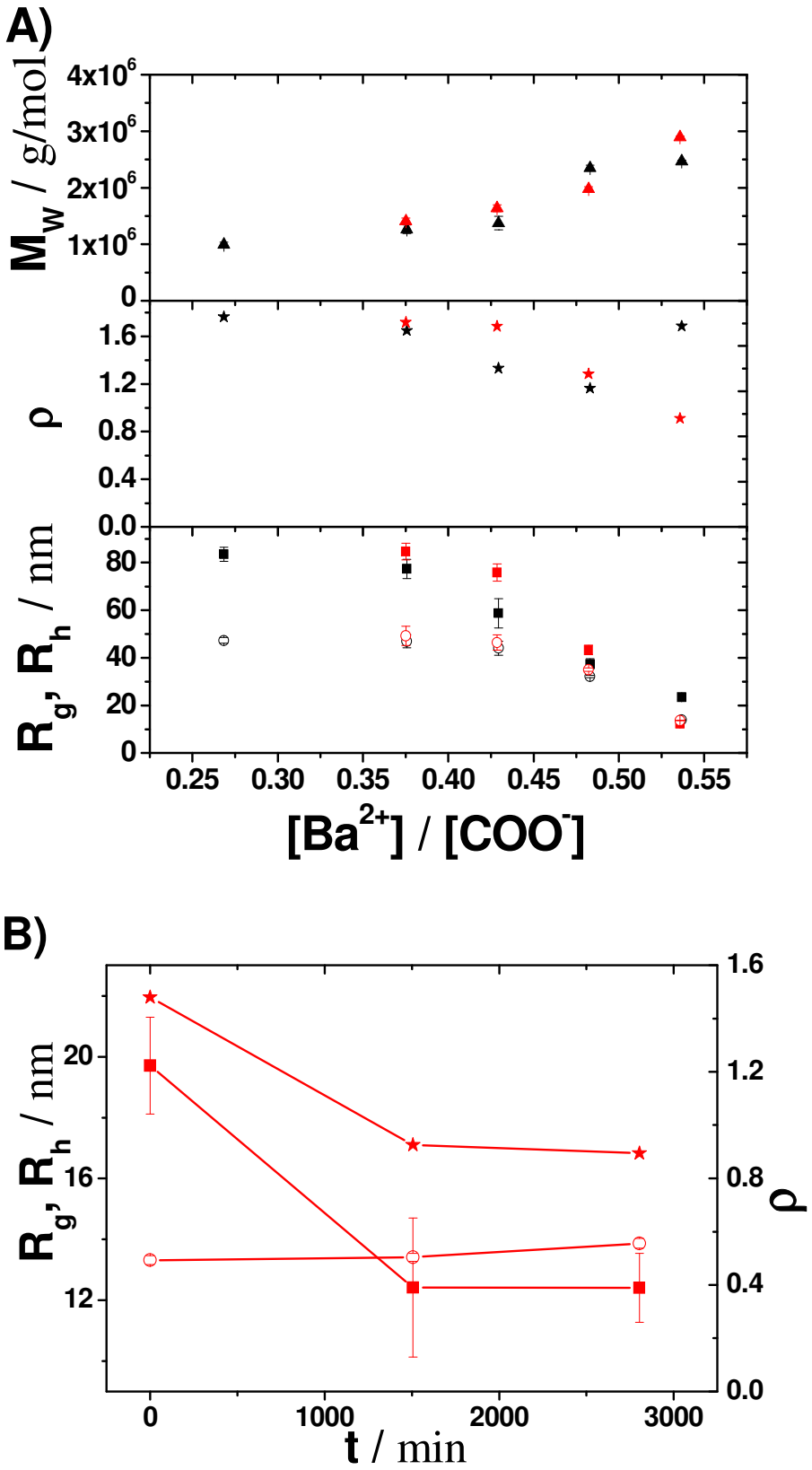

Figure 59: A) Values of R_g (■), R_h (○), M_w (▲) and ρ (★) of series BaPA-ESRF (black symbols) and series BaPA-MAX-lab-O (red symbols) at [I]=0.01. B) Values of R_g (■), R_h (○) and ρ (★) of sample O1 from series BaPA-MAX-lab-O as a function of time.

So far no small angle scattering experiments in the stable part of the phase diagram were performed with the BaPA system. In case of CaPA, SrPA and PbPA those measurements revealed intermediate structures in between the coil and sphere state, which could be fitted with a pearl necklace chain form factor.[15,25,27] Therefore we will now try to learn if similar structures can be found for BaPA.

The measurements were performed at the ID02 beamline located at the ESRF in Grenoble. Five suitable samples were mixed with the help of the BaPA phase diagram at [I]=0.01 with sample NaPA-1. All samples had the same NaPA concentration but differed in the Ba^{2+} and Na^{+} content (Fig. 58). The sample series denoted as BaPA-ESRF is represented by open black squares in the phase diagram (Fig. 58). The samples were characterized beforehand by SLS and DLS (Fig. 59 A black symbols). All light scattering curves were analyzed with the help of the Zimm equation[49] thereby neglecting the concentration dependent part in eq 12. As expected the value for R_g decreases with increasing Ba^{2+}-content from 83 to 23 nm. The same trend can be observed for the value of R_h which decreases from 47 to 14 nm. The value for the apparent M_w increases by a factor of 2.5 from ~ 1000 kDa to 2500 kDa. Possible explanations for this effect are the same which were already mentioned for AlPSS and BaPSS. The increase of the M_w could be affected by the decoration of the PA chains with Ba^{2+}-cations, which leads to an increase of the M_w of the whole ensemble and to a change of the dn/dc from NaPA towards BaPA. On the other hand a partial aggregation of a small portion of the NaPA chains due to an increased hydrophobicity cannot be excluded.

The structure sensitive parameter shrinks from 1.76 to 1.16 and increases for the sample with the highest Ba^{2+}-content again to a value of 1.68. Because of the location of this solution in the phase diagram a more collapsed structure and therefore a value close to ρ=0.78 was expected. The deviation from this expected value may be explained with the small size of the entities. For values for R_g close to and below 20 nm the slope in the scattering curve becomes very small and the experimental uncertainty for R_g becomes large.

After characterization by SLS and DLS the samples were send to Grenoble where they were measured 10 days after mixing by SAXS. The ID02 beamline has a detector tube with a length of 30 m which enables to measure at very low q-values (with that particular configuration down to 0.002 nm^{-1}). Unfortunately the scattering of the sample at low q-values was similar to the scattering of the pure solvent. Therefore only the mid-q range of 0.1 $nm^{-1} \leq q \leq 7$ nm^{-1} gave good scattering results (Fig. 60). By selection of an unsuitable detector distance a small shoulder in the scattering curve, which is typical for a pearl necklace chain and which defines the pearl-pearl distance may have been missed. However a drastic structural change of the PA chains with increasing Ba^{2+}-content can be observed. In the following the scattering curves will be discussed in terms of the slope in the Porod-regime.[68,71,72] The samples S5, S4 and S3, which contain the lowest Ba^{2+}-concentration show power laws of $P(q) \sim q^{-\beta}$ which exhibit a slope close to β=-1, which is typical for a cylinder-like structure. From sample S3 to S1, the slope increases from β=-1 to β=-2.2 and finally to β=-4. A slope of β=-2 is typical for a coil-like structure, while β=-4 is typical for a sphere.

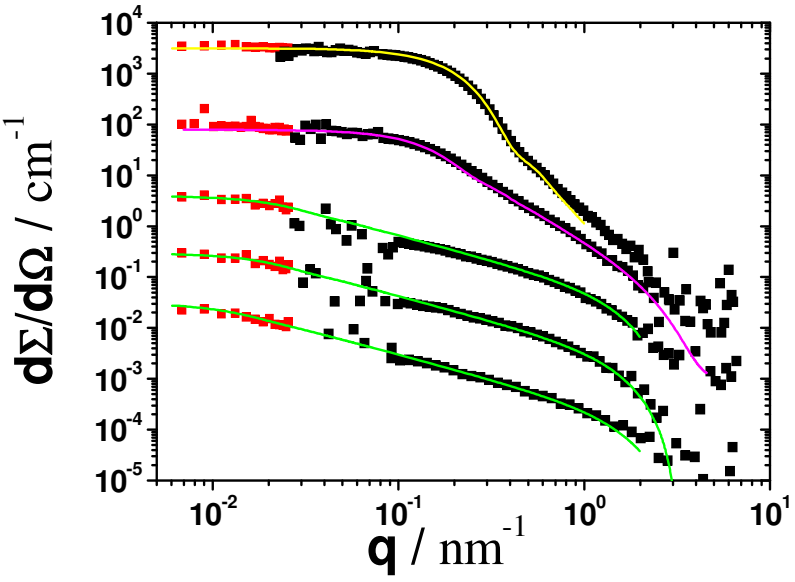

Figure 60: Combined SLS(■) and SAXS(■) scattering curves of sample series BaPA-ESRF from bottom to top with increasing content of Ba^{2+} in comparison to the corresponding cylinder model fit (green line)[50] , ellipsoid model fit (pink line)[76] and sphere model fit (yellow line)[50]. The respective fitting parameters are shown in Tab. 21, 22 and 23. The curves are increasingly shifted by a factor of 10^0, 10^1, 10^2, 10^3 and 10^4.

The change in the structure with increasing Ba^{2+}-concentration can also be observed in the Kratky-plot. For the samples S5 to S3, the signal in the Kratky-plot is steadily increasing and approaches a broad peak, which correlates with the cross section of the cylinders (Fig. 61 A). In case of sample S2 a small peak is already appearing. The position of the peak maximum is correlated with the size of the compact domain or sphere according to $q_{max}=2.5/R_{g,domain}$.[98] The peak maximum in S2 correlates with condensed domains of $R_{g,\ domain}$~12 nm, which is 3 times smaller than the size of the entire shrinking coil, determined as R_g~35 nm from SLS. This discrepancy is a hint that the PA-chain in that particular state could have adopted a pearl necklace-chain structure. The sample with the highest Ba^{2+}-content shows a large peak in the Kratky-plot corresponding to R_g of compact domains of 13.6 nm or to spheres with a radius of 11.3 nm, which is again smaller than the R_g, which was obtained from SLS. The Guinier analysis of the SAXS curve gives a value which is also much smaller than the R_g obtained from SLS. As it was mentioned before, the SLS measurement is not very accurate when small particles close to and below 20 nm are measured. However, the discrepancy between the value of R_g estimated by SLS and the values for R_g obtained by the Guinier and Peak analysis can also be attributed to a non-equilibrium state, which prevails for some time after mixing of the sample. In the following the equilibrium was achieved and the BaPA coils shrank to more compact states. This uncertainty in R_g does not offer conclusive information on the shape of S1 but the pattern of the bell-shape curve in the Kratky-plot and the first maximum which can be seen in the scattering curve of sample S1 is a hint that the chains collapsed at that state to compact spheres (Fig. 60). Therefore the scattering curve of sample S1 was fitted with the model curve of a sphere[50] (Fig. 60 and Tab. 21).

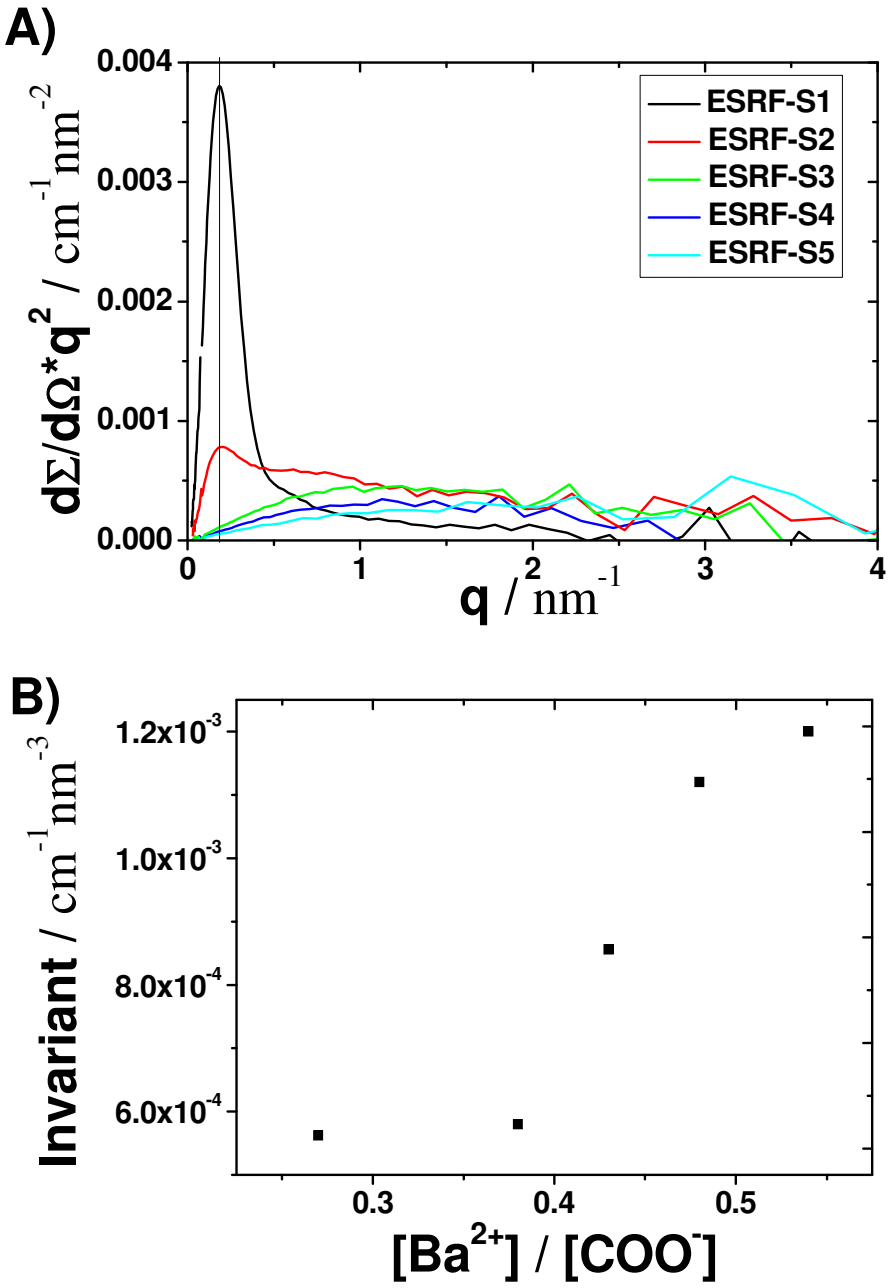

Figure 61: A) Kratky-plot of SAXS measurements of series BaPA-ESRF with the following color code: light blue – S5, dark blue – S4, green – S3, red – S2 and black S1. B) Invariant of 61 A as a function of the $[Ba^{2+}]/[COO^{-}]$ ratio. The area was calculated in a q-regime of 0.08 nm-1 ≤ q ≤ 2.3.

The invariant, which is the area under the scattering curve in the Kratky-plot was estimated in a q regime from 0.08 nm^{-1} to 2.3 nm^{-1} (Fig. 61 B). The invariant increased by a factor of 2.1 from 5.62∗10-4 $cm^{-1}nm^{-3}$ to 1.20∗10-3 $cm^{-1}nm^{-3}$ in the series from the sample with the lowest Ba^{2+}-content to the sample with the highest Ba^{2+}-content. The increase can be explained by the incorporation of the Ba^{2+}-cations into the PSS coils, which increases the scattering contrast of the whole entity.

Table 21: Fit Parameters of sample S1 fitted with the model form factor of a sphere.[50]

Sample	R_g Guinier (SLS) / nm	R_g Guinier (SAXS) / nm	R_g from peak in Kratky plot	Radius sphere (model form factor) / nm
S1	22.80	9.6	13.3	9

The scattering curve of S2 was fitted with an ellipsoid model. Although the overall trend of the curve is recovered by the fit for sample S2 (Fig. 60), the R_g which can be obtained from the fitting parameters is too low compared to the R_g measured by SLS (Tab. 22). Like in case of BaPSS it is possible that the structure of S2 could be more cigar like or is composed of dense domains, which touch each other. In such a case the scattering curve would not follow the model curve of a pearl necklace chain, but the compact domains, which were identified by the Kratky-plot would be reconciled with nodules or the cross section of the cigar.

Table 22: Fitting parameters of sample S2 fitted with the model form factor of a ellipsoid.[76]

sample	Ellipsoid radius a / nm	Ellipsoid radius b / nm	R_g from fitting parameters / nm	R_g from Peak in Kratky plot / nm	R_g Guinier (SAXS) / nm	R_g Guinier (SLS) / nm
S2	0.9	18	9.4	12	11.6	34.9

The samples S3, S4 and S5 were fitted with a cylinder model[50]. First the respective SAXS curve was fitted with the model curve, thereby the radius of the cylinder was determined. Afterwards the length of the model cylinder was varied until the R_g calculated from the fitting parameters overlaid with the R_g which was obtained by the SLS measurements. The SLS curves were then multiplied with an appropriate shift factor in a way that the SLS curve overlaid with the respective model curve of the cylinder. The main fitting parameters are shown in Tab. 23.

Table 23: Fit parameters of samples S3, S4 and S5 fitted with the model form factor of a cylinder.[50]

Sample	Cylinder length / nm	Cylinder radius / nm	R_g from fitting parameters / nm	R_g Guinier (SLS) / nm
S3	181.9	1.2	52.5	49.7
S4	211.8	1.2	61.4	61.2
S5	304.3	1	87.8	86.6

Since the time delay between the mixing of the samples and the measurements at the ID02 in Grenoble was 10 days long, another SAXS experiment at the same system was done, now

using polymer sample NaPA-2 instead of sample NaPA-1. This further SAXS experiment is expected to answer the question, if the age of the samples has an effect on the structure of the collapsed chains.

Four samples were mixed (O1, O2, O3, O4) which had almost the same composition as the four samples with the highest Ba^{2+}-content used for the experiment at the ESRF (Fig. 58). The sample series is denoted as BaPA-MAX-lab-O. After mixing, the samples were characterized by DLS and SLS three times in a period of two days. SLS was analyzed with the Zimm equation[49], where the concentration dependent part was neglected (eq 12). Although another NaPA sample was used for the experiment, almost the same extent of shrinking was observed compared to the sample characterization of series BaPA-ESRF. In series BaPA-MAX-lab-O the value for R_g was shrinking with increasing Ba^{2+}-content from 85 nm to 12 nm while the value of R_h decreased from 50 nm to 13 nm. The structure sensitive parameter decreased with increasing Ba^{2+}-content from 1.7 to 0.9 and M_w increased from 1400 kDa to 2900 kDa (Fig. 59 A).

An interesting effect could be extracted additionally from the light scattering experiments. The sample O1 with the highest Ba^{2+}-content in series of BaPA-MAX-lab-O showed the same unexpected behavior as sample S1 in series BaPA-ESRF (Fig. 59 B). Directly after the mixing of O1 the obtained R_g also adopted a value of ~20 nm while the R_h had a value of ~13.5, which leads to a structure sensitive parameter of ρ~1.5, although a much more compact structure was expected at a state that close to the phase boundary. Interestingly enough the value of R_g of sample O1 further shrank successively from ~20 to ~12.4 nm in the period between SLS/DLS measurement 1 and 2 (25 hours) while the value of R_h stayed stable. The second value for the structure sensitive parameter was 0.9, which fits nicely to the findings of Schweins et al.[13,24] and to the findings of the SAXS measurements of series BaPA-ESRF. The time dependent development of sample O1 suggests that for SAS experiments in the future a certain shelf time for the equilibration of the samples should be applied.

After 2 days, the samples were sent to the MAX-lab in Lund (Sweden) where they were measured 10 days after mixing by SAXS at the I911-SAXS beamline. Additionally 4 samples (T1, T2, T3, T4) were measured, which had the same composition like the samples of series BaPA-MAX-lab-O, but which were prepared directly before the SAXS measurement by mixing a NaPA-stock solution of polymer sample NaPA-2 with different $BaCl_2$-stock solutions. The sample series is denoted in the following as BaPA-MAX-lab-T.

By comparing the set of scattering curves of sample series BaPA-MAX-lab-O and BaPA-MAX-lab-T similarities and differences were observed (Figure 62 A and B). In general both sample series follow the trend which was already observed for series BaPA-ESRF. The polymer chains become more compact with increasing Ba^{2+}-content, which can be observed from the scattering curves and the Kratky-plots (Fig. 62 A, B, C and D). However, small differences were also observed and can be discussed better by comparing the scattering curves with the same sample composition.

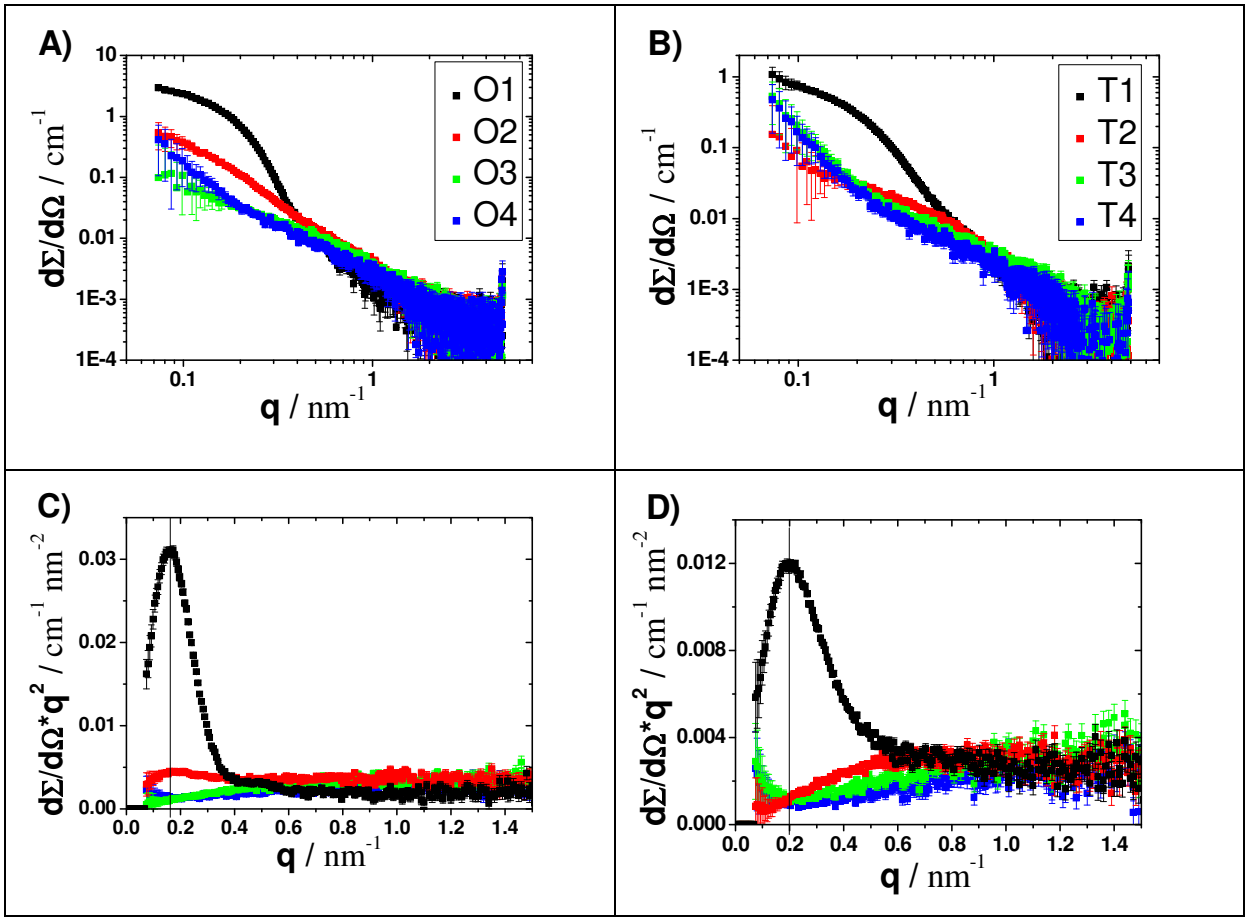

Figure 62: A) SAXS curves of sample series BaPA-MAX-lab-O. B) SAXS curves of sample series BaPA-MAX-lab-T. C) Kratky-plot of sample series BaPA-MAX-lab-O. D) Kratky-plot of sample series BaPA-MAX-lab-T.

Like sample S1 from series BaPA-ESRF, sample O1 has a sphere-like structure. The scattering curve has a slope close to β=-4 at high q. Because of the missing Guinier regime, sample O1 and T1 could not be fitted with a Guinier model, therefore R_g was calculated from the respective peak positions in the Kratky plot. The R_g obtained from the peak position of the Kratky-Plot of sample S1 has a value of ~12.8 nm and fits perfectly to the second value which was determined by SLS. It was shown before that the SLS/DLS measurements predicted also a sphere like structure. The scattering curve of sample T1 exhibits a slope of -3 and the first maxima of the sphere form factor cannot be observed in the scattering curve. The peak position in the Kratky curve corresponds in case of sample T1 to a sphere of 10.4 nm or to condensed domains of the size of 12.5 nm. Sample T1 was mixed directly in front of the SAXS experiment. Hence, it is assumed that sample T1 was not yet in equilibrium, when it was measured by SAXS. The polymer chains became already compact but not compact enough to form perfect sphere-like structures.

The scattering curve of sample O2 exhibits a slope of β=-2 in the Porod regime, which is comparable to the value obtained from the scattering curve of S2 (Fig. 63 B and Fig. 60). As it was mentioned before, this is a typical value for coil-like structures. Like for sample S2 from series BaPA-ESRF a small peak can be found in the Kratky-plot of sample O2. In case of sample O2 this peak is not as distinct and extends over a larger q range than in case of sample S2 (Fig. 62 C). The condensed areas of the chain exhibit a R_g of ~14 nm, which is three

times smaller than the R_g of ~43 nm measured by SLS. In both cases no shoulder in the scattering curve which is related to the distance of the collapsed domains could be found. The freshly mixed sample T2 shows a completely different behavior than O2 and S2. The slope of the scattering curve in the mid-q region shows a slope of β=-1. Towards small q-values a strong increase of the scattering intensity is visible (B in Fig. 62 and B in Fig. 63). Due to the large uncertainty of the data points it is not clear if this increase in the scattering intensity has a structural meaning. Accordingly the peak which was typical for S2 and O2 does not appear in the Kratky-plot (Fig. 62 D). Also in that case it can be supposed that the time between mixing of sample T2 and the SAXS measurement was not long enough, to reach the equilibrium.

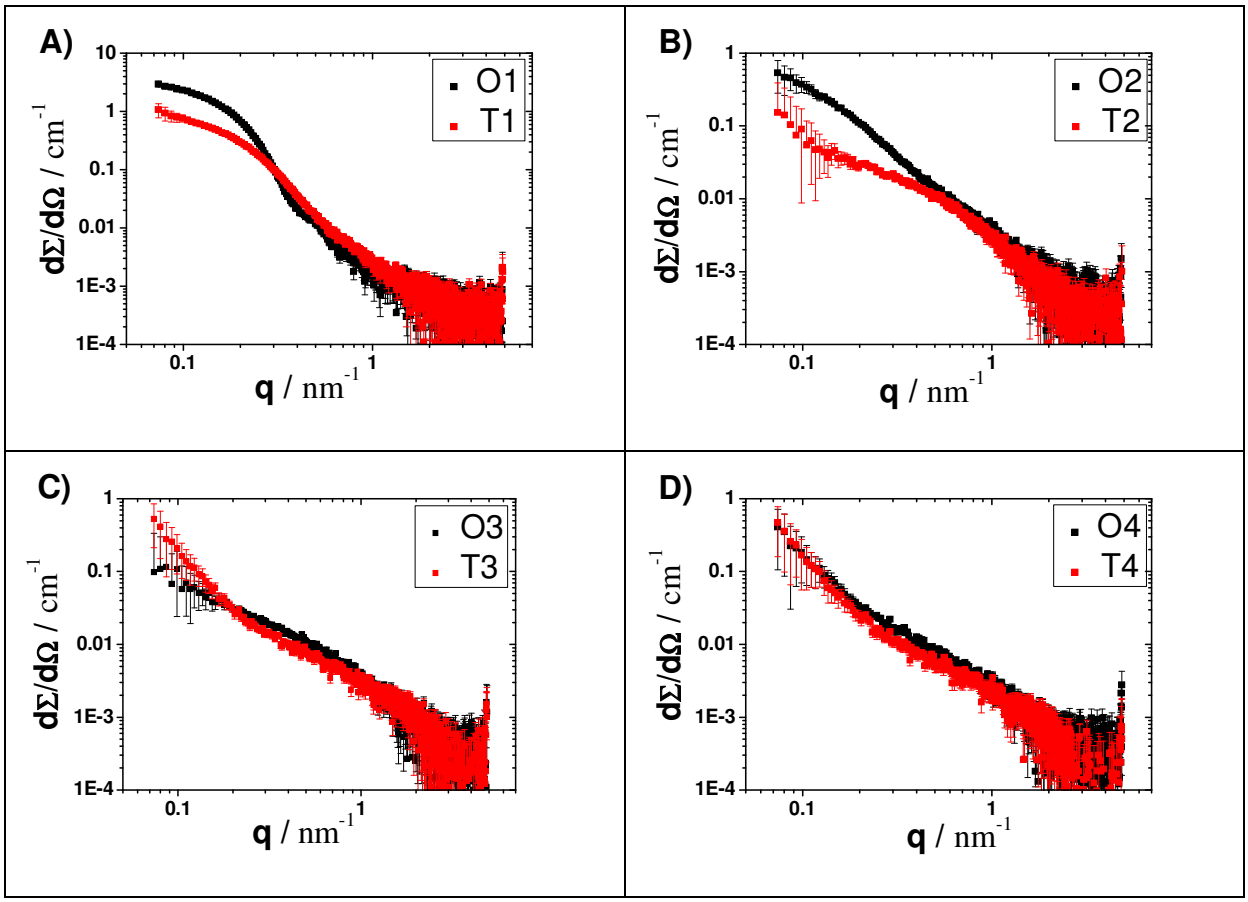

Figure 63: A) Comparison of O1 and T1. B) Comparison of O2 and T2. C) Comparison of O3 and T3. D) Comparison of O4 and T4.

Like the scattering curves of S3 and S4, the scattering curves of samples O3, T3, O4 and T4 exhibit a slope of -1 in the Porod-regime. The upturn of the scattering signal at low q in sample T3, O4 and T4 may be attributed to formation of aggregates, but due to the large uncertainty of the points it is not clear if the upturn of the scattering signal has a structural meaning.

4.4.3 Summary

The SAXS study of polyacrylate in the presence of Ba^{2+}-cations showed that the polyacrylate chains collapse with increasing Ba^{2+}-content from cylinder-like structures towards compact spheres. The collapse towards compact spheres was already noticed before by Schweins et

al.[24,27] by means of combined SLS/DLS, but a more direct proof for this observation was still missing. A pearl necklace chain structure for intermediate states as have been observed for CaPA[25], SrPA[27] and PbPA[15] could not be verified. However, there are hints that an intermediate structure which is composed of connected, condensed sub-domains also exist for those present states which are located close to but not directly at the phase boundary.

Some similarities can be observed to PSS in the presence of Ba^{2+}. In line with the shrinking the appearance of compact domains were observed. Another similarity is an elongated time of shrinking of the samples which are located very close to the phase boundary. The final size of the PE chains is not reached before 12h of equilibration. Differences can be observed in the degree of shrinking, which is more distinct in case of BaPA. For BaPA a collapse from coils to compact spheres can be observed, whereby the BaPSS chains shrink from coils to pearl-necklace or potatoe-like structures (chapter 4.3.1).

For future SAS experiments a certain shelf time of the samples should be considered before SAS measurements are started in order to measure final states.

4.5 ITC on Various SIC-Polyelectrolyte Combinations

4.5.1 Introduction

In two preceding chapters on the solution behavior of AlPSS and BaPSS it could be shown by means of temperature dependent light scattering experiments that the size of the AlPSS and BaPSS chains correlate directly with the solution temperature [Chapter 4.2.2 and 4.3.2]. In case of NaPSS in the presence of Al^{3+}-cations, the chains begin to shrink with increasing temperature [Chapter 4.2.2]. The same effect could be induced by the binding of specifically interacting alkaline earth cations to NaPA.[30] Obviously the binding of the respective cations to the ionic groups of those polyelectrolytes is entropically driven. Noteworthy combinations of SICs and polyelectrolytes also showed an L-type precipitation behavior. Antonietti et al.[29] investigated NaPA in the presence of Ca^{2+}-cations by means of ITC measurements. They observed a positive molar binding enthalpy which for the first titration increment (i=1) is ΔH_{Ca1}=17 kJ/mol. This indicates an entropically driven binding process, in agreement with the temperature induced coil shrinking of alkaline earth salts of PA. Qualitative calculation revealed that ten water molecules and two Na-cations are liberated per Ca^{2+}-cation bound to COO^-.[29]

In case of BaPSS the opposite trend was observed. By cooling the solution, the coils begin to shrink. The trends can be reversed by increasing the temperature. Accordingly, the binding process of the Ba^{2+} cations to the sulfonated groups seems to be enthalpically driven [Chapter 4.3.2].

Motivated by these findings isothermal titration calorimetry measurements were carried out on PA in combination with Ca^{2+} and Ba^{2+} and on PSS in combination with Ca^{2+}, Ba^{2+} and Al^{3+} to unravel the thermodynamics of the binding process of the respective SIC to the functional residues of the polyelectrolyte chains.

The required data provide three characteristic parameters, the molar binding energy determined from the second titration step normalized by a division with the molar amount of SICs added by this step (ΔH_{M2}), the total integral done by the stepwise addition of the heat increments and the total integral normalized by the molar monomer concentration (X^-).

4.5.2 Results

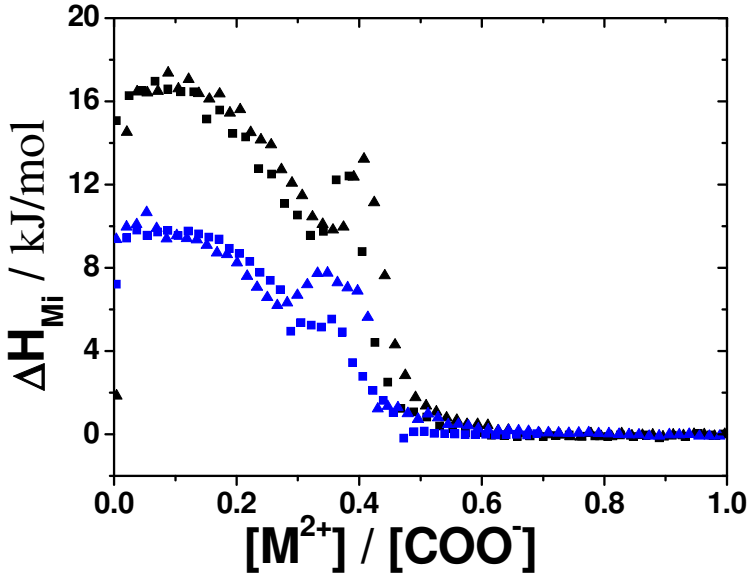

Figure 64: ITC curves for the titration of a solution of NaPA with a solution of $CaCl_2$ (CaPA-1 ■, CaPA-2 ▲) and $BaCl_2$ (BaPA-1 ■, BaPA-2 ▲) in pure water.

The ITC measurements on the interaction of Ca^{2+} and Ba^{2+} with PA show a positive binding enthalpy (Fig. 64). The maximum molar binding enthalpy for the titration of NaPA with Ca^{2+} measured at the beginning of an experiment (i=2) with 16.27 kJ/mol ≤ ΔH_{Ca2} ≤ 16.45 kJ/mol is comparable to the values published by Antonietti et al.[29] for PA in the presence of Ca^{2+}. The maximum molar binding enthalpy of PA in the presence of Ba^{2+} adopted smaller values with 9.43 kJ/mol ≤ ΔH_{Ba2} ≤ 9.98 kJ/mol. The corresponding integrated enthalpy per residual group for PA in the presence of Ca^{2+} is 5.77 kJ/mol ≤ ΔH_{x-} ≤ 6.31 kJ/mol and is also higher compared to the one for PA in the presence of Ba^{2+} which is 3.15 kJ/mol ≤ ΔH_{x-} ≤ 3.53 kJ/mol. Hence, the binding process in both cases is endothermic and the process has to be entropically driven.

In both cases a spike-like peak is visible at $[M^{z+}]/[COO^-]$ ~ 0.35. During the experiments the phase boundary was crossed, because precipitate could be observed in both cases on the bottom of the sample container after the ITC experiment. Turbidity experiments showed that the precipitation of the CaPA and BaPA sets in directly after the peak (Fig. 65 A and B). Therefore the peak is probably connected with the aggregation and/or precipitation process of CaPA and BaPA. Noteworthy Antonietti et al. did not observe such a peak. The reason could be that Antonietti et al.[29] stopped the experiments before the precipitation of the CaPA started.

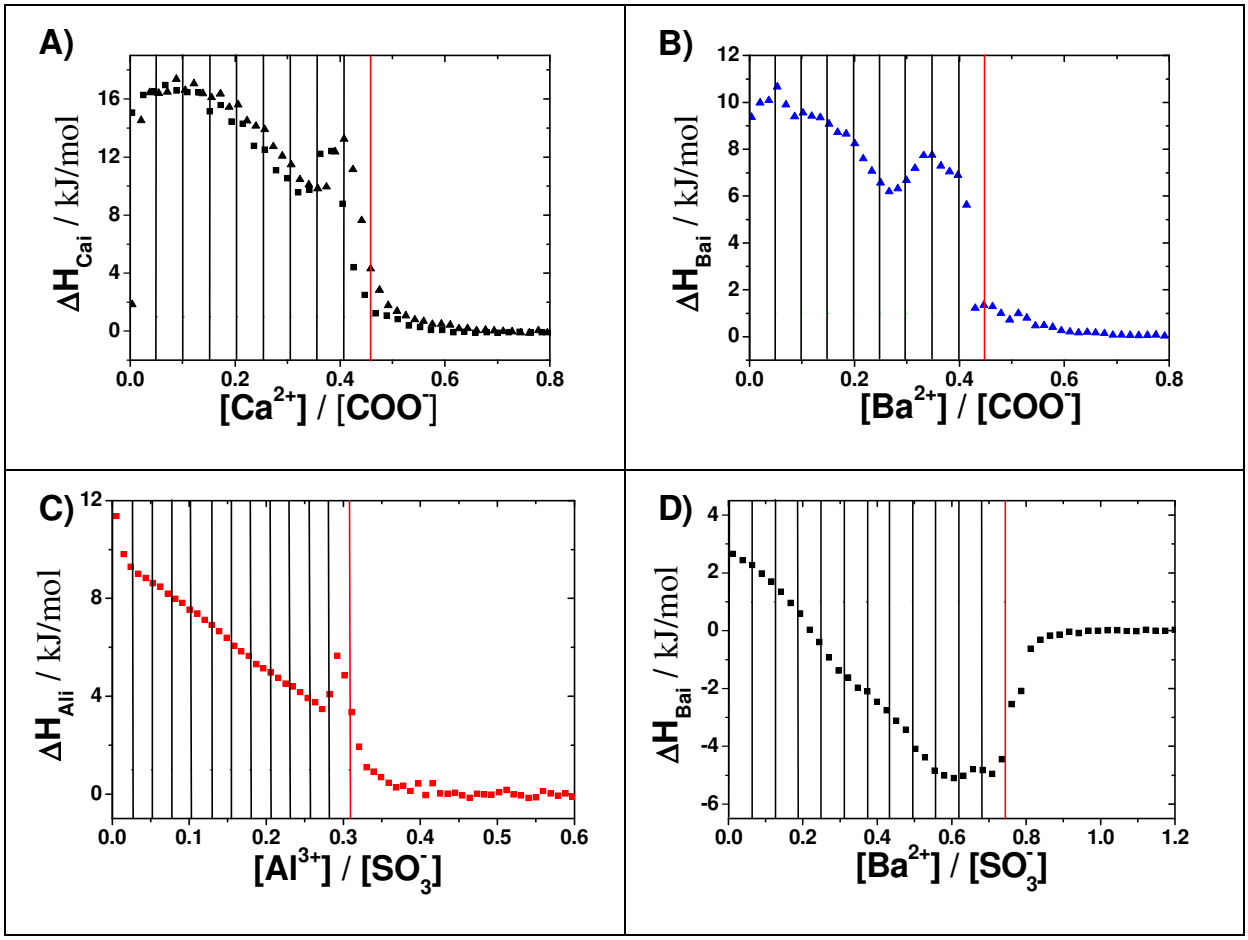

Figure 65: ITC measurements in comparison with the respective turbidity experiments. Black lines denote compositions which are stable and optically clear. Red lines indicate the compositions which are optically turbid. The graphs refer to the repetitions of the following experiments: CaPA-1 and CaPA-2 (A), BaPA-2 (B), and AlPSS-pH6-1 (C) and BaPSS-1 (D). The symbols have the same meaning as in the corresponding Figures of the manuscript.

Experiments on the interaction of Al^{3+} with PSS were carried out at three different conditions. Two experiments were performed with a non adjusted pH of the NaPSS solution (pH 6), two with a pH of the NaPSS solution adjusted at pH=3 and two experiments with a pH of the NaPSS solution adjusted to pH=3 at [I]=0.1 M. Experiments at a pH of 3 were carried out, because the $AlCl_3$ stock solutions exhibit a pH of 3. The pH of NaPSS solutions usually exhibits a value of 6 and hence does not require adjustment to higher pH to ensure a fully dissociated state. The pKs-value of para-toluenesulfonicacid is 0.7,[102] which is comparable to the pKs-value of the sulfuric acid and thus indicates that PSS is completely dissociated in aqueous solutions.

The ITC curves of the experiments with NaPSS dissolved in pure water at a pH of 3 and of 6, show comparable trends (Fig. 66). The plateau in the beginning, which could be observed in the experiments with PA and Ba^{2+} and Ca^{2+} is missing in case of PSS and Al^{3+} at pH=3 and 6. All curves decrease from the start. Titration of PSS with Al^{3+} shows an endothermic molar binding enthalpy and a spike-like peak could be observed in the decreasing part of the ITC curves at both pH-values of PSS in the presence of Al^{3+}. Turbidity experiments showed again that the precipitation of the AlPSS sets in right after the peak in ΔH_{Ali} appeared (Fig. 66 C). At the end of the experiments an oil-like precipitate was found on the bottom of the sample

container. Hence, the solution behavior of PSS in the presence of Al^{3+} at pH=6 and pH=3 is close to that of PA in the presence of Ca^{2+} and Ba^{2+}. The molar binding enthalpy at the second titration step exhibits in both cases a value in between 9.32 kJ/mol ≤ ΔH_{Al2} ≤ 10.45 kJ/mol, which is comparable to the values obtained for PA in the presence of Ba^{2+}. The values for the experiments done with the NaPSS solution adjusted to a pH of 3 are shifted to negligibly lower values of $[Al^{3+}]/[SO_3^-]$ compared to those observed at pH=6. The total integral normalized by the amount of monomers also differs slightly. It adopts in case of pH=3 values of ΔH_{x-}=1.67 kJ/mol and in case of pH=6 values of 2.03 kJ/mol ≤ ΔH_{x-} ≤ 2.32 kJ/mol. The small differences could be explained by an exchange pressure caused by the additional H^+-cations. However the effect is very small and it is suggested that the influence of the pH value in the range of 3 ≤ pH ≤ 6 on the behavior of NaPSS coils in aqueous solutions is very low.

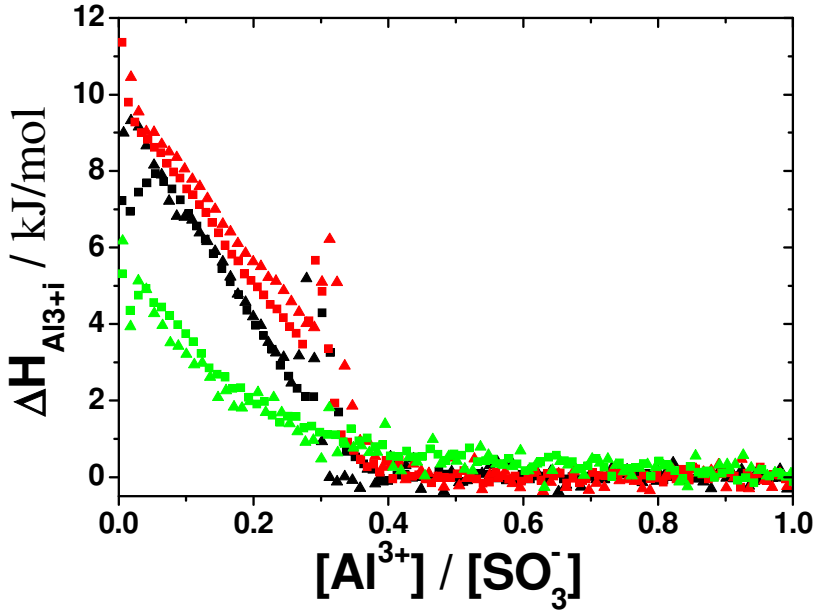

Figure 66: ITC curves for the titration of a solution of NaPSS with a solution of $AlCl_3$ in pure water at pH=3 (AlPSS-pH3-1 ■, AlPSS-pH3-3 ▲) and pH=6 (AlPSS-pH6-1 ■, AlPSS-pH6-2 ▲) and at [I]=0.1 M and pH=3 (AlPSS-NaCl-pH3-1 ■, AlPSS-NaCl-pH3-2 ▲).

The ITC curve for the titration of NaPSS with Al^{3+} at [I]=0.1 M shows a deviation from the experiments performed without inert salt (Fig. 66). The molar binding enthalpy of the initial titration increment is positive at 4.75 kJ/mol ≤ ΔH_{Al3} ≤ 5.13 kJ/mol, while the total heat per mol of monomers is 1.07 kJ/mol ≤ ΔH_{x-} ≤ 1.15 kJ/mol. Both values are 50% lower than the ones observed in the absence of inert salt. This decrease can be explained with the exchange pressure caused by the Na^+-cations. As can be inferred from Fig. 65, the binding process also extends over a broader regime of $[Al^{3+}]/[SO_3^-]$. The spike-like peak which was found in the titration curve of PA with $Ca^{2+}$and Ba^{2+} and the titration curve of PSS with Al^{3+} in the absence of an inert salt content, disappeared once NaCl is present at [I]=0.1 M. A precipitate could not be found on the bottom of the sample chamber.

PSS in the presence of Ba^{2+} was investigated in pure water and at [I]=0.1 M. The ITC curve of PSS in the presence of Ba^{2+} in pure water differs completely from PSS in the presence of Al^{3+} in pure water (Fig. 66 and Fig. 67). It starts with an endothermic value at 2.43 kJ/mol ≤ ΔH_{Ba2} ≤ 3.15 kJ/mol and becomes gradually exothermic to a level of -4 kJ/mol ≤ ΔH_{Bai} ≤ -5.5 kJ/mol. The ΔH_{Bai} value then decreases until a small peak appears, beyond which it drops to the baseline. The ΔH_{X-} adopts values between -1.49 kJ/mol and -1.58 kJ/mol. This exothermic binding enthalpy is compatible with the temperature dependent light scattering experiments, where a decreasing sample temperature leads to stronger binding of Ba^{2+} and hence to a coil shrinking [Chapter 4.3.2]. The total integral of the ITC curve can be separated into a positive part 0.095 J ≤ Integral ≤ 0.182 J and a negative part -0.410 J ≤ Integral ≤ -0.770 J.

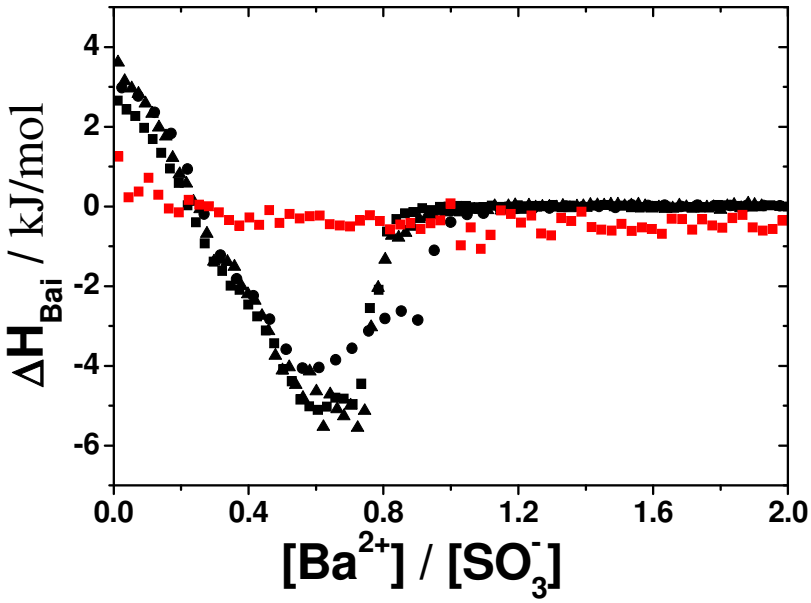

Figure 67: ITC curves for the titration of a solution of NaPSS with a solution of Ba^{2+} in pure water (BaPSS-1 ■, BaPSS-2 ▲,BaPSS-3 ●) and 0.1 M (BaPSS-NaCl-1 ■).

An endothermic process at the beginning of the titration turns into a significantly stronger exothermic process at around $[Ba^{2+}]/[SO_3^-]$ ~ 0.3. This pattern of the ITC curve can be explained with two different processes which overlay each other. Whereas the initial value of ΔH_{Ba1} of 3kJ/mol is in qualitative agreement with a replacement of two Na^+ by one Ba^{2+} ($\Delta H_{Ba1,theoretical}$=3.718 kJ/mol). The second step could be attributed to the binding of the Ba^{2+}-cations to the residual groups of the NaPSS coils. Hence, penetration of bivalent Ba^{2+} cations into the domains of NaPSS coils accompanied with the liberation of the corresponding amount of Na^+ ions is the dominating process during the first titration steps. Only after accumulation of Ba^{2+} in those domains has become large enough binding of Ba^{2+} to SO_3^-, accompanied with the evolution of heat gets increasingly dominating. The negative enthalpy of the second process is fully in line with the temperature dependent SLS/DLS experiments, where a decreasing sample temperature revealed a coil shrinking (Fig. 4.3.2).

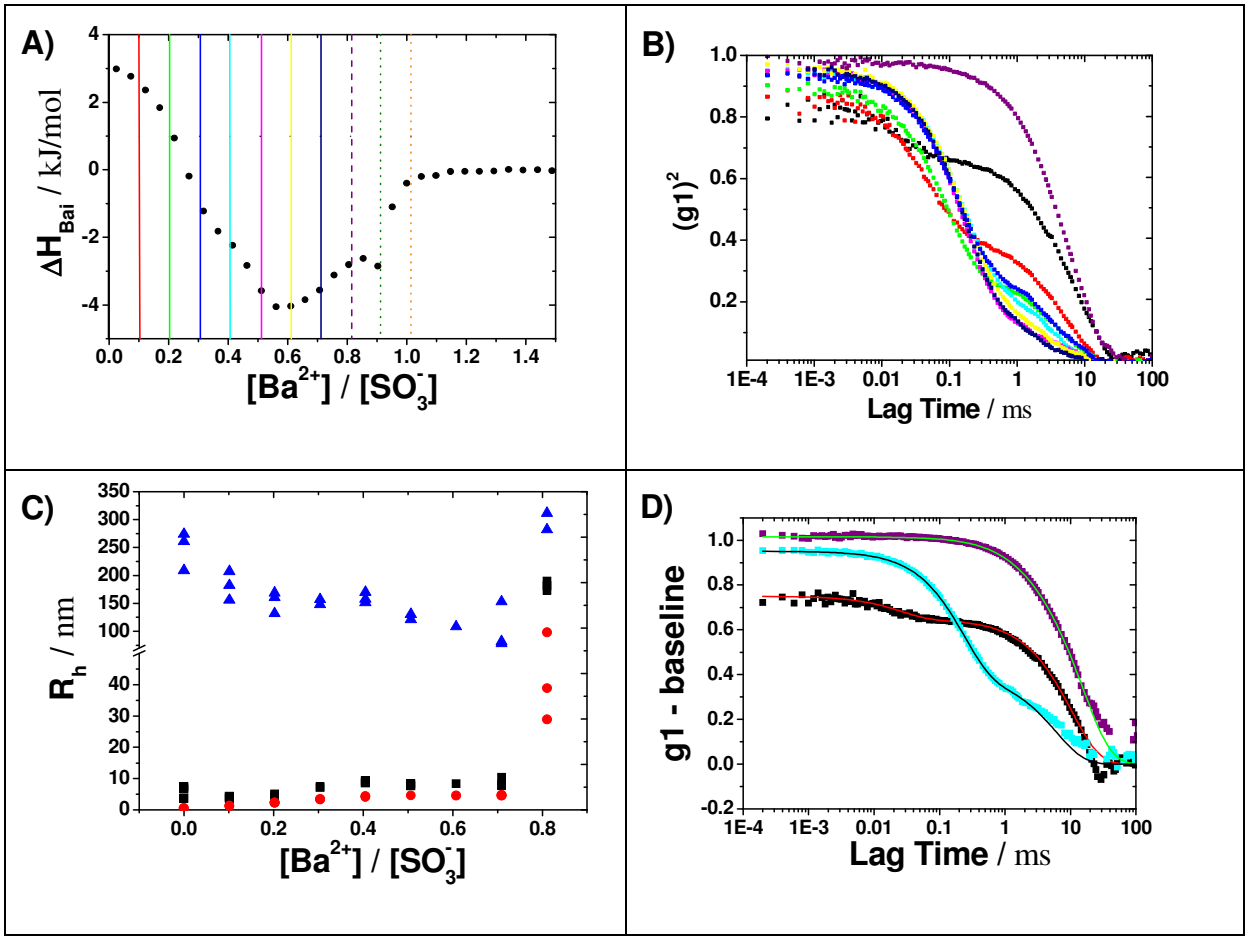

Figure 68: A) ITC curve of BaPSS. Coloured lines represent compositions which were additionally analyzed by DLS. B) Correlation functions measured at a scattering angle of 40° of the different states addressed by ITC in A). The colour code in B) is equal to the one in A). C) Results of a biexponential fit of the correlation functions in function of the sample composition with R_h 1 (●), R_h 2 (▲) and averaged R_h (■). D) Selected correlation functions with corresponding biexponential fit.

Additional DLS measurements were performed with the same protocol applied for the ITC experiment BaPSS-3 where NaPSS was titrated with Ba^{2+} in pure water. The DLS experiments in the beginning show two modes, a fast mode and a slow mode. With increasing Ba^{2+} content the slow mode gradually weakens until a point close to the spike-like peak at $0.7 \leq [Ba^{2+}]/[SO_3^-] \leq 1$, where it disappears and just one intensive slow mode is observed (Fig. 68). The fast mode can be interpreted as the signal from single coils, while the slow mode can be attributed to aggregates. During the initial part of the titration, i.e. at low concentrations of Ba^{2+} these aggregates dissolve because of the incoming Ba^{2+}-cations. On one hand the Ba^{2+}-cations bind to the sulfonate groups of the NaPSS coils, neutralize the polyelectrolyte and lead to an increasing hydrophobicity and coil contraction. On the other hand the Ba^{2+}-cations contribute to an electrostatic shielding effect. Both effects, neutralization and electrostatic shielding weaken like-charge attractions among polyelectrolyte chains observed at very low salt concentrations.[103–105] Accordingly NaPSS coils become separated from each other and the tendency to form aggregates decreases with increasing Ba^{2+} content. At a critical concentration of the Ba^{2+}-cations finally starts aggregation and precipitation of the hydrophobic NaPSS coils. The turbidity experiments showed that the precipitation of the

BaPSS starts right after the spike-like peak in the ITC curve like in the case of PSS in the presence of Al^{3+} (Fig. 65 D).

It is more difficult to obtain significant data from the ITC experiments of NaPSS solutions with Ba^{2+} at [I]=0.1 M. A titration based on the same protocol as in pure water (BaPSS-NaCl-1) started again with positive enthalpy values, which became slightly negative (Fig. 67). A subtraction of the fitted background was not possible, because the precipitation threshold was not reached at the end of the experiment. A closer look on the phase diagram offers a straight forward explanation. The Ba^{2+}-content necessary to precipitate chains in the NaPSS-solution under consideration is much higher than the value of 16.5 mM which was reached at the end of the ITC experiments of NaPSS solutions with Ba^{2+} at [I]=0.1 M. At the same time the Ba^{2+}-concentration in the stock solution must not be increased over 0.05 M, because the content of positive charges should be equal to $[I]=2[Ba^{2+}]+[Na^{+}]=0.1$ M at every titration step. The biggest syringe available had a volume of 2.5 ml. Even if the starting volume of the NaPSS solution in the sample container would have been decreased drastically from 9.5 ml to 5 ml, it would not have been low enough to make accessible the precipitation threshold.

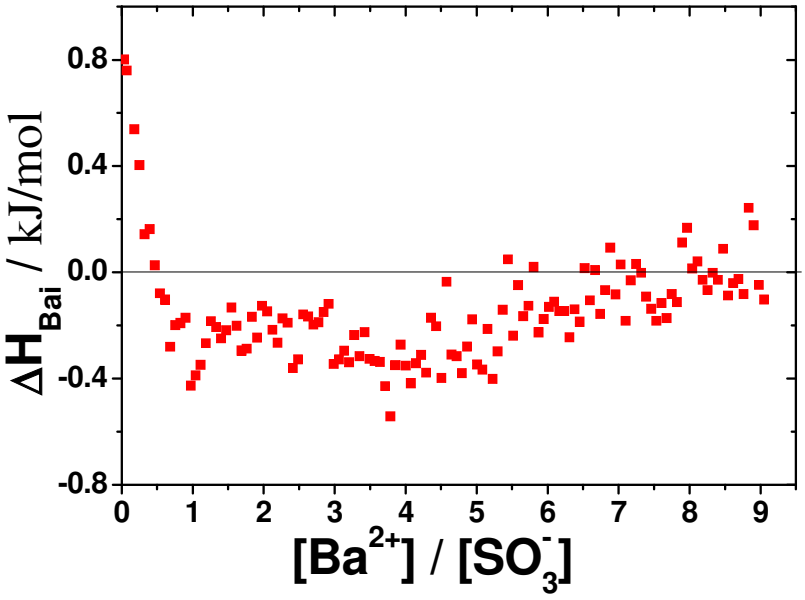

Figure 69: ITC curves for the titration of a solution of NaPSS with a solution of Ba^{2+} approaching [I]=0.1 M at the end of the titration experiment. The experiment is denoted as BaPSS-NaCl-option.

Therefore an alternative experiment was designed. The starting solution of PSS had a NaCl concentration of 0.06 M and the Ba^{2+}-solution with which we titrated had a concentration of $[Ba^{2+}]=0.118$ M. This composition made possible that the salinity of the solution approaches $[I]=2[Ba^{2+}] + [Na^{+}]=0.1$ M after the last titration step. With this method a fitted background could be subtracted from the ITC curve. The resulting ITC curve starts again with an endothermic part at $\Delta H_{Ba2}=0.76$ kJ/mol, successively drops to slightly exothermic values and eventually approaches the baseline (Fig. 69). The total integral normalized to the monomer concentration adopts a value of $\Delta H_{x}=-1.385$ kJ/mol. After the experiment a precipitate was observed in the sample container. Hence, the ITC curve now shows the same pattern, which

has been observed for the titration of PSS with Ba^{2+} in the absence of an inert salt. Only the exothermic peak extends over a wider regime of $[Ba^{2+}]/[SO_3^-]$. Also the influence of the inert salt content is the same observed for the titration of PSS with Al^{3+} experiments. For both PE-SIC combinations the ΔH_{Mi} values and ΔH_{x-} values are shifted to slightly lower values compared to the experiments, which were performed in the absence of an inert salt (Tab. 24).

Two additional ITC experiments were carried out in which PSS dissolved in pure water was titrated with Ca^{2+}. The signal of the ITC curves shows an endothermic process starting at 4.35 kJ/mol ≤ ΔH_{Cai} ≤ 4.59 kJ/mol and continuously decreases to the baseline, which is reached at a Ca^{2+} to monomer ratio of 0.5.

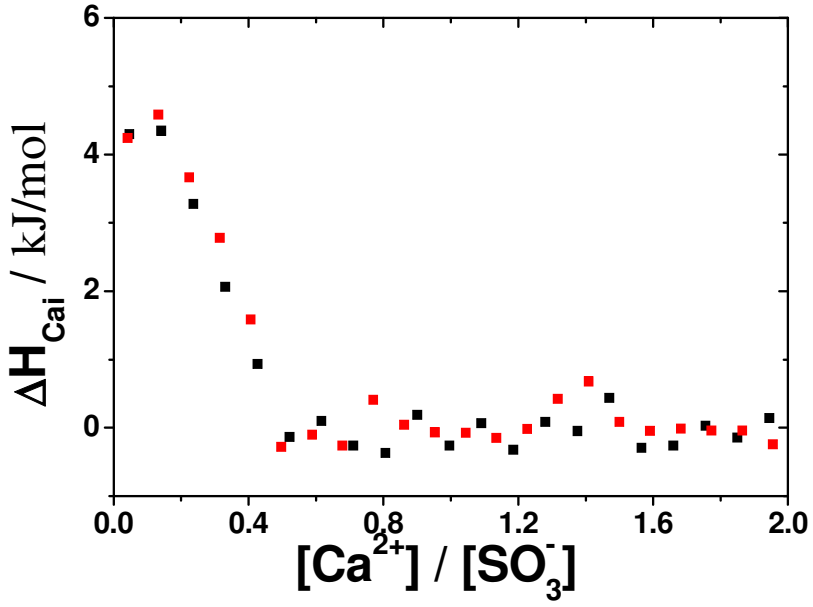

Figure 70: ITC curves for the titration of a solution of NaPSS with a solution of Ca^{2+} (CaPSS-1 ■, CaPSS-2 ■) in pure water.

ΔH_{X-} adopts values between 1.17 kJ/mol and 1.3 kJ/mol (Fig. 70). That is comparable to values observed for the titration NaPSS with Ba^{2+} and Al^{3+} performed in the presence of an inert salt. However, unlike to NaPSS in the presence of Ba^{2+} and Al^{3+}, NaPSS in the presence of Ca^{2+} does not show a phase boundary and does not exhibit a coil shrinking with an increasing Ca^{2+}-concentration, which exceeds conventional screening effects [Chapter 4.3.1]. Accordingly, no precipitate appears in the ITC experiment. Apparently, Ca^{2+}-cations do not interact specifically with the PSS coils.

Under the assumption that all Na^+-cations are replaced by the Ca^{2+}-cations and that each liberated cation requires a thermal energy of 1.5 kT whereby two Na^+-cations are liberated to the bulk while one Ca^{2+}-cation is bound a maximum energy of 3.718 kJ/mol of Ca^{2+} and $\Delta H_{X-,theoretical}$=1.859 kJ/mol of SO_3^- would be needed. The actual ΔH_{X-} which was measured per monomer is smaller compared to the theoretical value per monomer (Tab. 24). That is not completely surprising because the Ca^{2+}-cations do not seem to interact specifically with the PSS coils and not all Ca^{2+}-cations enter the polymer domain at equilibrium.

Table 24: Values for ΔH_{Mi}, the total integral and ΔH_{X^-} for each experiment.

	ΔH_{Mi} / kJ/mol	Integral / J	ΔH_{X^-} / kJ/mol	ΔH_{Mi} / kJ/mol	Integral / J	ΔH_{x^-} / kJ/mol
Baseline correction by	fitted background			solvent titration		
CaPA-1 i=2	16.275	2.802	5.767	18.202	3.200	6.585
CaPA-2 i=3	16.450	3.066	6.305	x	x	x
BaPA-1 i=2	9.429	1.495	3.148	x	x	x
BaPA-2 i=2	9.975	1.712	3.530	x	x	x
AlPSS-pH3-1 i=2	6.94	0.636	1.665	x	x	x
AlPSS-pH3-3 i=2	9.321	0.464	1.674	x	x	x
AlPSS-pH6-1 i=2	9.798	0.747	2.034	x	x	x
AlPSS-pH6-2 i=2	10.453	0.643	2.323	x	x	x
AlPSS-NaCl-pH3-1 i=3	4.749	0.065	1.152	x	x	x
AlPSS-NaCl-pH3-2 i=3	5.128	0.060	1.073	x	x	x
BaPSS-1 i=2	2.432	-0.616	-1.578	3.371	-0.472	-1.208
BaPSS-2 i=2	3.145	-0.588	-1.487	x	x	x
BaPSS-3 i=2	2.765	-0.316	-1.529	3.352	-0.297	-1.440
BaPSS-NaCl-1	0.229	x	x	x	x	x
BaPSS-NaCl-option i=2	0.760	-0.045	-1.385	x	x	x
CaPSS-1 i=2	x	x	x	4.349	0.241	1.167
CaPSS-2 i=2	x	x	X	4.585	0.275	1.302

The measurements on NaPSS in the presence of Ca^{2+} and Ba^{2+} underline that a two-step process takes place. After being injected to the polyelectrolyte solution, the alkaline earth cations start to penetrate the negatively charged polyelectrolyte domains. As a consequence a certain amount of the original Na^+-counterions are replaced by Ca^{2+} and Ba^{2+} and leave the polyelectrolyte domains. The replacement is thus driven by entropy and can be seen also in the beginning of the titration of NaPSS with Ca^{2+} and Ba^{2+}, where a slightly positive enthalpy was measured. Subsequently a complexation between the cations and the polyelectrolyte takes place, which can be related to the negative enthalpy measured for PSS in the presence of Ba^{2+}. In case of PSS in the presence of Ca^{2+} this part is missing because Ca^{2+} does no interact specifically with polystyrene sulfonate. In case of PA in the presence of Ca^{2+} and Ba^{2+} and PSS in the presence of Al^{3+} one cannot discriminate between the two reaction steps by means of thermodynamic data, because both steps exhibit a positive binding enthalpy.

According to the theoretical $\Delta H_{X^-,}$ =1.859 kJ/mol per monomer group a theoretical value for the entropy of the reaction can be calculated under the assumption of 100% conversion. This value is in all experiments significant smaller than the actual value (Tab. 25).

Table 25: Theoretical and actual values for the integral of the positive part of the ITC curve.

Experiment	Theoretical value for integral of the positive part / J	Actual value for the integral of the positive part / J
CaPSS-1	0.384	0.241
CaPSS-2	0.393	0.275
BaPSS-1	0.726	0.127
BaPSS-2	0.736	0.182
BaPSS-3	0.384	0.095
BaPSS-NaCl-option	0.060	0.007

The difference between the theoretical and the actual value of the integral of the positive part of the ITC curve in case of experiment CaPSS-1 and CaPSS-2 is not surprising and can be explained by incomplete conversion at the equilibrium state. The Ca^{2+} do not interact specifically with the residual groups, and therefore not all Ca^{2+}, will enter in the polymer. The differences between the theoretical and actual values are significantly larger in case of experiments with PSS and Ba^{2+} than in case of experiments with PSS and Ca^{2+} , which underlines that the binding process superpose in parts the Ba^{2+}/Na^{+} exchange process.

4.5.3 Summary

Antonietti et al.[29] could show by means of ITC experiments that the binding from Ca^{2+} to polyacrylates exhibits a positive binding energy and thus demonstrated that the binding of Ca^{2+} to the carboxylate groups is an entropically driven process. We could reproduce this observation with ITC measurements on solutions of NaPA with solutions of Ca^{2+}. Further ITC experiments of NaPA solutions with Ba^{2+} solutions reveal qualitatively the same thermodynamic behavior. Only the binding enthalpy of PA in the presence of Ba^{2+} is smaller by a factor of 0.4 than in case of PA in the presence of Ca^{2+}.

PSS in the presence of Al^{3+} was investigated accordingly by ITC. Like NaPA in the presence of Ca^{2+} and Ba^{2+} exhibits a phase boundary with a stoichiometric trend. However, three different solvent states were applied in this case. It could be shown that the influence of the pH in the regime of $3 \leq pH \leq 6$ is negligible, which was expected because PSS is a strong polyacid. By adding inert salt to the PSS solution the ITC curve was shifted to lower enthalpy values. In all three cases the ITC curves of PSS in the presence of Al^{3+} exhibit a positive enthalpy, which is in line with the acceleration of the coil shrinking observed with increasing temperature by light scattering. The thermodynamics of the binding of Al^{3+} to PSS is also in qualitative agreement with that of the binding of Ca^{2+} or Ba^{2+} to PA, whereby all three combinations show an L-type precipitation (stoichiometric trend). Only the values for ΔH_{Mi} and ΔH_{X-} in case of PSS in the presence of Al^{3+} are below the values for PA in the presence of Ca^{2+} and Ba^{2+}.

The ITC experiment for PSS in the presence of Ba^{2+} started with a positive enthalpy but changed during the experiment to a negative enthalpy. This pattern can be interpreted by a two-step model. First the cations enter the polyelectrolyte phase and expel the original

counterions and subsequently the complexation by SO_3^- takes place. In case of the PA with Ba^{2+} or Ca^{2+} and PSS with Al^{3+} the two steps most likely also take place but are not visible because both steps exhibit a positive enthalpy. The negative enthalpy fits to the temperature dependent light scattering experiments, where a decreasing chain size was observed in combination with decreasing sample temperature [Chapter 4.3.2].

For PSS in the presence of Ca^{2+} just a slightly positive enthalpy was observed, which is in line with a non-specific character of the interactions between Ca^{2+} and PSS. It can be assumed that only the replacement of 2 Na^+ per one Ca^{2+}-cation takes place in the polyelectrolyte domain without any complex binding of Ca^{2+} to SO_3^- residues.

In case of PA in the presence of Ca^{2+} or Ba^{2+} and PSS in the presence of Al^{3+} or Ba^{2+} in pure water a spike-like peak becomes visible in the decaying part of the ITC curve. It is assumed that this extra peak is related to the aggregation/precipitation process of the SIC-polyelectrolyte complexes. A precipitate was found on the bottom of the sample container in those cases. Additional turbidity experiments on the same polyelectrolyte SIC combinations showed that the precipitation of the chains takes place at compositions located close to the position of the spike-like extra peak.

5. Conclusions and Outlook

The results of the thesis give an interesting insight into SIC-polyelectrolyte complexes. Differences could be outlined between PSS in the presence of Al^{3+} and PSS in the presence of Ba^{2+}.

- The phase diagram of AlPSS exhibits a L-type threshold and a re-entrant phase boundary. The L-type threshold is typical for nearly all known SIC-polyelectrolyte combinations. A re-entrant phase boundary was also observed by other groups for PSS in the presence of trivalent cations and cations with a higher valence and for proteins in the presence of cations with a valence larger than 2.[20,86,87] The reason for this behavior is the charge reversal due to the addition of a large number of multivalent cations to the residual groups of the polyelectrolyte, which leads to a re-dissolution of the polymer chains. Light scattering measurements on points located above the re-entrant phase boundary reveal a behavior of the polymer chains equal to states, which are located below the L-Type phase boundary.
- The BaPSS phase diagram exhibits just two regimes, one at low Ba^{2+} concentrations, with stable solutions and one at higher Ba^{2+} concentrations, where precipitation takes place. Three details are outstanding: (i) Ba^{2+} is the only alkaline earth cation, which leads to a precipitation with PSS chains. (ii) Precipitation takes place at a concentration of Ba^{2+} which is slightly higher than typically found for an L-type threshold. (iii) The phase boundary exhibits a horizontal trend at low PSS concentrations.
- The threshold which limits the solution state dominated by single coils in the regime at low SIC concentration is shifted to higher values of SIC cations if the inert salt level is increased.
- A shrinking of the PSS chains with increasing Al^{3+} or Ba^{2+} is observable for both SIC-PSS combinations. The shrinking is more distinct in case of BaPSS. However, the shrinking in both cases is not as drastic as in case of the shrinking of PA coils induced by alkaline earth cations, which is still difficult to explain, because PSS exhibits a lower persistence lengt/stiffness than PA. A reason could be that the tendency of the PSS chains towards aggregation is larger than in case of PA chains.
- Small angle scattering experiments revealed that the structure of the PSS chains in the presence of Al^{3+} remain coil-like even at states close to the phase boundary. BaPSS shows, in contrast to AlPSS that the chains become more compact with increasing Ba^{2+} concentration and that dense chain subdomains exist, which are smaller than the entire polymer chain. This supports, the existence of a pearl necklace-like structure or equally likely potatoe- or sausage-like structures at intermediate states. In contrast to AlPSS and BaPSS, polyacrylates in the presence of Ba^{2+}, collapse to compact spheres, which could be shown by SAXS experiments.
- Interesting results were obtained from temperature dependent light scattering experiments in combination with ITC experiments. Like in case of CaPA and SrPA, the shrinking of the PSS chains in the presence of Al^{3+} cations is enhanced by an increase

of the sample temperature, suggesting that the binding reaction is an entropically driven process. BaPSS shows the opposit effect, a decreasing sample temperature leads a decreasing chain size. ITC measurements indeed prove that the binding process is exothermal. Additionally the ITC measurements on BaPSS revealed that a two step process takes place. Beginning with an endothermic part, which can be attributed to the infiltration of the polymer domains by the Ba^{2+} cations and a release of Na^{+} counterions. Subsequently, the binding of the Ba^{2+} cations to the SO_3^- residues of the polymer takes place, which is enthalpically driven.

- Aggregation of BaPSS was induced by component mixing and by a temperature jump. In both cases aggregates are formed, which are compact but not as compact as dense spheres. A difference between both methods was observed during the initial period. In contrast to the induction by a temperature jump, where compact aggregates are formed directly from the beginning, the structure of the aggregated BaPSS chains induced by component mixing is in the beginning more polydispers and fluffy. The aggregates become more compact with time. A probable explanation is that the coils in the temperature induced aggregation assemble slowly enough to enable for simultaneous compaction, while the coils in the aggregates induced by component mixing aggregate much faster, thereby kinetically trapping extended states which inhibit further shrinking.

There are various ideas, how the project can be further developed in the future.

- One topic is to find more SIC-PSS combinations. One very interesting candidate could be iron. It could be demonstrated that PSS in the presence of Fe(III) leads to an L-type threshold and a shrinking of the PSS chain, which is comparable to that induced by Al^{3+}.[23] It would be very interesting to see, if a re-entrant phase boundary could be found also for Fe(III)PSS. It may be possible that also Fe(II) like Fe(III) interacts specifically with PSS. The main question is, which type of phase boundary could be found in this case; an L-type like in the case of Fe(III) and Al^{3+} or a phase boundary which is similar to that of BaPSS.
- SANS/SAXS experiments on PSS in the presence of Fe(III), could reveal similarities and differences to AlPSS and BaPSS. Especially the structure of the chains close to the phase boundary would be very interesting.
- ASAXS on BaPSS could be a better way to reveal the structure of the densified subdomains of the chains and the corresponding Ba^{2+} distribution than SANS and SAXS is
- Time resolved SAXS experiments could be interesting for the shrinking of BaPSS and BaPA at states close to the phase boundary. The shrinking of the chains at points that are close to the threshold seems to be decelerated, as it was outlined in the present thesis. So it could be possible to observe the change of the chain structure from a coil to compact states with time.
- A block copolymer of PA and PSS may establish a powerful material with new responsive features. The collapse of the different blocks in the presence of Ba^{2+} could

be tuned via the sample temperature. Toward higher temperatures the PA block would collapse and the PSS block would be expanded and toward lower temperatures the PSS block would shrink and the PA block would be expanded.

- Fitting of the ITC curves with an appropriate model would lead to more information about the thermodynamics of the binding process.

6. Appendix

A1: Solution Behavior of PSS in the Presence of Al^{3+}

The light scattering experiments of series h-AlPSS-1 and h-AlPSS-3 are presented in the following by Figure A 1 and A 2.

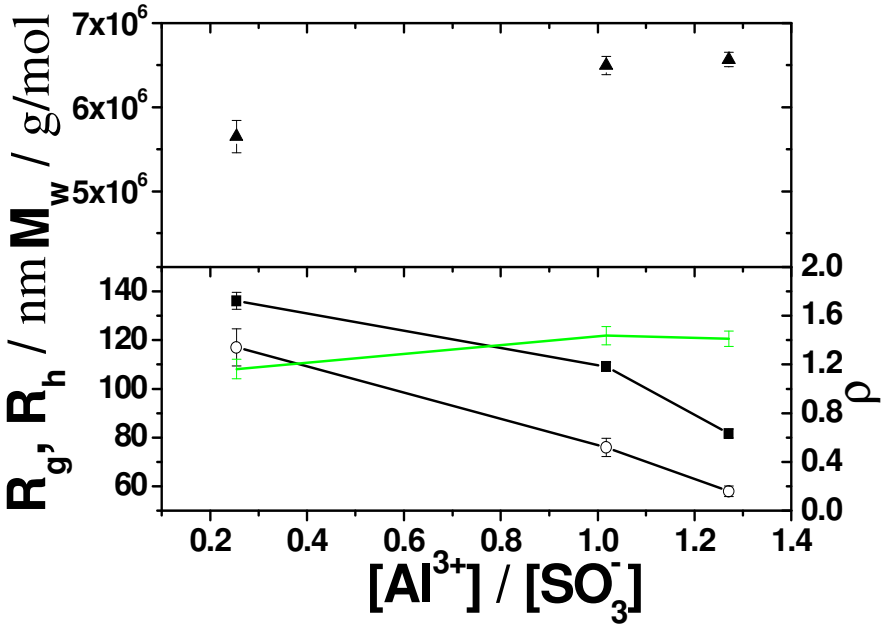

Figure A 1: R_g (■), R_h (○), M_w (▲) and ρ (green line) of h-NaPSS-2 at [I]=0.1 M as a function of the ratio of $[Al^{3+}]/[SO_3^-]$ in series h-AlPSS-1

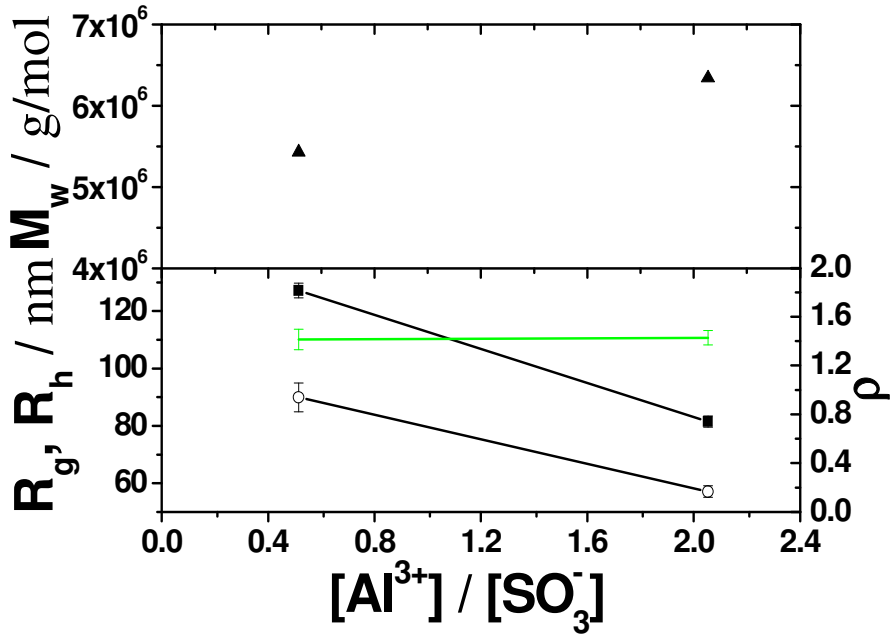

Figure A 2 R_g (■), R_h (○), M_w (▲) and ρ (green line) of h-NaPSS-2 at [I]=0.1 M as a function of the ratio of $[Al^{3+}]/[SO_3^-]$ in series h-AlPSS-3

For the experiments in D_2O a NaPSS sample with a smaller molecular weight was used in order to facilitate data evaluation of small angle scattering experiments. Due to the smaller size of polymer sample h-NaPSS-1 0.2 µm filters were used instead of 0.45 µm filters, applied for all experiments with polymer samples h-NaPSS-2 and d-NaPSS.

At least two alternative ways of preparing the light scattering solutions appear to be adequate. Separate filtering of each component (I) or mixing the components first and filtering of the combined solution (II). We tested both procedures for h-NaPSS-1 in the presence of Al^{3+} and analysed both samples by light scattering. Fig. A 3 demonstrates that size and apparent M_w are independent of the sample preparation. Usually we applied procedure I for the combined light scattering experiments. But in case of the SANS/SAXS experiments at the ILL/ESRF procedure II was preferred in order to perform LS and SANS/SAXS with identically prepared solutions. Therefore the sample was mixed first and filtered afterwards by the same work step a 0.2 µm filter.

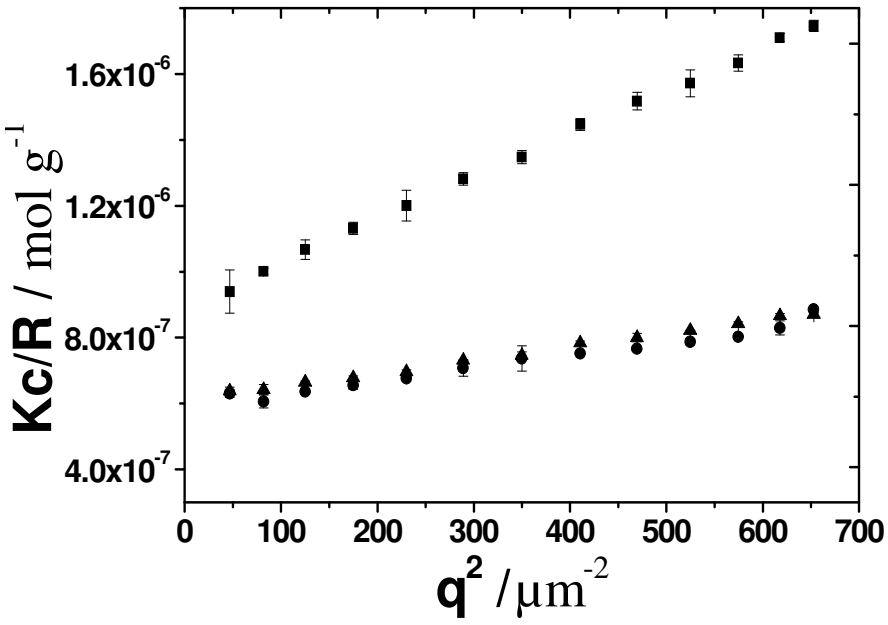

Figure A 3: Zimm Plot of 1.3mM h-NaPSS-1 at [I]=0.1 M in the absence of Al^{3+} filtered by a 0.2 µm filter (■) and a sample consisting of 1.3mM h-NaPSS-1 and 2.1 mM Al^{3+} at [I]=0.1 M prepared by separate filtering of the stock solutions (●) with a 0.2 µm filter and by filtering of the combined sample with a 0.2 µm filter (▲).

In agreement with the trends observed with all other polymer samples R_g and R_h of the h-NaPSS-1 chains decrease with increasing Al^{3+}-content while the structure sensitive parameter stay constant at ρ=1.4 (Fig. 30). The apparent mass kept below the value of a single coil. Surprisingly no increase of M_w was noticeable with increasing $[Al^{3+}]$ in the present case. A reason could be the use of D_2O as solvent or that in contrast to other sample series which are presented in this manuscript the series in D_2O covered a narrow range in $[Al^{3+}]$ (Fig. 29).

A2: Verification of Radiation Damage by SAXS

In order to scrutinize for a possible damage of the AlPSS and BaPSS coils by irradiation with the x-ray beam during SAXS at ID02 both samples analyzed by SAXS where measured with a sequence of 10 time frames of 1s each.

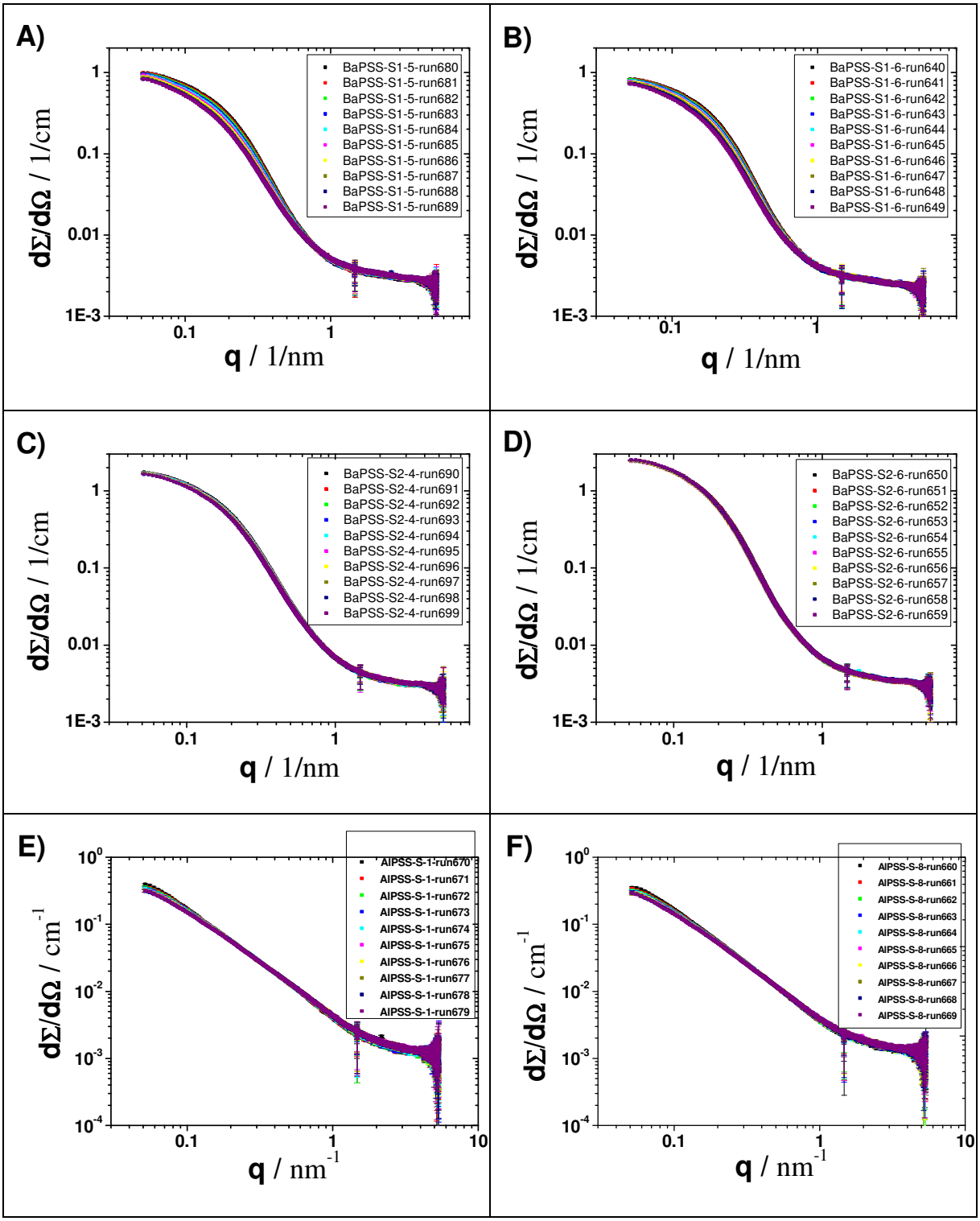

A 4: Ten SAXS curves of sample BaPSS-S1-5 (A), BaPSS-S1-6 (B), BaPSS-S2-4 (C), BaPSS-S2-6 (D), AlPSS-S-1 (E) and AlPSS-S-8 (F). Each scattering curve was measured for 1 second.

The resulting scattering curves show a trend at low q. Hence, only the first curve of each sequence is used in the thesis.

References

(1) Manning, G. S. Counterion binding in polyelectrolyte theory. *Acc. Chem. Res.* **1979**, *12*, 443–449.

(2) Flory, P. J.; Osterheld, J. E. Intrinsic Viscosities of Polyelectrolytes. Poly-(acrylic Acid). *J. Phys. Chem.* **1954**, *58*, 653–661.

(3) Takahashi, A.; Nagasawa, M. Excluded Volume of Polyelectrolyte in Salt Solutions. *J. Am. Chem. Soc.* **1964**, *86*, 543–548.

(4) Kitano, T.; Taguchi, A.; Noda, I.; Nagasawa, M. Conformation of Polyelectrolyte in Aqueous Solution. *Macromolecules* **1980**, *13*, 57–63.

(5) Wang, L.; Yu, H. Chain conformation of linear polyelectrolyte in salt solutions: Sodium poly(styrenesulfonate) in potassium chloride and sodium chloride. *Macromolecules* **1988**, *21*, 3498–3501.

(6) Schweins, R.; Hollmann, J.; Huber, K. Dilute solution behaviour of sodium polyacrylate chains in aqueous NaCl solutions. *Polymer* **2003**, *44*, 7131–7141.

(7) Hirose, E.; Iwamoto, Y.; Norisuye, T. Chain Stiffness and Excluded-Volume Effects in Sodium Poly(styrenesulfonate) Solutions at High Ionic Strength. *Macromolecules* **1999**, *32*, 8629–8634.

(8) Takahashi, A.; Kato, T.; Nagasawa, M. The Second Virial Coefficient of Polyelectrolytes. *J. Phys. Chem.* **1967**, *71*, 2001–2010.

(9) Hara, M.; Nakajima, A. Characteristic Behaviors of Light Scattering from Polyelectrolyte in Dilute Solution Region. *Polym J* **1980**, *12*, 701–709.

(10) Wall, F. T.; Drenan, J. W. Gelation of polyacrylic acid by divalent cations. *J. Polym. Sci.* **1951**, *7*, 83–88.

(11) Huber, K. Calcium-induced shrinking of polyacrylate chains in aqueous solution. *J. Phys. Chem.* **1993**, *97*, 9825–9830.

(12) Schweins, R.; Huber, K. Collapse of sodium polyacrylate chains in calcium salt solutions. *Eur. Phys. J. E* **2001**, 117–126.

(13) Schweins, R.; Goerigk, G.; Huber, K. Shrinking of anionic polyacrylate coils induced by Ca2+, Sr2+ and Ba2+: a combined light scattering and ASAXS study. *The European physical journal. E, Soft matter* **2006**, *21*, 99–110.

(14) Lages, S.; Michels, R.; Huber, K. Coil-Collapse and Coil-Aggregation due to the Interaction of Cu 2+ and Ca 2+ Ions with Anionic Polyacylate Chains in Dilute Solution. *Macromolecules* **2010**, *43*, 3027–3035.

(15) Lages, S.; Goerigk, G.; Huber, K. SAXS and ASAXS on Dilute Sodium Polyacrylate Chains Decorated with Lead Ions. *Macromolecules* **2013**, *46*, 3570–3580.

(16) Ezhova, A.; Huber, K. Specific Interactions of Ag + Ions with Anionic Polyacrylate Chains in Dilute Solution. *Macromolecules* **2014**, *47*, 8002–8011.

(17) Ikegami, A.; Imai, N. Precipitation of polyelectrolytes by salts. *J. Polym. Sci.* **1962**, *56*, 133–152.

(18) Michaeli, I. Ion binding and the formation of insoluble polymethacrylic salts. *J. Polym. Sci.* **1960**, *48*, 291–299.

(19) Drifford, M.; Dalbiez, J.-P.; Delsanti, M.; Belloni, L. Structure and dynamics of polyelectrolyte solutions with multivalent salts. *Berichte der Bunsengesellschaft für physikalische Chemie* **1996**, *100*, 829–835.

(20) La Cruz, M. O. de; Belloni, L.; Delsanti, M.; Dalbiez, J. P.; Spalla, O.; Drifford, M. Precipitation of highly charged polyelectrolyte solutions in the presence of multivalent salts. *J. Chem. Phys.* **1995**, *103*, 5781.

(21) Narh, K. A.; Keller, A. Precipitation effects in polyelectrolytes on addition of salts. *J. Polym. Sci. B Polym. Phys.* **1993**, *31*, 231–234.
(22) Yanjing Zhao. Fällungsverhalten von Zink-Polyacrylat aus wässeriger Lösung. Bachelorarbeit, Universität Paderborn, Paderborn, 2015.
(23) Markus Hansch. Phasenverhalten von Polyelektrolyten in Gegenwart spezifisch wirkender Metall - Kationen. Masterarbeit, Universität Paderborn, Paderborn, 2013.
(24) Ralf Schweins. Gestaltsänderungen gelöster anionischer Polyacrylatketten in Gegenwart von Erdalkaliionen. Dissertation, Universität Paderborn, Paderborn, 2002.
(25) Schweins, R.; Lindner, P.; Huber, K. Calcium Induced Shrinking of NaPA Chains: A SANS Investigation of Single Chain Behavior. *Macromolecules* **2003**, *36*, 9564–9573.
(26) Schweins, R.; Huber, K. Particle scattering factor of pearl necklace chains. *Macromol. Symp.* **2004**, *211*, 25–42.
(27) Goerigk, G.; Schweins, R.; Huber, K.; Ballauff, M. The distribution of Sr 2+ counterions around polyacrylate chains analyzed by anomalous small-angle X-ray scattering. *Europhys. Lett.* **2004**, *66*, 331–337.
(28) Sebastian Lages. Untersuchungen zum Kollabierungs- und Aggregationsverhalten von gelösten Polyacrylaten in Gegenwart zweiwertiger Kationen. Dissertation, Universität Paderborn, Paderborn, 2010.
(29) Sinn, C. G.; Dimova, R.; Antonietti, M. Isothermal Titration Calorimetry of the Polyelectrolyte/Water Interaction and Binding of Ca 2+: Effects Determining the Quality of Polymeric Scale Inhibitors. *Macromolecules* **2004**, *37*, 3444–3450.
(30) Lages, S.; Schweins, R.; Huber, K. Temperature-induced collapse of alkaline Earth cation-polyacrylate anion complexes. *The journal of physical chemistry. B* **2007**, *111*, 10431–10437.
(31) Lages, S.; Lindner, P.; Sinha, P.; Kiriy, A.; Stamm, M.; Huber, K. Formation of Ca 2+ -Induced Intermediate Necklace Structures of Polyacrylate Chains. *Macromolecules* **2009**, *42*, 4288–4299.
(32) Anna Ezhova. Specific interactions of Ag+ ions with linear Pa chains. Dissertation, Universität Paderborn, Paderborn, 2015.
(33) Ezhova, A.; Huber, K. Contraction and Coagulation of Spherical Polyelectrolyte Brushes in the Presence of Ag + , Mg 2+ , and Ca 2+ Cations. *Macromolecules* **2016**, *49*, 7460–7468.
(34) Solis, F. J. Phase diagram of dilute polyelectrolytes: Collapse and redissolution by association of counterions and co-ions. *The Journal of chemical physics* **2002**, *117*, 9009–9015.
(35) Morawetz, H. Structure-solubility relationships in polymers, Frank W. Harris and Raymond B. Seymour, Eds., Academic Press, New York, 1977, 271 pp. $13.00. *J. Polym. Sci. B Polym. Lett. Ed.* **1977**, *15*, 634.
(36) Prabhu, V. M.; Muthukumar, M.; Wignall, G. D.; Melnichenko, Y. B. Dimensions of polyelectrolyte chains and concentration fluctuations in semidilute solutions of sodium–poly(styrene sulfonate) as measured by small-angle neutron scattering. *Polymer* **2001**, *42*, 8935–8946.
(37) Prabhu, V. M.; Muthukumar, M.; Wignall, G. D.; Melnichenko, Y. B. Polyelectrolyte chain dimensions and concentration fluctuations near phase boundaries. *J. Chem. Phys.* **2003**, *119*, 4085.
(38) Kanai, S.; Muthukumar, M. Phase separation kinetics of polyelectrolyte solutions. *The Journal of chemical physics* **2007**, *127*, 244908.
(39) *Neutrons, X-rays and light: Scattering methods applied to soft condensed matter ; [completely revised 'Bombannes' lectures];* Lindner, P.; Zemb, T., Eds., 1. ed.; North-Holland delta series; Norh-Holland Elsevier: Amsterdam, 2002.
(40) Berne, B. J.; Pecora, R. *Dynamic Light Scattering: With Applications to Chemistry, Biology, and Physics*; Dover Books on Physics; Dover Publications: Newburyport, 2013.

(41) Chu, B. *Laser Light Scattering: Basic Principles and Practice. Second Edition*; Dover Books on Physics; Dover Publications: Newburyport, 2013.
(42) Schärtl, W. *Light scattering from polymer solutions and nanoparticle dispersions*, 1. ed.; Springer Berlin: Berlin, 2007.
(43) Teraoka, I. *Polymer Solutions: An Introduction to Physical Properties*, 1st ed.; Wiley-Interscience: S.l., 2002.
(44) Rubinstein, M.; Colby, R. H. *Polymer physics*, 1. publ., repr; Oxford Univ. Press: Oxford u.a., 2011.
(45) *Light scattering: Principles and development;* Brown, W., Ed., 1. ed.; Oxford science publications 53; Clarendon Press: Oxford, 1996.
(46) Morawetz, H. Light scattering from polymer solutions, M. B. Huglin, Ed., Aca-demic Press Inc., London, 1972. 885 pp. $45.00. *J. Polym. Sci. B Polym. Lett. Ed.* **1973**, *11*, 68–69.
(47) Kratochvíl, P. *Classical light scattering from polymer solutions*; Polymer science library 5; Elsevier: Amsterdam u.a., 1987.
(48) Rayleigh, L. On the Diffraction of Light by Spheres of Small Relative Index. *Proceedings of the Royal Society A: Mathematical, Physical and Engineering Sciences* **1914**, *90*, 219–225.
(49) Zimm, B. H. Apparatus and Methods for Measurement and Interpretation of the Angular Variation of Light Scattering; Preliminary Results on Polystyrene Solutions. *J. Chem. Phys.* **1948**, *16*, 1099.
(50) Guinier, A.; Fournet, B. *Small Angle Scattering of X-Rays*; Wiley-VCH: New York, 1955.
(51) Brown, R. A Brief Account of Microscopical Observations made in the Months of June, July, and August, 1827, on the Particles contained in the Pollen of Plants; and on the General Existence of Active Molecules in Organic and Inorganic Bodies. In *The miscellaneous botanical works of Robert Brown*; Brown, R., Bennett, J. J., Eds.; Cambridge library collection. Botany and horticulture; Cambridge University Press: Cambridge, 2015; pp 463–486.
(52) Einstein, A. Über die von der molekularkinetischen Theorie der Wärme geforderte Bewegung von in ruhenden Flüssigkeiten suspendierten Teilchen. *Ann. Phys.* **1905**, *322*, 549–560.
(53) Smoluchowski, M. von. Zur kinetischen Theorie der Brownschen Molekularbewegung und der Suspensionen. *Ann. Phys.* **1906**, *326*, 756–780.
(54) Christian Doppler. Ueber das farbige Licht der Doppelsterne und einiger anderer Gestirne des Himmels. *Abhandlungen der k. böhm. Gesellschaft der Wissenschaften* **1842**, *5*, 465–482.
(55) Siegert, A. J. F. *MIT Radiation Lab* **1943**, Report No. 465.
(56) Koppel, D. E. Analysis of Macromolecular Polydispersity in Intensity Correlation Spectroscopy: The Method of Cumulants. *J. Chem. Phys.* **1972**, *57*, 4814.
(57) Burchard, W. *Light scattering from polymers*; Advances in polymer science 48; Springer: Berlin, 1983.
(58) Burchard, W.; Schmidt, M.; Stockmayer, W. H. Information on Polydispersity and Branching from Combined Quasi-Elastic and Intergrated Scattering. *Macromolecules* **1980**, *13*, 1265–1272.
(59) Schmidt, M. Combined integrated and dynamic light scattering by poly(γ-benzyl glutamate) in a helocogenic solvent. *Macromolecules* **1984**, *17*, 553–560.
(60) Donkai, N.; Inagaki, H.; Kajiwara, K.; Urakawa, H.; Schmidt, M. *Makromol. Chem.* **1985**, *186*, 2623–2638.
(61) EPN-Campus: PSMC Equipment. http://www.epn-campus.eu/users/pscm/pscm-facilities/psmc-equipment/ (accessed October 18, 2016).
(62) NIST Center for Neutron Research. https://www.ncnr.nist.gov/resources/n-lengths/elements/h.html (accessed March 5, 2017).

(63) D11 at ILL. https://www.ill.eu/instruments-support/instruments-groups/instruments/d11/description/instrument-layout/ (accessed March 5, 2017).
(64) Vitaliy Pipich. KWS-3 or VerySANS : Very-High Resolution Focusing SANS Diffractometer. http://iffwww.iff.kfa-juelich.de/~pipich/dokuwiki/doku.php/kws3 (accessed March 5, 2017).
(65) Schneider, M.; Michels, R.; Pipich, V.; Goerigk, G.; Sauer, V.; Heim, H.-P.; Huber, K. Morphology of Blends with Cross-Linked PMMA Microgels and Linear PMMA Chains. *Macromolecules* **2013**, *46*, 9091–9103.
(66) Wignall, G. D.; Bates, F. S. Absolute calibration of small-angle neutron scattering data. *J Appl Crystallogr* **1987**, *20*, 28–40.
(67) Goerigk, G.; Varga, Z. Comprehensive upgrade of the high-resolution small-angle neutron scattering instrument KWS-3 at FRM II. *J Appl Crystallogr* **2011**, *44*, 337–342.
(68) *Small angle X-ray scattering;* Glatter, O.; Kratky, O., Eds.; Acad. Pr: London, 1982.
(69) ID02 - TIME-RESOLVED ULTRA SMALL-ANGLE X-RAY SCATTERING. http://www.esrf.eu/home/UsersAndScience/Experiments/CBS/ID02/BeamlineLayout.html (accessed March 5, 2017).
(70) Labrador, A.; Cerenius, Y.; Svensson, C.; Theodor, K.; Plivelic, T. The yellow mini-hutch for SAXS experiments at MAX IV Laboratory. *J. Phys.: Conf. Ser.* **2013**, *425*, 72019.
(71) Porod, G. Die Röntgenkleinwinkelstreuung von dichtgepackten kolloiden Systemen. *Kolloid-Zeitschrift* **1951**, *124*, 83–114.
(72) Porod, G. Die Röntgenkleinwinkelstreuung von dichtgepackten kolloiden Systemen. *Kolloid-Zeitschrift* **1952**, *125*, 51–57.
(73) Benoît, M. H. La diffusion de la lumière par des macromolécules en chaînes en solution dans un bon solvant. *Comptes rendus hebdomadaires des séances de l'Académie des sciences* **1957**, *245*, 2244–2247.
(74) Hammouda, B. *SANS from Homogeneous Polymer Mixtures A Unified Overview*; Advances in polymer science 106; Springer: Berlin u.a., 1993.
(75) Higgins, J. S.; Benoît, H. *Polymers and neutron scattering*, Reprint. with corr; Oxford series on neutron scattering in condensed matter 8; Clarendon Press: Oxford u.a., 1996.
(76) *Structure analysis by small-angle X-ray and neutron scattering;* Feigin, L. A.; Svergun, D. I.; Taylor, G. W., Eds.; Plenum Press: New York, 1987.
(77) Freire, E.; Mayorga, O. L.; Straume, M. Isothermal titration calorimetry. *Anal. Chem.* **1990**, *62*, 950A-959A.
(78) Wiseman, T.; Williston, S.; Brandts, J. F.; Lin, L.-N. Rapid measurement of binding constants and heats of binding using a new titration calorimeter. *Analytical Biochemistry* **1989**, *179*, 131–137.
(79) *Protein-ligand interactions: Hydrodynamics and calorimetry ; a practical approach;* Harding, S. E.; Chowdhry, B. Z., Eds.; The practical approach series; Oxford Univ. Press: Oxford, 2007.
(80) Brüssau, R.; Goetz, N.; Mächtle, W.; Stölting, J. *Tenside Surf. Det.* **1991**, *28*, 396.
(81) Brice, B. A.; Halwer, M. A Differential Refractometer*. *J. Opt. Soc. Am.* **1951**, *41*, 1033.
(82) Pipich, V.; Fu, Z. KWS-3: Very small angle scattering diffractometer with focusing mirror. *JLSRF* **2015**, *1,* DOI: 10.17815/jlsrf-1-28.
(83) Pipich, V. *QtiKWS*; JCNS/MLZ.
(84) ILL. *LAMP (Large Array Manipulation Program)*; Institut Laue Langevin.
(85) Berry, G. C. Thermodynamic and Conformational Properties of Polystyrene. I. Light-Scattering Studies on Dilute Solutions of Linear Polystyrenes. *The Journal of chemical physics* **1966**, *44*, 4550–4564.

(86) Zhang, F.; Skoda, M. W. A.; Jacobs, R. M. J.; Zorn, S.; Martin, R. A.; Martin, C. M.; Clark, G. F.; Weggler, S.; Hildebrandt, A.; Kohlbacher, O. *et al.* Reentrant condensation of proteins in solution induced by multivalent counterions. *Physical review letters* **2008**, *101*, 148101.
(87) Zhang, F.; Weggler, S.; Ziller, M. J.; Ianeselli, L.; Heck, B. S.; Hildebrandt, A.; Kohlbacher, O.; Skoda, M. W. A.; Jacobs, R. M. J.; Schreiber, F. Universality of protein reentrant condensation in solution induced by multivalent metal ions. *Proteins* **2010**, *78*, 3450–3457.
(88) Volk, N.; Vollmer, D.; Schmidt, M.; Oppermann, W.; Huber, K. *Polyelectrolytes with Defined Molecular Architecture II*; Advances in polymer science 166, 2004.
(89) Axelos, M. A. V.; Mestdagh, M. M.; Francois, J. Phase Diagrams of Aqueous Solutions of Polycarboxylates in the Presence of Divalent Cations. *Macromolecules* **1994**, *27*, 6594–6602.
(90) Jia, P.; Zhao, J. Single chain contraction and re-expansion of polystyrene sulfonate: a study on its re-entrant condensation at single molecular level. *The Journal of chemical physics* **2009**, *131*, 231103.
(91) Horkay, F.; Tasaki, I.; Basser, P. J. Osmotic Swelling of Polyacrylate Hydrogels in Physiological Salt Solutions. *Biomacromolecules* **2000**, *1*, 84–90.
(92) Dingenouts, N.; Patel, M.; Rosenfeldt, S.; Pontoni, D.; Narayanan, T.; Ballauff, M. Counterion Distribution around a Spherical Polyelectrolyte Brush Probed by Anomalous Small-Angle X-ray Scattering. *Macromolecules* **2004**, *37*, 8152–8159.
(93) Prabhu, V. M.; Amis, E. J.; Bossev, D. P.; Rosov, N. Counterion associative behavior with flexible polyelectrolytes. *The Journal of chemical physics* **2004**, *121*, 4424–4429.
(94) Nierlich, M.; Boue, F.; Lapp, A.; Oberthür, R. Characteristic lengths and the structure of salt free polyelectrolyte solutions. A small angle neutron scattering study. *Colloid & Polymer Sci* **1985**, *263*, 955–964.
(95) Weill, G.; Maret, G. Magnetic birefringence of polystyrene sulphonate: Molecular weight and concentration dependence. *Polymer* **1982**, *23*, 1990–1993.
(96) Provencher, S. W. A constrained regularization method for inverting data represented by linear algebraic or integral equations. *Computer Physics Communications* **1982**, *27*, 213–227.
(97) Provencher, S. W. CONTIN: A general purpose constrained regularization program for inverting noisy linear algebraic and integral equations. *Computer Physics Communications* **1982**, *27*, 229–242.
(98) Liao, Q.; Dobrynin, A. V.; Rubinstein, M. Counterion-Correlation-Induced Attraction and Necklace Formation in Polyelectrolyte Solutions: Theory and Simulations. *Macromolecules* **2006**, *39*, 1920–1938.
(99) Liu, J.; Rieger, J.; Huber, K. Analysis of the nucleation and growth of amorphous CaCO3 by means of time-resolved static light scattering. *Langmuir : the ACS journal of surfaces and colloids* **2008**, *24*, 8262–8271.
(100) Vishnevetskaya, N. S.; Hildebrand, V.; Niebuur, B.-J.; Grillo, I.; Filippov, S. K.; Laschewsky, A.; Müller-Buschbaum, P.; Papadakis, C. M. Aggregation Behavior of Doubly Thermoresponsive Polysulfobetaine- b -poly(N -isopropylacrylamide) Diblock Copolymers. *Macromolecules* **2016**, *49*, 6655–6668.
(101) Yu, J.; Mao, J.; Yuan, G.; Satija, S.; Jiang, Z.; Chen, W.; Tirrell, M. Structure of Polyelectrolyte Brushes in the Presence of Multivalent Counterions. *Macromolecules* **2016**, *49*, 5609–5617.
(102) RÖMPP - Methylbenzolsulfonsäuren - Georg Thieme Verlag KG. https://roempp.thieme.de/roempp4.0/do/data/RD-13-04124 (accessed November 29, 2016).
(103) Antonietti, M.; Briel, A.; Gröhn, F. Structure and Viscosity of Spherical Polyelectrolyte Microgels: A Model for the Polyelectrolyte Effect? In *Structure and Dynamics of Polymer and Colloidal Systems*; Borsali, R., Pecora, R., Eds.; Springer Netherlands: Dordrecht, 2002; pp 363–415.

(104) Förster, S.; Schmidt, M.; Antonietti, M. Static and dynamic light scattering by aqueous polyelectrolyte solutions: Effect of molecular weight, charge density and added salt. *Polymer* **1990**, *31*, 781–792.
(105) Brett, E. D.; Amis, E. J. Domain Structures in Low Ionic Strength Polyelectrolyte Solutions. *Macromolecules* **1998**, *31*, 7378–7384.